MODELLING OF NEGATIVE CORONA DISCHARGE CHEMISTRY IN DRY AIR

MODELLING OF NEGATIVE CORONA DISCHARGE CHEMISTRY IN DRY AIR FOR A COAXIAL WIRE–TUBE ELECTRODE SYSTEM

By

ALEXANDER L.C. KWAN, B.Sc.

Part 2: On-Campus Project

A Report
Submitted to the School of Graduate Studies
in Partial Fulfillment of the Requirements
for the Degree of
M. Eng. in Engineering Physics

One of Two Project Reports:
The Other Report is Designated as
Part 1: Off-Campus Project

McMaster University

MASTER OF ENGINEERING (1997)
(Engineering Physics)

McMaster University
Hamilton, Ontario

TITLE: Modelling of Negative Corona Discharge Chemistry in Dry Air for a Coaxial Wire–Tube Electrode System

AUTHOR: Alexander L.C. Kwan, B.Sc. (University of Alberta)

SUPERVISOR: Dr. J.S. Chang

NUMBER OF PAGES: xix, 169

Abstract

Acid rain, which can damage buildings, vegetation and affect the health of animals, is produced when oxides like NO_x and SO_x are released into the atmosphere and react with the water vapor in air. These oxides may be produced during the combustion process in a fossil fuel fire power plant. Consequently, a number of methods have been studied to reduce the emission of these oxides from the flue gas exhaust. One of these methods is the corona discharge induced non-thermal plasma technique.

Corona discharge is a gas discharge in which electron, neutral radicals and ions are generated in the process. These electron, free radicals and ions will react with the oxides. The feasibility of NO_x and SO_x removal from the flue gas by the corona discharge method has been attempt in a number of studies. However, the mechanism behind the discharge process is still not well understood in this moment since the dominant plasma chemistry is not well investigated. In this work, a negative dc corona discharge chemistry in a coaxial wire-tube electrode configuration is numerically simulated.

The purpose of this work is to try to gain a better fundamental understanding of the corona discharge process. In this model, the continuity equations and the charged (or neutral) particle transport equations are solved

simultaneous with the Poisson's equations. One hundred and ninety-five chemical reactions for 38 different chemical species are included. These species can be divided into three groups. The first group is the negative ions which includes O^-, O_2^-, O_3^-, O_4^-, NO^-, NO_2^-, NO_3^-, $N_2O_2^-$ and $N_2O_3^-$. The second group is the neutral species which includes O, O_2, O_3, N, N_2, NO, NO_2, N_2O, NO_3, N_2O_4 and N_2O_5. The third group is the positive ions which includes O^+, O_2^+, O_4^+, O_6^+, N^+, N_2^+, N_3^+, N_4^+, NO^+, NO_2^+, NO_3^+, NO_4^+, N_2O^+, $N_2O_2^+$, $N_2O_3^+$, $N_2O_4^+$, N_3O^+ and $N_4O_2^+$.

The simulation results shown that the concentrations of neutral radicals and ions (both positive and negative) increase with increasing applied voltage. The results also show that the total concentrations of the negative ions tends to increase as the radial distance from corona wire to the grounded tube electrode increases, while the contrary is true for the positive ions and the neutral radicals. Experimental results have shown that the time averaged corona discharge current increases with increasing gas flow rate. However, this increase is relatively small. Consequently, the gas flow rate have no significant effect on the concentrations of the negative ions, and negligible effect on the concentrations of the positive ions and neutral radicals when compared to the applied voltage effect.

In all the simulations, the negative ion with the highest concentration is $N_2O_2^-$, while the radical with the highest concentration is N_2O. For the positive ion, the species with the highest concentration is N_3O^+ at the lower applied voltage and $N_2O_3^+$ at the higher applied voltage. Also several toxic byproducts like O_3, NO, NO_2, N_2O_4 and N_2O_5 are observed in the simulation results. However, their maximum computed concentrations are within the acceptable limits. The neutral species observed by the present numerical simulations agree qualitatively well with Penetrante's model [1], and the experimental observations of Donohoe et al. [2], Ito et al [3], Masuda et al. [4], Hill et al. [5] and Brahdvold and Martinez [6].

Acknowledgments

The completion of this report would not be possible without the help from many individuals. Therefore, I will wish to take a minute to thank them. First of all, I wish to thank Dr. J.S. Chang for his suggestions. I also wish to thank Dr. F. Pontiga for his patience in explaining his program to me, and for his helps in solving some of the initial problems with the program. Next, I want to thank D. Novog for his suggestions in solving the system of nonlinear equations, and to N. Fukuhara for his help in solving the stack overflow problem with the PC FORTRAN compiler. I also wish to thank P. Looy for his "expert opinion" on the layout of this report. Finally, I wish to thank everyone else in the lab for any of their helps and supports. This work is partly supported by the Natural Sciences and Engineering Council and the NEDO-RITE Program, MITI-Japan.

Table of Contents

List of Figures

List of Tables

1. Introduction

Air pollutants may be induced from a number of different sources, which can either be natural or man-make. Natural air pollutants may be created from forest fires, volcanic eruptions, biological decay, dust storm and/or pollens, while man-make air pollutants may originated from combustion of fossil fuel (power plants and automobiles), or manufacturing processes (factories) [7]. Since the control of the natural pollutants is difficult, it is usually considered as the background pollution [8].

The man-make air pollutants may include both inorganic pollutants and organic pollutants. Inorganic pollutants may include sulfur-containing compounds (e.g. SO_2, H_2S and H_2SO_4), nitrogen-containing compounds (e.g. NO, NO_2, N_2O and NH_3), carbon oxides (e.g. CO and CO_2), halogen and halides (HF, HCl, Cl_2, F_2 and SiF_4), photochemical products (e.g. O_3) and volatile heavy metals (e.g. Hg, Ti and Cd) [7-9]. Organic pollutants may include compounds like paraffines (e.g. methane and ethane), olefins (e.g. ethylene and butadiene), aromatics (e.g. benzene and toluene), aldehydes (e.g. formaldehyde), ketones (e.g. acetone), organic acids (benzoic acid) and alcohols (e.g. methanol) [7,8].

These man-make air pollutants can be damaging in a number of ways [7,8]:

1. It reduces the atmospheric visibility (e.g. smog).
2. It induces economic losses due to damage to buildings and historic sites (e.g. acid rain from sulfur and/or nitrogen containing compounds).
3. It reduces the air quality which can impact human health (e.g. eye irritation, coughing and chest soreness due to the air pollutants, and carcinogenic effects from aromatics compounds like benzene).
4. It damages vegetation and animal's health (acid rain, neurotoxin like mercury and toxin like cadmium).

Consequently, effective control of these air pollutants is essential.

Due to the faster construction time and the lower operational cost, coal fired power plants are employed in many different developed and developing countries for electrical power generation (including United States and Canada). These power plants generated electricity by the mean of coal (or lignite) burning [10]. In this process, the combustion of the coal generates thermal energy (heat), which is then used to boiling water and produces steam. The generated steam can then drive the turbine downstream and produce electricity.

During the combustion process, a number of air pollutants can be produced. The combustion gases such as carbon monoxide (CO), carbon dioxide (CO_2), and methane (CH_4) may cause greenhouse effect which will lead to global warming [9,11]. Also depending on the composition of the coal, NO_x and SO_x can be emitted during combustion. These oxides, when released into the atmosphere, can react with the water vapor and produce acid rain [9,11,12]. Finally, the trace elements contained in the coal may evaporate during the combustion, combined with the fly ashes and released as exhaust [9]. A list of the trace elements contained in three different type of U.S. coal is listed in Table 1.1 [10]. This mixture of exhaust is usually refer to as the flue gas.

Due to their higher demand for oxygen during combustion, the solid fuel such as coal produces higher emission freight that gaseous or liquid fuels [9]. Consequently, better emission control techniques are required. The lower of air pollutants in flue gas can be achieved in two different ways: lower the emission of air pollutants from combustion, or removing the pollutants from the flue gas exhaust (post combustion treatments). Both methods are usually employed simultaneous to improve the overall efficiency.

The reduction of NO_x and SO_x emissions from the flue gas can be achieve by burning coal with lower nitrogen or sulfur components. Similarly, burning coal with lower trace elements compositions should reduce the over all emission of these elements. However, this method may not always be practical due to economic (e.g. transporting the lower sulfur containing coal over a longer distance will increase the transportation cost) and/or natural constraints (e.g. the western U.S. coal shown in Table 1.1 have a lower manganese concentration but a higher barium and strontium concentrations when compared to the eastern and mid-west coal). Finally, effective combustion technique can reduce the combustion-dependent emission such as carbon monoxide and organic carbon to a very low level [9].

Current flue gas cleaning system is usually consist of several different components since different pollutants may have to be removed using different methods. The trace elements may be separated from the flue gas by the wet-scrubber, semi-dry or dry system [9]. Of these three systems, the wet flue gas system is the most versatile because it can also remove a substantial amount of the acidic pollutants from the flue gas [7-10]. The NO_x, SO_x and the remaining combustion-related emissions in the flue gas may be extract by conversing them into harmless gases (e.g. H_2O and N_2), conversing them into useful byproduct(s) (e.g. dry ices) and/or trapping them for later disposal [13].

A number of technologies have been developed over the years to remove the gaseous pollutants from the flue gases. Technology based on the corona discharge processes is one of the next generation techniques for the desulfurization and denitrification of the combustion flue gases generated by the fossil fuel fired power plant. The corona discharge is produced from an electric field generated from the high voltage applied to the active electrode [14-16]. This discharge can generate energetic electrons, oxidizing radicals and ions, which can then be used for the desulfurization, denitrification and even destruction of volatile organic compounds [11-13,17-23].

In this work, a negative dc corona discharge in a coaxial wire–tube electrode configuration is examined numerically. The present corona discharge plasma chemistry model considers the drifting of the ions due to the electric field, the diffusion of all the charged and neutral particles as well as the source and sink terms of the particles using the transport equation [24-26]. Thirty-eight different chemical species are currently simulated in the model, which can be divided into three groups. The first group is the negative ions which includes O^-, O_2^-, O_3^-, O_4^-, NO^-, NO_2^-, NO_3^-, $N_2O_2^-$ and $N_2O_3^-$. The second groups is the neutral species which includes O, O_2, O_3, N, N_2, NO, NO_2, N_2O, NO_3, N_2O_4 and N_2O_5. The third groups is the positive ions which includes O^+, O_2^+, O_4^+, O_6^+, N^+, N_2^+, N_3^+, N_4^+, NO^+, NO_2^+, NO_3^+, NO_4^+, N_2O^+, $N_2O_2^+$, $N_2O_3^+$, $N_2O_4^+$, N_3O^+ and $N_4O_2^+$. The numerical simulation code in this work is programmed using the FORTRAN computer language, and the effects of applied voltage and gas flow rate in dry air condition are examined.

Table 1.1: The amount of trace elements contained in different types of U.S. coal [10].

Element name	Symbol	Analysis Data (PPM)		
		Eastern Coal	Mid-West Coal	Western Coal
Manganese	Mn	200	72	34
Barium	Ba	70	30	300
Strontium	Sr	70	30	100
Fluorine	F	60	58	37
Zirconium	Zr	30	10	15
Boron	B	20	50	70
Vanadium	V	20	20	7
Lithium	Li	18.8	7	4.3
Copper	Cu	16	16.3	7.4
Chromium	Cr	15	10	3
Nickel	Ni	15	18	2
Zinc	Zn	12.8	58	12.8
Arsenic	As	11	12	2
Lead	Pb	10.9	19	4.3
Gallium	Ga	7	2	3
Yttrium	Y	7	7	3
Cobalt	Co	5	7	1.5
Selenium	Se	3.5	2.8	0.5
Niobium	Nb	3	0.7	3
Scandium	Sc	3	3	1.5
Thorium	Th	2.8	1.6	2.4
Beryllium	Be	2	1.5	0.3
Molybdenum	Mo	2	2	1.5
Uranium	U	1	1.4	0.7
Antimony	Sb	0.8	0.8	0.4
Ytterbium	Yb	0.7	0.7	0.3
Cadmium	Cd	0.3	0.12	0.2
Mercury	Hg	0.14	0.1	0.06

2. Literature Review

One possible way to reduce the NO_x, SO_x and greenhouse gases from the flue gas exhaust is by the corona discharge processes. A corona discharge may be defined as a gas discharge in which the ionization processes are restrict to the region around the active electrode(s) [14-16]. A high voltage is applied to the active electrode which generates a large electric field needed for the corona discharge, and some of the gas molecules is ionized or converted into free radicals in the process [14-16]. These ions and free radicals may then react with the NO_x, SO_x and greenhouse gases in the flue gas, either to convert them to harmless or reusable byproduct(s), or to convert them into acids which can be neutralized by the addition of ammonium (NH_3) and collected as ammonium sulfate or ammonium nitrate particles [11,12,17-20]. The feasibility of removing the NO_x and SO_x from the flue gas by the corona discharge method is examined in a number of studies [12,17,18,20].

The first comprehensive microscopic theory of corona discharge is investigated by Belevtser and Biberman [27], while the basic properties of the corona discharge for various electrode configurations have been examined by Goldman et al. [15]. Since then, a number of studies have investigated the corona discharge processes (both positive and negative) numerically. Some of these studies are summarized in Table 2.1. The simulation by Gallimberti [19] demonstrated that the concentration of the neutral radicals generated during the impulse corona discharge in flue gas for a wire-plane electrode configuration is generally larger than the total concentrations of ions (both positive and negative), and the neutral radical with the highest concentration generated is H and OH combined. Another study by Mukkarilli et al. [28] shown that the highest concentration neutral radical generated in a pin-plate type electrode corona discharge in dry air is ozone.

A simulation of parallel plate type electrode for a silent discharge streamer corona in air by Eliasson and Kogelschatz [29] also show that ozone is the neutral species with highest concentration. However, a significant amount of radicals like NO, N_2O, NO_2, NO_3 and N_2O_5 are also produced in the process, although the two highest concentrations among this group of radicals (N_2O and N_2O_5) are still at least two orders of magnitude lower than the ozone concentration. More recent work by Penetrante [1] shows similar results, where the three highest concentrations radicals generated during a pulse corona discharge in air with 400 ppm of NO are O_3, N_2O and N_2O_5. A numerical study by Kulikovsky [30] shows that the dominant radical generated in a positive streamer corona discharge in air is O. However, Kulikovsky's model does not include any ozone reactions. One possible reason for the disagreements among these simulation results is that these models does not include a comprehensive consideration of the ion and radical species reactions that may occur during a corona discharge. Another possible reason is that these models may be simulating different initial conditions (e.g. difference gas composition), different type of corona discharge and/or different electrode geometry.

On the other hand, experimental results of Donohue at al. [2], Ito et al. [3], Masuda et al [4], Hill et al. [5] and Brahdvold and Martines [6] show that N_2O, O_3, NO, NO_2, N_2O_3, N_2O_4 and N_2O_5 are the main corona discharge byproducts, while McDaniel and Crane [31], Lecuille et al. [32], and Goldman et al. [33] observed O_3^- during the corona discharge experiments.

In this work, a negative dc corona discharge in a cylindrical coaxial wire-tube reactor is modelled. Although the dc type corona discharge consumes about tens time more energy that the electron beam or pulsed corona method for desulfurization and denitrification processes [12], the underlying principles between the dc and the pulsed corona discharge are very similar. Therefore, the model developed in this work may be extended in the future for the study of the pulsed corona method, which consumes less electrical power and may be more efficient for desulfurization and denitrification processes (compared to the dc corona method) [12].

The physical model utilized in this work is based on a modified version of the Loeb's model [16], while the chemical model discussed is originally developed by Chang [34-36]. A simplified numerical model which includes most of the negative ions and neutral species discussed in this work have been attempted by Pontiga et al. [37]. However due to the fact that the positive ions are not included in the simulation and any electric field distortion due to spatial charge is neglected, this model does not prove a complete picture of the plasma chemistry in a negative corona discharge. Consequently, an update is needed.

In this work, the positive ions and a new neutral species (N_2O_4) are added to the chemical model in an attempt to improve the accuracy of the simulation. The distortion of the electric field due to the presence of the electron is also included. Finally, the determination of the electron density, and the divergence and Laplacian of the trace particle concentrations is also different from Pontiga et al.'s model [37]. A more detail discussion on the current modelling of the corona discharge in a coaxial wire-tube configuration is examined in Chapter 4.

Table 2.1: A table of numerical studies related to the corona discharge phenomenon

Year	Author	Modelling	Species Considered	Parameters Considered	Ref.
1983	A.A. Belevtser & L.M. Biberman	Positive and negative corona discharge in He	charged and excited helium	electric field	27
1988	I. Gallimberti	Positive DC corona discharge in flue gas	e^-, N, O, CO, H, OH, H_2O, total positive ions, total negative ions	drift velocity, mean energy, ionization and attachment coefficients for electron	19
1988	S. Mukkarilli et al.	Pin-Plate DC corona discharge in dry and wet air	O, O_2, O_3, N_2, NO_x, H_2O	kinetic rate coefficient, electron energy distribution	28
1991	D. Braun et al.	Ozonizers electrical discharge	e^-, O_3	electric field	38
1991	B. Eliasson & U. Kogelschatz	Parallel plane silent discharge in Xe, O_2 and air	O, O_2, O_3, N, N_2, NO, NO_2, NO_3, N_2O, N_2O_5, Xe, Xe_2, Xe^+, Xe_2^+	UV emission and photon generating efficiency in Xe	29
1993	B.M. Penetrante	Power consumption of non-thermal $DeNO_x$ processes	H^-, O^-, O+, H^+, O_2^+, OH^+, N^+, N_2^+, H_2O^+, CO_2^+, H, N, N_2, O, O_2, O_3, CO, CO_2, NO, NO_2, N_2O, N_2O_5, N_2O_4, HNO_2, HNO_3, HO_2NO_2, OH, H_2O, H_2O_2	power consumption	1
1994	P.A. Vitello et al.	Negative parallel plate streamer in nitrogen	e^-, total positive ions, total negative ions	electric field, ions and electron velocities	39
1995	A.A. Kulikovsky	Positive parallel plate streamer in N_2	e^-	electric field, photo-ionization rate	40

Table 2.1: Continue

Year	Author	Modelling	Species Considered	Parameters Considered	Ref.
1995	F. Tochikubo et al.	Positive coaxial wire steamer propagation	O, O_2, O_3, N, N_2, NO, NO_2, NO_3	ionization rate, electric field	41
1996	R. Morrow & J.J. Lowke	Positive parallel plate pulsed corona in air	e^-, total positive ions, total negative ions	electric potential, electric field, ionization rate	42
1996	A.A. Kulikovsky	Positive parallel plate streamer in air	e^-	electric field, space charge, streamer radius & velocity	43
1997	A.A. Kulikovsky	Positive parallel plate streamer in air with external field	e^-	ionization rate, steamer spatial and electric field temporal evolution	44
1997	A.A. Kulikovsky	Positive point plate streamer in air	e^-, O, N, N_2, OH	electric field, streamer radius and velocity, dissociation rate	30
1997	F. Pontiga et al.	Negative coaxial wire corona discharge in O_2	e^-, O^-, O_2^-, O_2^+, O, O_3	N/A	45
1997	present	Negative DC corona discharge in dry air	e^-, O^-, O_2^-, O_3^-, O_4^-, NO^-, NO_2^-, NO_3^-, $N_2O_2^-$, $N_2O_3^-$, O, O_2, O_3, N, N_2, NO, NO_2, N_2O, NO_3, N_2O_4, N_2O_5, O^+, O_2^+, O_4^+, O_6^+, N^+, N_2^+, N_3^+, N_4^+, NO^+, NO_2^+, NO_3^+, NO_4^+, N_2O^+, $N_2O_2^+$, $N_2O_3^+$, $N_2O_4^+$, N_3O^+, $N_4O_2^+$	electric field, electron temperature and ionization rate	

3. Coaxial Wire-Tube Electrodes Corona Discharge Characteristics

For completeness, this chapter will review the coaxial wire-tube electrode corona discharge system modelled for this numerical study. The first section of this chapter will discuss the experimental apparatus. The second section will examines the time averaged corona discharge current-voltage characteristic obtained from this coaxial wire-tube electrode configuration, which are utilized as the inputs for the numerical model.

3.1. Experimental Apparatus

A schematic of the coaxial wire-tube corona discharge experimental apparatus [46] is shown in Figure 3.1.1. The active electrode here is the corona wire, while the grounded electrode is the outer cylindrical tube. The length of the grounded electrode is 18.01 cm, with a radius (outer radius) of 1.78 cm. A smooth wire with radius (r_l) of 0.038 cm is utilized as the active electrode. The electrometer in Figure 3.1.1 is intended to measure the discharge current.

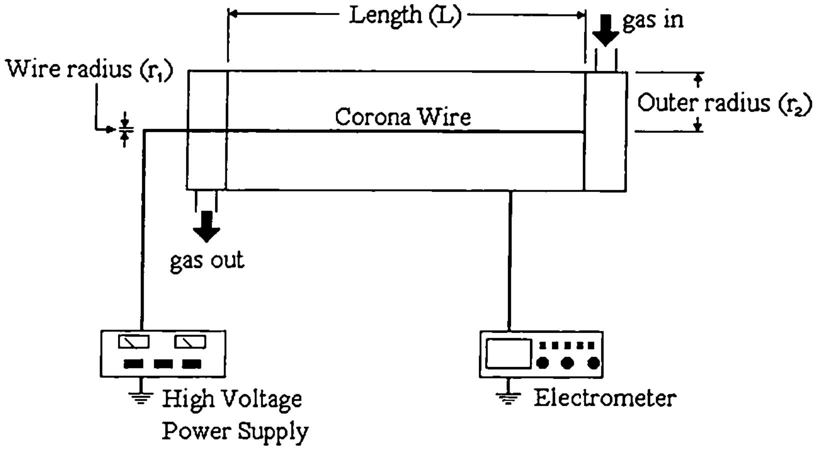

Figure 3.1.1: Schematic of the coaxial wire–tube corona discharge experimental apparatus

3.2. Current-Voltage Characteristics

In this work, only the negative dc corona discharge is investigated. A typical time averaged current-voltage characteristics obtained by Chang et al. [46] is shown in Figure 3.2.1. For the current experimental setup, the corona discharge (without gas flow) breakdown at an applied voltage of about –20 kV, with the time averaged discharge current increases with increasing applied voltage. The discharge current as a function of the gas flow rate at an applied voltage of –18.0 kV is shown in Figure 3.2.2 [46,47]. From this figure, one can observe that the time averaged discharge current tends to increase linearly as the flow rate increases. For the fixed applied voltage of –18.0 kV, the saturated points seems to occur at about 1.5 L/min, and further increase in gas flow rate after this points (2.0 L/min) have no significant effect on the time averaged discharge current.

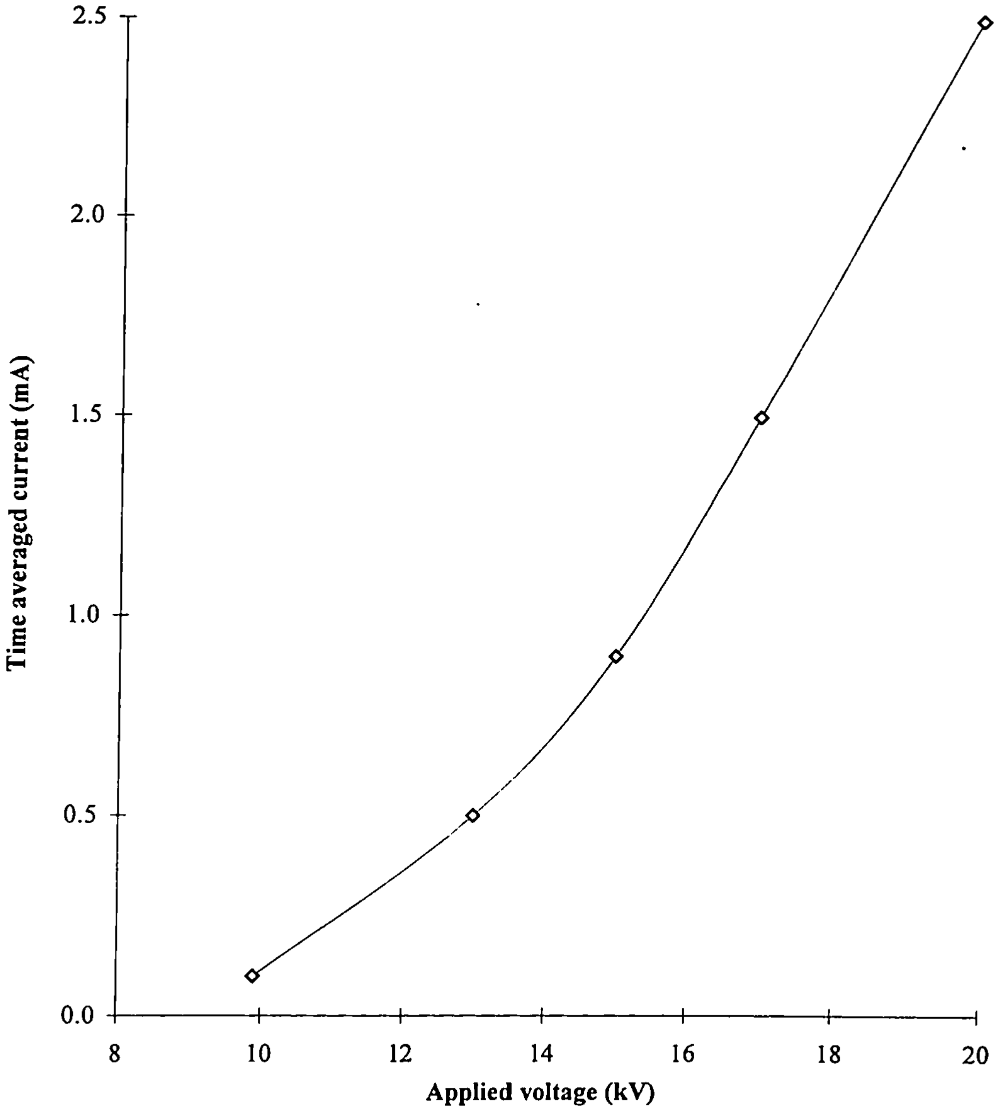

Figure 3.2.1: The time averaged current-voltage characteristics of the coaxial wire-tube electrode corona discharge without gas flow

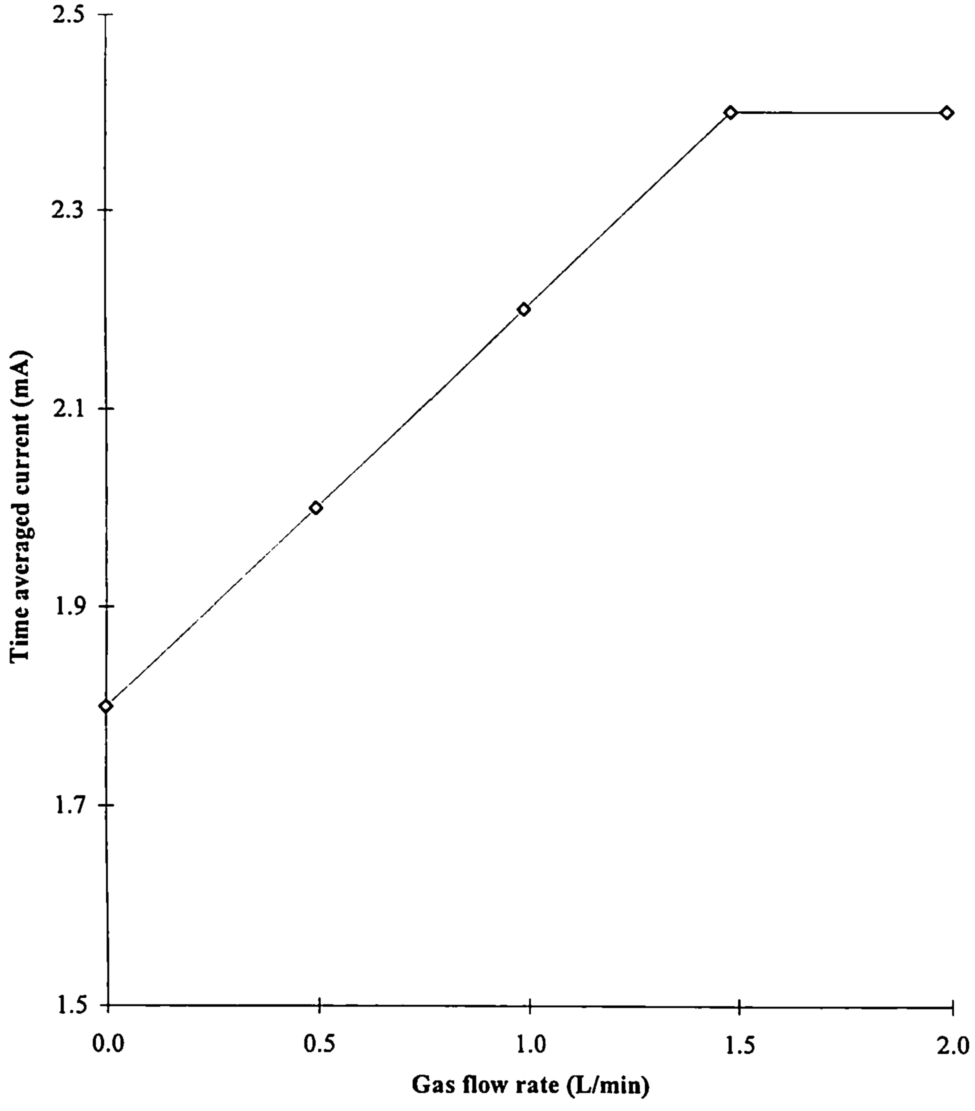

Figure 3.2.2: The time averaged current as a function of gas flow rate at a fixed applied voltage of −18 kV

4. Modelling of the Corona Discharge

The method for modelling the negative dc corona discharge in dry air for a coaxial wire-tube electrodes configuration will be presented in this chapter, which is divided into five sections. The first section examines the governing equations behind the numerical model, and the second section discusses the physical model of the corona discharge. The chemical model for a 79% N_2–21% O_2 (dry air) system is examined in the third section, while the estimation of the transport coefficients for the ions and neutral radicals are discussed in the fourth section. Finally the strategy for achieving convergence in these numerical simulations is discussed in the last section.

4.1. Governing Equations

Since an electric field will exist inside the corona reactor due to the high voltage applied to the active electrode, the continuity equations and the charged particle transport equations are required to be solved simultaneous with the Poisson equations for the charged particles [26]. The continuity equation for species *k* is:

$$\nabla \cdot \vec{J}_k = -\frac{d[n_k]}{dt} + S_o - S_i \tag{4.1.1}$$

where the subscripts *k* refer to different ions or neutrals. $\vec{J}$ is the particle flux density and *n* is the particle density. The terms S_o and S_i are the production and loss rate of particle *k* by chemical reactions. For steady-state:

$$\frac{d[n_k]}{dt} = 0 \tag{4.1.2}$$

This will simplifies Equation 4.1.1 to:

$$S_o - S_i - \nabla \cdot \vec{J}_k = 0 \tag{4.1.3}$$

The charged particle transport equation for species *k* is:

$$\vec{J}_k = n_k \vec{U}_g \pm \mu_k n_k \vec{E} - D_k \nabla n_k - G_k n_k \nabla T_g \tag{4.1.4}$$

where the subscript *g* refers to bulk gas. $\vec{U}$ is the velocity, μ is the mobility, $\vec{E}$ is the electric field, *D* is the diffusion coefficient, *G* is the thermophoresis coefficient and *T* is the temperature [26].

4.2. Physical Model of the Corona Discharge

In Equation 4.1.4, the transport of charged particles by gas convection (the first right hand side term) is assumed to be small when compared with the other terms in the present corona discharged conditions [46]. The second term is the influence of the electric field on the mobility of the charged particles. The sign for this term is determined by the charge of the ions. The sign on the top is for the positive ions, while the sign at the bottom is for the negative ions. The third term represents the particle flux created by diffusion, and the last term is the thermophoresis flux produced by the inhomogeneities in spatial temperature [48]. The contribution of this last term to the total flux is also assume to be small due to the small power consumption in the corona discharge process [46], and will be neglected in the present model. This will simplifies the transport equation to:

$$\vec{J}_k = \pm\, \mu_k\, n_k \vec{E} - D_k \nabla n_k \tag{4.2.1}$$

Taking the divergence on both side and assuming μ_k is constant produces:

$$\nabla \cdot \vec{J}_k = \pm\, \mu_k\, \nabla \cdot \left(n_k \vec{E}\right) - D_k \nabla^2 n_k \tag{4.2.2}$$

Combining Equation 4.1.3 and 4.2.2 yields:

$$S_o - S_l \mp \mu_k\, \nabla \cdot \left(n_k \vec{E}\right) + D_k \nabla^2 n_k = 0 \tag{4.2.3}$$

or,

$$S_o - S_l \mp \mu_k n_k \nabla \cdot \vec{E} \mp \mu_k \vec{E}\, \nabla \cdot n_k + D_k \nabla^2 n_k = 0 \tag{4.2.4}$$

Equation 4.2.4 applies only to charged particles. For neutral species, the electric field should have no effect and Equation 4.2.4 will reduce to:

$$S_o - S_i + D_k \nabla^2 n_k = 0 \tag{4.2.5}$$

Since the corona reactor is in a cylindrical configuration and the current model assumes no angular or axial dependence, the cylindrical coordinates system with only radial dependence will be considered in the calculations.

To calculate the divergence of the electric field ($\nabla \cdot \vec{E}$), one may wish to start by considering the total charge flux (j_t):

$$j_t \approx \pm e\vec{E}\left(\mu_e n_e + \sum_i \mu_i n_i\right) \tag{4.2.6}$$

where e is the unit charge (C), $\vec{E}$ is the electric field (V/cm), μ is the mobility of the charged particles (cm^2/Vs), n is the concentration of the charge particles (cm^{-3}) and the subscript i stands for different ions. Since there are two different types of ions, the top sign (+) is used for the positive ions and the bottom sign (–) is used for the negative ions and electron.

Because the voltage applied is negative and the electron mobility is much larger than the ionic mobility, one may assume that:

$$\mu_e n_e >> \sum_a \mu_a n_a \ or \ \sum_c \mu_c n_c \tag{4.2.7}$$

when,

$$n_e \approx \sum_a n_a \ or \ \sum_c n_c \tag{4.2.8}$$

here the subscript a represents the negative ions and the subscript c represents the positive ions. With Equation 4.2.7, the total charge flux can be approximated as [49]:

$$j \approx -e\bar{E}\mu_e n_e \tag{4.2.9}$$

In the cylindrical coordinate system, this yield a total current (I) of:

$$I \approx -2\pi\, r L e \bar{E}\mu_e n_e \tag{4.2.10}$$

here r is the radial distance (cm) and L is the length (cm) of the corona wire. Rearranging Equation 4.2.10 gives:

$$n_e \approx \frac{-I}{2\pi r L e \bar{E}\mu_e} \tag{4.2.11}$$

The differential form of the Poisson's equation can be stated as [50]:

$$\nabla \cdot \vec{E} = \frac{-en_e \pm e\sum_i n_i}{\varepsilon} \tag{4.2.12}$$

where ε is the dielectric constant (C/V·cm). By assuming the density of the electron is much greater that the sum of the ion concentrations (both positive and negative), Equation 4.2.12 will simplifies to :

$$\nabla \cdot \vec{E} = \frac{-e n_e}{\varepsilon} \tag{4.2.13}$$

In the cylindrical coordinate system with no angular or axial dependence, the divergence of the electric field can be computed as:

$$\nabla \cdot \vec{E} = \frac{\vec{E}}{r} + \frac{d\vec{E}}{dr} \tag{4.2.14}$$

Combining Equation 4.2.13 and 4.2.14 yields:

$$\frac{\vec{E}}{r}+\frac{d\vec{E}}{dr}=\frac{-en_e}{\varepsilon} \tag{4.2.15}$$

or,

$$\frac{d\vec{E}}{dr}=\frac{-en_e}{\varepsilon}-\frac{\vec{E}}{r} \tag{4.2.16}$$

Next, one can combine Equation 4.2.11 and 4.2.16 to eliminate the electron density:

$$\frac{d\vec{E}}{dr}=\frac{I}{2\pi rL\varepsilon\vec{E}\mu_e}-\frac{\vec{E}}{r} \tag{4.2.17}$$

Since the electron mobility (μ_e) is a function of the electric field, this relationship is required for solving Equation 4.2.17. The electron mobility may be approximated by fitting a curve through experimental data. The data utilized here is from Table 14.18 in Huxley and Crompton [51], and the best fitted curve for the respective experimental data is shown in Figure 4.2.1.

From Figure 4.2.1, one obtains that:

$$\mu_e=40110\left|\vec{E}\right|^{-0.501} \tag{4.2.18}$$

where μ_e is in cm^2/Vs and $\vec{E}$ is in V/cm. Substituting Equation 4.2.18 into Equation 4.2.17 yields:

$$\frac{d\vec{E}}{dr}=\frac{-I}{80220\pi rL\varepsilon\left|\vec{E}\right|^{0.499}}+\frac{\left|\vec{E}\right|}{r} \tag{4.2.19}$$

Next, one may want to introduce a constant Γ :

$$\Gamma = \frac{-I}{80220\pi\varepsilon L} \tag{4.2.20}$$

This will reduces Equation 4.2.19 to:

$$\frac{d\bar{E}}{dr} = \frac{\Gamma}{r\left|\bar{E}\right|^{0.499}} + \frac{\left|\bar{E}\right|}{r} \tag{4.2.21}$$

The solution to Equation 4.2.21 is:

$$\left|\bar{E}\right| = \left(\Gamma - \frac{\alpha}{r^{\omega}}\right)^{\frac{1}{\omega}} \tag{4.2.22}$$

where ω is equal to 1.499 and α is the constant of integration. To determine α, one can apply the following [52]:

$$\left|V_a\right| = \int_{r_1}^{r_2} \left|\bar{E}\right| dr \tag{4.2.23}$$

Here V_a is the voltage applied to the corona wire, while r_1 and r_2 are the radius of the corona wire and coaxial tube respectively. Since the integration in Equation 4.2.23 can not be easily solve analytically, a numerical iteration method is developed to calculate α. In this method, α is initially assigned some arbitrary value. This value is then used to calculate the electric field, which can then be use to compute the applied voltage with numerical integration. This calculated applied voltage is then compared with the experimental applied voltage, and the value of α is adjusted accordingly until the calculated applied voltage is in close agreement with the experimental result. Once α is computed, the electron density and the magnitude of the electric field can be calculated using Equation 4.2.11 and 4.2.22 respectively. After the electron density is determined, the divergence of the electric field can be calculated using Equation 4.2.13 and substituted back into Equation 4.2.4.

The next step is to determine the divergence of the ions density ($\nabla \cdot n_k$) and the Laplacian of the particles (including charged particles) density ($\nabla^2 n_k$). Since these densities are what one try to compute in this simulation, approximations for this two terms are employed. In the present model, it is assume that the radial dependence of the particles density can be approximated using the radial electron density profile as follows:

$$\begin{aligned}\nabla \cdot n_k &= \frac{n_e^r - n_e^{r-\Delta r}}{\Delta r} \\ &\approx \frac{n_k}{n_e}\frac{n_e^r - n_e^{r-\Delta r}}{\Delta r}\end{aligned} \tag{4.2.24}$$

and,

$$\begin{aligned}\nabla^2 n_k &= -\left(\frac{1}{r}\frac{n_e^r - n_e^{r-\Delta r}}{\Delta r} + \frac{n_e^{r+\Delta r} + n_e^{r-\Delta r} - 2n_e^r}{\Delta r^2}\right) \\ &\approx -\frac{n_k}{n_e}\left(\frac{1}{r}\frac{n_e^r - n_e^{r-\Delta r}}{\Delta r} + \frac{n_e^{r+\Delta r} + n_e^{r-\Delta r} - 2n_e^r}{\Delta r^2}\right)\end{aligned} \tag{4.2.25}$$

Here, the subscript e indicates the electron density is utilized in the computations, which can be calculated using Equation 4.2.11. The superscript on n indicates the radial position of the electron density and Δr is the radial step size. The radial step for all the divergence and Laplacian computations in this report is taken to be 0.0109 cm unless otherwise stated.

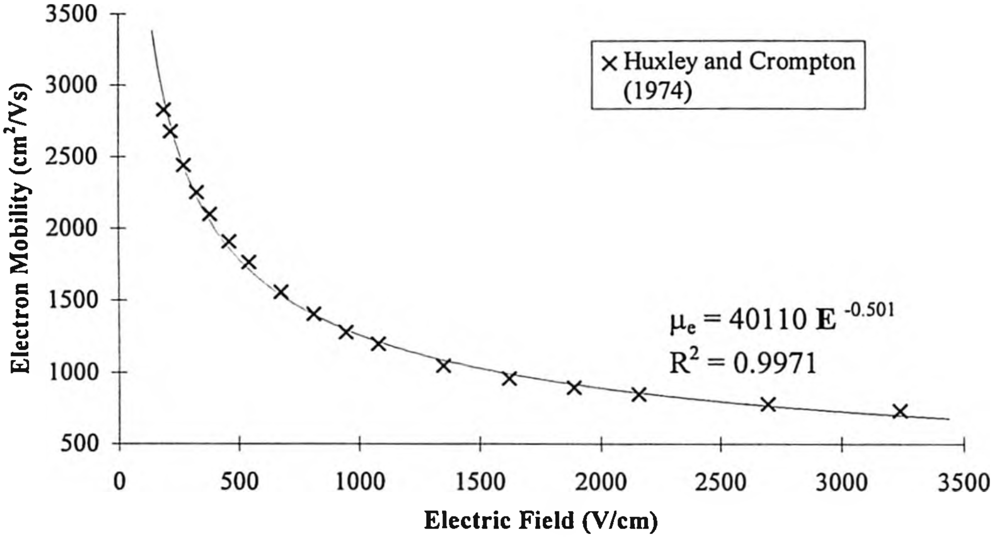

Figure 4.2.1: The electron mobility as a function of the electric field in air

4.3. Chemical Model of N_2–O_2 System

The calculation for the production and loss rates of particle *k* by chemical reactions will be considered in this section. The source (S_o) and sink (S_l) terms in Equations 4.2.4 and 4.2.5 can be computed by consider the rate of the chemical reactions occurring inside the corona reactor. For the current model, two- and three-body collision reactions between neutral radicals, positive ions, negative ions and electron are considered. For the two-body reactions, the chemical reaction can be stated as:

$$\mathrm{A} + \mathrm{B} \xrightarrow{k_2} \mathrm{C} + \mathrm{D}\,(+\mathrm{E}\ +....) \tag{4.3.1}$$

The rate of decrease in the concentration of species A or B can be expressed as [53]:

$$\frac{d[\mathrm{X}]}{dt} = -k_2\,[\mathrm{A}][\mathrm{B}] \tag{4.3.2}$$

while the rate of increase for species C or D (and any other product(s) of reaction) can be determined by:

$$\frac{d[\mathrm{X}]}{dt} = k_2\,[\mathrm{A}][\mathrm{B}] \tag{4.3.3}$$

here [X] represents the concentration of species A or B in Equation 4.3.2 and the concentration of species C or D (or and other product(s) of reaction) in Equation 4.3.3, while k_2 represents the reaction rate coefficient for the two-body reaction.

For the three-body reaction with the third body (M), the chemical reaction is:

$$A + B + M \xrightarrow{k_3} C + D\,(+ \ldots.) + M \qquad (4.3.4)$$

Again, the rate of decrease in the concentration of species A or B can be expressed as [53]:

$$\frac{d[\mathrm{X}]}{dt} = -k_3\,[\mathrm{A}][\mathrm{B}][\mathrm{M}] \qquad (4.3.5)$$

while the rate of increase for species C or D (and any other product(s) of reaction) can be determined by:

$$\frac{d[\mathrm{X}]}{dt} = k_3\,[\mathrm{A}][\mathrm{B}][\mathrm{M}] \qquad (4.3.6)$$

here k_3 represents the reaction rate coefficient for the three-body reaction, while [M] is the concentration of the third body particle.

In the present model, the concentration of this third body is assumed to be 2.463×10^{19} cm^{-3}, while the concentrations of the O_2 and N_2 (in dry air) are assumed to be 5.1723×10^{18} cm^{-3} and 1.94577×10^{19} cm^{-3} respectively. A complete list of the chemical reactions considered in this model with their respectively reaction rate is listed in Table 4.3.1 and Table 4.3.2 at the end of this section [25,26,34-36,54-64], while the block diagrams for the chemical reactions of the radicals, negative and positive ions are shown in Figures 4.3.1 to 4.3.3.

Table 4.3.1: Neutrals and ions reactions with reaction rates

Chemical Reaction	Reaction Rate	Ref.
$N_2O_5 + M \rightarrow NO_3 + NO_2 + M$	$k_1 = 2.60 \times 10^{-19}$	56
$NO + N \rightarrow O + N_2$	$k_2 = 3.10 \times 10^{-11}$	57
$NO^- + N_2O \rightarrow e^- + NO + N_2O$	$k_3 = 5.10 \times 10^{-12}$	55
$NO^- + NO \rightarrow e^- + NO + NO$	$k_4 = 5.00 \times 10^{-12}$	55
$NO_2 + N \rightarrow O + N_2O$	$k_5 = 1.40 \times 10^{-12}$	57
$NO_2 + NO^- \rightarrow NO_2^- + NO$	$k_6 = 7.40 \times 10^{-10}$	55
$NO_2^- + N_2O \rightarrow NO_3^- + N_2$	$k_7 = 1.00 \times 10^{-12}$	55
$NO_2^- + N_2O_5 \rightarrow NO_3^- + NO_2 + NO_2$	$k_8 = 7.00 \times 10^{-10}$	55
$NO_2^- + NO_2 \rightarrow NO_3^- + NO$	$k_9 = 2.00 \times 10^{-13}$	63
$NO_3 + NO \rightarrow NO_2 + NO_2$	$k_{10} = 2.60\times 10^{-11}$	56
$NO_3 + NO_2 + M \rightarrow N_2O_5 + M$	$k_{11} = 7.30 \times 10^{-32}$	56
$NO_3^- + NO \rightarrow NO_2^- + NO_2$	$k_{12} = 1.00 \times 10^{-12}$	55
$O + N_2O_5 \rightarrow O_2 + NO_2 + NO_2$	$k_{13} = 3.00 \times 10^{-16}$	57
$O + NO + M \rightarrow NO_2 + M$	$k_{14} = 9.00 \times 10^{-32}$	57
$O + NO_2 \rightarrow O_2 + NO$	$k_{15} = 9.70 \times 10^{-12}$	57
$O + NO_2 + M \rightarrow NO_3 + M$	$k_{16} = 7.90 \times 10^{-32}$	35
$O + NO_3 \rightarrow O_2 + NO_2$	$k_{17} = 1.70 \times 10^{-11}$	56
$O + NO_3^- \rightarrow O_2 + NO_2^-$	$k_{18} = 2.50 \times 10^{-12}$	55
$O + NO_3^- \rightarrow O_2^- + NO_2$	$k_{19} = 2.50 \times 10^{-12}$	55
$O + NO_3^- \rightarrow O_3^- + NO$	$k_{20} = 2.50 \times 10^{-12}$	55
$O + NO_3^- \rightarrow e^- + O_2 + NO_2$	$k_{21} = 2.50 \times 10^{-12}$	55
$O + O + M \rightarrow O_2 + M$	$k_{22} = 8.00 \times 10^{-33}$	62
$O^- + N \rightarrow e^- + NO$	$k_{23} = 2.20 \times 10^{-10}$	55
$O^- + N_2 \rightarrow e^- + N_2O$	$k_{24} = 1.00 \times 10^{-12}$	55
$O^- + N_2 + M \rightarrow NO_2^- + M$	$k_{25} = 4.00 \times 10^{-31}$	55
$O^- + N_2O \rightarrow NO^- + NO$	$k_{26} = 2.00 \times 10^{-10}$	55
$O^- + NO \rightarrow e^- + NO_2$	$k_{27} = 2.80 \times 10^{-10}$	55
$O^- + NO_2 \rightarrow O + NO_2^-$	$k_{28} = 1.00 \times 10^{-09}$	55
$O^- + O \rightarrow e^- + O_2$	$k_{29} = 1.90 \times 10^{-10}$	63
$O_2 + N \rightarrow O + NO$	$k_{30} = 8.90 \times 10^{-17}$	57
$O_2 + NO + NO \rightarrow NO_2 + NO_2$	$k_{31} = 2.00 \times 10^{-38}$	62
$O_2 + NO^- \rightarrow O_2^- + NO$	$k_{32} = 5.00 \times 10^{-10}$	63
$O_2 + O + M \rightarrow O_3 + M$	$k_{33} = 6.00 \times 10^{-34}$	62
$O_2 + O^- \rightarrow e^- + O_3$	$k_{34} = 1.00 \times 10^{-12}$	55
$O_2 + O_2 + O^- \rightarrow O_3^- + O_2$	$k_{35} = 1.10 \times 10^{-30}$	58

Table 4.3.1: Continue

Chemical Reaction	Rate Constant	Ref.
$O_2^- + N \rightarrow e^- + NO_2$	$k_{36} = 4.00 \times 10^{-10}$	55
$O_2^- + N_2 \rightarrow e^- + N_2 + O_2$	$k_{37} = 1.10 \times 10^{-19}$	55
$O_2^- + N_2 + M \rightarrow N_2O_2^- + M$	$k_{38} = 4.00 \times 10^{-33}$	55
$O_2^- + N_2O \rightarrow NO_2^- + NO$	$k_{39} = 2.00 \times 10^{-14}$	55
$O_2^- + N_2O \rightarrow O_3^- + N_2$	$k_{40} = 2.00 \times 10^{-14}$	55
$O_2^- + NO_2 \rightarrow O_2 + NO_2^-$	$k_{41} = 7.00 \times 10^{-10}$	55
$O_2^- + O \rightarrow O_2 + O^-$	$k_{42} = 1.50 \times 10^{-10}$	55
$O_2^- + O \rightarrow e^- + O_3$	$k_{43} = 1.50 \times 10^{-10}$	63
$O_2^- + O_2 \rightarrow e^- + O_2 + O_2$	$k_{44} = 2.20 \times 10^{-18}$	55
$O_2^- + O_2 + M \rightarrow O_4^- + M$	$k_{45} = 3.40 \times 10^{-32}$	55
$O_3 + M \rightarrow O_2 + O + M$	$k_{46} = 1.77 \times 10^{-26}$	56
$O_3 + N \rightarrow O_2 + NO$	$k_{47} = 2.30 \times 10^{-26}$	62
$O_3 + NO \rightarrow O_2 + NO_2$	$k_{48} = 1.80 \times 10^{-14}$	26
$O_3 + NO_2 \rightarrow O_2 + NO_3$	$k_{49} = 3.20 \times 10^{-17}$	56
$O_3 + NO_2^- \rightarrow O_2 + NO_3^-$	$k_{50} = 1.20 \times 10^{-10}$	55
$O_3 + NO_3^- \rightarrow O_2 + O_2 + NO_2^-$	$k_{51} = 1.00 \times 10^{-13}$	55
$O_3 + O \rightarrow O_2 + O_2$	$k_{52} = 8.00 \times 10^{-15}$	56
$O_3 + O^- \rightarrow O_3^- + O$	$k_{53} = 8.00 \times 10^{-10}$	55
$O_3 + O_2^- \rightarrow O_3^- + O_2$	$k_{54} = 6.00 \times 10^{-10}$	55
$O_3^- + M \rightarrow e^- + O_3 + M$	$k_{55} = 2.30 \times 10^{-11}$	58
$O_3^- + N_2 + N_2 \rightarrow N_2O_3^- + N_2$	$k_{56} = 8.00 \times 10^{-32}$	55
$O_3^- + N_2O \rightarrow NO_3^- + NO$	$k_{57} = 1.00 \times 10^{-15}$	55
$O_3^- + N_2O \rightarrow O_2^- + O_2 + N_2$	$k_{58} = 6.30 \times 10^{-15}$	55
$O_3^- + N_2O \rightarrow O_4^- + N_2$	$k_{59} = 6.30 \times 10^{-15}$	55
$O_3^- + N_2O \rightarrow e^- + O_2 + O_2 + N_2$	$k_{60} = 6.30 \times 10^{-15}$	55
$O_3^- + NO \rightarrow O + NO_3^-$	$k_{61} = 1.10 \times 10^{-12}$	55
$O_3^- + NO \rightarrow O_2 + NO_2^-$	$k_{62} = 1.10 \times 10^{-12}$	63
$O_3^- + NO_2 \rightarrow O_2 + NO_3^-$	$k_{63} = 2.80 \times 10^{-10}$	55
$O_3^- + O \rightarrow O_2^- + O_2$	$k_{64} = 2.50 \times 10^{-10}$	63
$O_4^- + N_2 \rightarrow O_2 + N_2O_2^-$	$k_{65} = 1.00 \times 10^{-11}$	55
$O_4^- + N_2O \rightarrow O_2 + N_2O_3^-$	$k_{66} = 1.00 \times 10^{-12}$	55
$O_4^- + NO \rightarrow O_2 + NO_3^-$	$k_{67} = 2.50 \times 10^{-10}$	55
$O_4^- + O \rightarrow O_3^- + O_2$	$k_{68} = 4.00 \times 10^{-10}$	55
$NO^- + X^+ \rightarrow m(O_2 + N_2)$	$k_{69} = 1.00 \times 10^{-06}$	*
$NO_2^- + NO^+ \rightarrow N_2O_3$	$k_{70} = 6.40 \times 10^{-06}$	26
$NO_3^- + NO^+ \rightarrow N_2O_4$	$k_{71} = 5.70 \times 10^{-06}$	*
$O_2^- + O_4^+ \rightarrow O_2 + O_2 + O_2$	$k_{72} = 4.20 \times 10^{-07}$	*

Table 4.3.1: Continue

Chemical Reaction	Rate Constant	Ref.
$O_2^- + N_2^+ \rightarrow O_2 + N_2$	$k_{73} = 2.00 \times 10^{-06}$	*
$O_2^- + O_2^+ \rightarrow O_2 + O_2$	$k_{74} = 2.00 \times 10^{-07}$	58
$O_3^- + X^+ \rightarrow m(O_2 + N_2)$	$k_{75} = 1.00 \times 10^{-06}$	*
$O^- + O^+ \rightarrow O_2$	$k_{76} = 1.10 \times 10^{-07}$	*
$O^- + N^+ \rightarrow NO$	$k_{77} = 1.80 \times 10^{-07}$	*
$N_2O_2^- + X^+ \rightarrow m(O_2 + N_2)$	$k_{78} = 1.00 \times 10^{-06}$	*
$O_4^- + X^+ \rightarrow m(O_2 + N_2)$	$k_{79} = 1.00 \times 10^{-06}$	*
$N_2O_3^- + X^+ \rightarrow m(O_2 + N_2)$	$k_{80} = 1.00 \times 10^{-06}$	*
$N_2O_5 + NO^+ \rightarrow N_2O_4 + NO_2^+$	$k_{81} = 5.90 \times 10^{-10}$	55
$N_2O_5 + O_2^+ \rightarrow NO_2^+ + NO_3 + O_2$	$k_{82} = 8.80 \times 10^{-10}$	63
$NO + NO_2^+ \rightarrow NO^+ + NO_2$	$k_{83} = 2.90 \times 10^{-10}$	63
$NO_2 + O^+ \rightarrow NO_2^+ + O$	$k_{84} = 1.60 \times 10^{-09}$	63
$O_2 + N^+ \rightarrow NO + O^+$	$k_{85} = 3.60 \times 10^{-11}$	63
$O_2^+ + N_2 \rightarrow NO + NO^+$	$k_{86} = 1.00 \times 10^{-15}$	55
$N + NO_2^+ \rightarrow NO + NO^+$	$k_{87} = 8.00 \times 10^{-12}$	55
$NO + N^+ \rightarrow N + NO^+$	$k_{88} = 9.00 \times 10^{-10}$	55
$NO + N_2^+ \rightarrow N_2 + NO^+$	$k_{89} = 3.30 \times 10^{-10}$	63
$NO + O^+ \rightarrow O + NO^+$	$k_{90} = 1.70 \times 10^{-12}$	55
$NO + O_2^+ \rightarrow O_2 + NO^+$	$k_{91} = 4.50 \times 10^{-10}$	55
$NO + N_3^+ \rightarrow N_2 + N_2O^+$	$k_{92} = 7.00 \times 10^{-11}$	55
$NO + N_3^+ \rightarrow N + N_2 + NO^+$	$k_{93} = 7.00 \times 10^{-11}$	55
$O + N_2^+ \rightarrow N + NO^+$	$k_{94} = 1.40 \times 10^{-10}$	63
$N_2 + O^+ \rightarrow N + NO^+$	$k_{95} = 1.20 \times 10^{-12}$	63
$N + O_2^+ \rightarrow O + NO^+$	$k_{96} = 1.20 \times 10^{-10}$	55
$O_2 + N^+ \rightarrow O + NO^+$	$k_{97} = 2.60 \times 10^{-09}$	55
$N_2O + O^+ \rightarrow O + N_2O^+$	$k_{98} = 3.00 \times 10^{-10}$	55
$O + N_2^+ \rightarrow N_2 + O^+$	$k_{99} = 5.40 \times 10^{-12}$	55
$O + NO_2^+ \rightarrow O_2 + NO^+$	$k_{100} = 8.00 \times 10^{-12}$	55
$O_2 + N_2O_3^+ \rightarrow N_2O + O_4^+$	$k_{101} = 1.90 \times 10^{-13}$	55
$O_2 + N_3^+ \rightarrow N_2O + NO^+$	$k_{102} = 3.30 \times 10^{-11}$	55
$N_2O + N_2^+ \rightarrow N_2 + N_2O^+$	$k_{103} = 7.00 \times 10^{-10}$	55
$O_3 + NO^+ \rightarrow O_2 + NO_2^+$	$k_{104} = 1.00 \times 10^{-14}$	63
$N_2 + N_2O_2^+ + M \rightarrow N_4O_2^+ + M$	$k_{105} = 1.00 \times 10^{-29}$	55
$N_2 + N_2 + NO^+ \rightarrow N_2 + N_3O^+$	$k_{106} = 1.00 \times 10^{-30}$	55
$N_2 + O_4^+ + M \rightarrow N_2O_4^+ + M$	$k_{107} = 1.00 \times 10^{-29}$	55
$O_3 + NO^+ + M \rightarrow NO_4^+ + M$	$k_{108} = 1.00 \times 10^{-29}$	55
$N_2 + O_2 + NO^+ \rightarrow N_2 + NO_3^+$	$k_{109} = 3.00 \times 10^{-31}$	55

Table 4.3.1: Continue

Chemical Reaction			Rate Constant	Ref.
$N_2O_5 + NO_2^+$	→	$N_2O_4 + NO_3^+$	$k_{110} = 1.00 \times 10^{-11}$	55
$N_2 + N_2 + N_2^+$	→	$N_2 + N_4^+$	$k_{111} = 1.10 \times 10^{-29}$	55
$O_2 + N_2^+$	→	$N_2 + O_2^+$	$k_{112} = 6.50 \times 10^{-11}$	55
$O_2 + N^+$	→	$N + O_2^+$	$k_{113} = 3.10 \times 10^{-10}$	55
$N_2 + N_2 + N^+$	→	$N_2 + N_3^+$	$k_{114} = 5.20 \times 10^{-30}$	55
$N_2 + N_2^+$	→	$N + N_3^+$	$k_{115} = 5.70 \times 10^{-11}$	55
$O_2 + N_3^+$	→	$N_2 + NO_2^+$	$k_{116} = 4.40 \times 10^{-11}$	55
$O_2 + O_4^+ + M$	→	$O_6^+ + M$	$k_{117} = 5.00 \times 10^{-30}$	55
$O_2 + O_2 + O_2^+$	→	$O_2 + O_4^+$	$k_{118} = 2.50 \times 10^{-30}$	55
$N_2O + O_4^+$	→	$O_2 + N_2O_3^+$	$k_{119} = 2.50 \times 10^{-10}$	55
$O_2 + N_4^+$	→	$N_2 + N_2 + O_2^+$	$k_{120} = 4.00 \times 10^{-10}$	55
$N_2O + O_2^+ + M$	→	$N_2O_3^+ + M$	$k_{121} = 5.20 \times 10^{-29}$	55
$NO + NO^+ + M$	→	$N_2O_2^+ + M$	$k_{122} = 5.00 \times 10^{-10}/[M]$	35
$N_2 + N_2 + O_2^+$	→	$N_2 + N_2O_2^+$	$k_{123} = 8.00 \times 10^{-31}$	55
$N_2 + N_2O_2^+$	→	$N_2 + N_2 + O_2^+$	$k_{124} = 2.00 \times 10^{-11}$	55
$O_2 + N_2O_2^+$	→	$N_2 + O_4^+$	$k_{125} = 5.00 \times 10^{-11}$	55
$NO_3 + NO_3$	→	$N_2O + O_2 + O_3$	$k_{126} = 1.00 \times 10^{-16}$	62
$N^* + NO_2$	→	$NO + NO$	$k_{127} = 0.0$	N/A
$N^* + NO_2$	→	$N_2O + O$	$k_{128} = 0.0$	N/A
$N^* + NO_2$	→	$N_2 + O_2$	$k_{129} = 0.0$	N/A
$N^* + NO_2$	→	$N_2 + O + O$	$k_{130} = 0.0$	N/A
$N_2O + O_3^-$	→	$O_2 + NO + NO + e^-$	$k_{131} = 2.00 \times 10^{-14}$	35
$O_2^* + O^-$	→	$O_3 + e^-$	$k_{132} = 2.10 \times 10^{-09}$	62
$N_2 + O^-$	→	$N_2 + O + e^-$	$k_{133} = 1.00 \times 10^{-12}$	55
$N + NO_2^-$	→	$NO + NO + e^-$	$k_{177} = 1.00 \times 10^{-11}$	55
$N + NO_3^-$	→	$NO + NO_2 + e^-$	$k_{178} = 1.00 \times 10^{-11}$	55
$O + N_2O_2^-$	→	$NO_2 + NO^-$	$k_{179} = 5.00 \times 10^{-12}$	64
$O + N_2O_2^-$	→	$N_2O + O_2^-$	$k_{180} = 5.00 \times 10^{-12}$	64
$O_3 + N_2O_2^-$	→	$NO_2 + NO_3^-$	$k_{181} = 5.00 \times 10^{-12}$	64
$O_3 + N_2O_2^-$	→	$NO_3 + NO_2^-$	$k_{182} = 5.00 \times 10^{-12}$	64
$N + N_2O_2^-$	→	$N_2O + NO + e^-$	$k_{183} = 5.00 \times 10^{-12}$	64
$N + N_2O_2^-$	→	$N_2 + NO_2 + e^-$	$k_{184} = 5.00 \times 10^{-12}$	64
$O + N_2O_3^-$	→	$NO_2 + NO_2^-$	$k_{185} = 3.00 \times 10^{-12}$	64
$O + N_2O_3^-$	→	$NO + NO_3^-$	$k_{186} = 3.00 \times 10^{-12}$	64
$O + N_2O_3^-$	→	$N_2O + O_3^-$	$k_{187} = 3.00 \times 10^{-12}$	64

Table 4.3.1: Continue

Chemical Reaction	Rate Constant	Ref.
$O_3 + N_2O_3^- \rightarrow NO_3 + NO_3^-$	$k_{188} = 1.00 \times 10^{-11}$	64
$N + N_2O_3^- \rightarrow N_2O + NO_2 + e^-$	$k_{189} = 1.00 \times 10^{-12}$	64
$O + N_2O_4 \rightarrow NO_2 + NO_3$	$k_{190} = 3.00 \times 10^{-16}$	35
$N_2O_4 + M \rightarrow NO_2 + NO_2 + M$	$k_{191} = 3.00 \times 10^{-21}$	35
$N_2O_4 + O_2^+ \rightarrow NO_2 + NO_2^+ + O_2$	$k_{192} = 5.00 \times 10^{-10}$	35
$N_2O_4 + NO_2^- \rightarrow NO + NO_2 + NO_3^-$	$k_{193} = 7.00 \times 10^{-10}$	64
$N_4O_2^+ + Y^- \rightarrow m(O_2 + N_2)$	$k_{194} = 1.00 \times 10^{-06}$	*
$N_3O^+ + Y^- \rightarrow m(O_2 + N_2)$	$k_{195} = 1.00 \times 10^{-06}$	*
$N_2O_4^+ + Y^- \rightarrow m(O_2 + N_2)$	$k_{196} = 1.00 \times 10^{-06}$	*
$N_2O^+ + Y^- \rightarrow m(O_2 + N_2)$	$k_{197} = 1.00 \times 10^{-06}$	*
$NO_4^+ + Y^- \rightarrow m(O_2 + N_2)$	$k_{198} = 1.00 \times 10^{-06}$	*
$NO_3^+ + Y^- \rightarrow m(O_2 + N_2)$	$k_{199} = 1.00 \times 10^{-06}$	*

* Guessed from theories in reference 25

Table 4.3.2: Electron-particles reactions with reaction rates

Chemical Reaction	Rate Constant[1]	Ref.
$e^- + NO_2 + NO_2 \rightarrow NO_2 + NO_2^-$	$k_{134} = 1.10 \times 10^{-27}$	54
$e^- + NO + NO_2 \rightarrow NO + NO_2^-$	$k_{135} = 1.10 \times 10^{-27}$	54
$e^- + O_2 + NO \rightarrow NO + O_2^-$	$k_{136} = 1.00 \times 10^{-31}$	54
$e^- + NO_2 \rightarrow h\nu + NO_2^-$	$k_{137} = 4.00 \times 10^{-10}$	54
$e^- + NO_2 + N_2 \rightarrow NO_2^- + N_2$	$k_{138} = 8.00 \times 10^{-28}$	54
$e^- + O_2 + NO_2 \rightarrow O_2 + NO_2^-$	$k_{139} = 3.00 \times 10^{-28}$	54
$e^- + O_2 + O_2 \rightarrow O_2^- + O_2$	$k_{140} = 3.13 \times 10^{-29} (300/T) \times \exp(-721.1/T)$	58
$e^- + O_3 \rightarrow O_2 + O^-$	$k_{141} = 1.412 \times 10^{-06} (300/T)^{1.5} \times \exp(-18451/T)$	58
$e^- + N_2 \rightarrow e^- + N + N$	$k_{142} = 2.75 \times 10^{-13} (1.3\times10^{-5}\,T + 1) \sqrt{T} \exp(-1.54\times10^{5}/T)$	26
$e^- + O_2 \rightarrow e^- + O + O$	$k_{143} = 10^{f} + 10^{g} + 10^{h}$, $f = -7.90 - 33.0\times10^{4}/\lvert E\rvert$; $g = -8.0 - 4.16\times10^{4}/\lvert E\rvert$; $h = -8.8 - 2.93\times10^{4}/\lvert E\rvert$	37
$e^- + NO + M \rightarrow NO^- + M$	$k_{144} = 2.0 \times 10^{-19} (300/T)^{3/2} \times \exp(-970/T)$	54
$e^- + O + M \rightarrow O^- + M$	$k_{145} = 3.13 \times 10^{-30} (300/T) \times \exp(-721/T)$	58
$e^- + O^- \rightarrow e^- + e^- + O$	$k_{146} = 10^{f}$; $f = 2239 - 2276 \log T + 835.7 (\log T)^2 - 140.8 (\log T)^3 + 8.63 (\log T)^4$	58
$e^- + O_2 \rightarrow O + O^-$	$k_{147} = 10^{f}$; $f = -10.51 - 1.721 \times (4.602 - \log T)^2 - 15.84 (4.6 - \log T)^4$	59
$e^- + O_2 + N_2 \rightarrow N_2 + O_2^-$	$k_{148} = 1.11 \times 10^{-30} (300/T) \times \exp(-721.2/T)$	*
$e^- + N^+ \rightarrow h\nu + N$	$k_{149} = 1.00 \times 10^{-12} (300/T)^{0.70}$	*
$e^- + N_2^+ \rightarrow N + N^*$	$k_{150} = 2.03 \times 10^{-07} (T)^{-0.39}$	63
$e^- + N_3^+ \rightarrow N_2 + N^*$	$k_{151} = 3.00 \times 10^{-07} (300/T)^{0.40}$	*
$e^- + NO^+ \rightarrow N + O$	$k_{152} = 2.20 \times 10^{-07} (300/T)^{0.85}$	*
$e^- + NO_2^+ \rightarrow N^* + O_2$	$k_{153} = 4.00 \times 10^{-07} (300/T)^{0.85}$	*
$e^- + NO_2^+ \rightarrow NO + O^*$	$k_{154} = 4.00 \times 10^{-07} (300/T)^{0.85}$	*

---

[1] In these reaction rates, T represents the electron temperature and is in the unit of Kelvin except for k_{172} to k_{175} where the temperature is in the unit of eV. E is the electric field and is in the unit of V/cm

Table 4.3.2: Continue

Chemical Reaction	Rate Constant	Ref.
$e^- + N_2O^+ \rightarrow NO + N^{\bullet}$	$k_{155} = 2.10 \times 10^{-07} (300/T)^{0.85}$	*
$e^- + N_2O^+ \rightarrow N_2 + O^{\bullet}$	$k_{156} = 2.10 \times 10^{-07} (300/T)^{0.85}$	*
$e^- + O^+ \rightarrow h\nu + O$	$k_{157} = 1.00 \times 10^{-12} (300/T)^{0.70}$	*
$e^- + O_2^+ \rightarrow O + O^{\bullet}$	$k_{158} = 3.00 \times 10^{-07} (300/T)^{0.60}$	*
$e^- + N_4O_2^+ \rightarrow N_2O + N_2O^{\bullet}$	$k_{159} = 7.00 \times 10^{-07} (300/T)^{0.85}$	*
$e^- + N_4O_2^+ \rightarrow N_2 + N_2 + O_2$	$k_{160} = 7.00 \times 10^{-07} (300/T)^{0.85}$	*
$e^- + N_3O^+ \rightarrow N_2 + NO^{\bullet}$	$k_{161} = 3.70 \times 10^{-07} (300/T)^{0.85}$	*
$e^- + N_2O_4^+ \rightarrow NO_2 + NO_2^{\bullet}$	$k_{162} = 7.00 \times 10^{-07} (300/T)^{0.85}$	*
$e^- + N_2O_4^+ \rightarrow N_2 + O_2 + O_2$	$k_{163} = 7.00 \times 10^{-07} (300/T)^{0.85}$	*
$e^- + NO_4^+ \rightarrow NO_2 + O_2$	$k_{164} = 6.00 \times 10^{-07} (300/T)^{0.85}$	*
$e^- + NO_3^+ \rightarrow NO + O_2$	$k_{165} = 5.00 \times 10^{-07} (300/T)^{0.85}$	*
$e^- + O_6^+ \rightarrow O_3 + O_3$	$k_{166} = 1.00 \times 10^{-06}$	*
$e^- + O_4^+ \rightarrow O_2 + O_2^{\bullet}$	$k_{167} = 6.00 \times 10^{-04} / T$	63
$e^- + N_4^+ \rightarrow N_2 + N_2^{\bullet}$	$k_{168} = 6.00 \times 10^{-04} / T$	63
$e^- + N_2O_3^+ \rightarrow N_2 + O_3$	$k_{169} = 1.00 \times 10^{-06} (300/T)^{0.50}$	*
$e^- + N_2O_3^+ \rightarrow NO + NO_2$	$k_{170} = 1.00 \times 10^{-06} (300/T)^{0.50}$	*
$e^- + N_2O_2^+ \rightarrow N_2 + O_2$	$k_{171} = 2.10 \times 10^{-07} (300/T)^{0.85}$	*
$e^- + N_2 \rightarrow N + N^+ + 2e^-$	$k_{172} = 6.39 \times 10^{-11} \sqrt{T}\ (1 + 2.53\times10^{-5} T) \exp(-79171/T)$	26
$e^- + N_2 \rightarrow N_2^+ + 2e^-$	$k_{173} = 1.88 \times 10^{-11} \sqrt{T}\ (1 + 5.13\times10^{-6} T) \exp(-390052/T)$	26
$e^- + O_2 \rightarrow O_2^+ + 2e^-$	$k_{174} = 2.14 \times 10^{-11} \sqrt{T}\ (1 + 6.15 \times10^{-6} T) \exp(-325043/T)$	26
$e^- + O_2 \rightarrow O + O^+ + 2e^-$	$k_{175} = 1.83 \times 10^{-11} \sqrt{T}\ (1 + 8.84\times10^{-6} T) \exp(-226370/T)$	26
$e^- + O_3 + M \rightarrow O_3^- + M$	$k_{176} = 3.13 \times 10^{-29} (300/T) \times \exp(-721/T)$	58

* Guessed from theories in reference 25

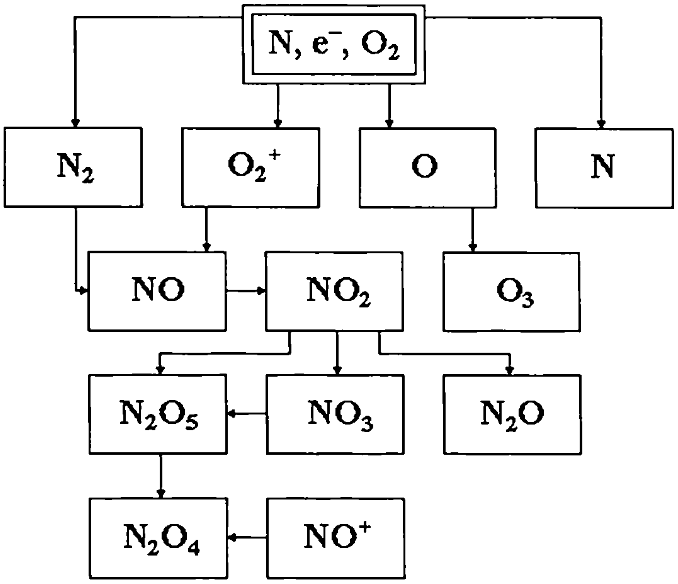

Figure 4.3.1: Block diagram of neutral radical chemistry

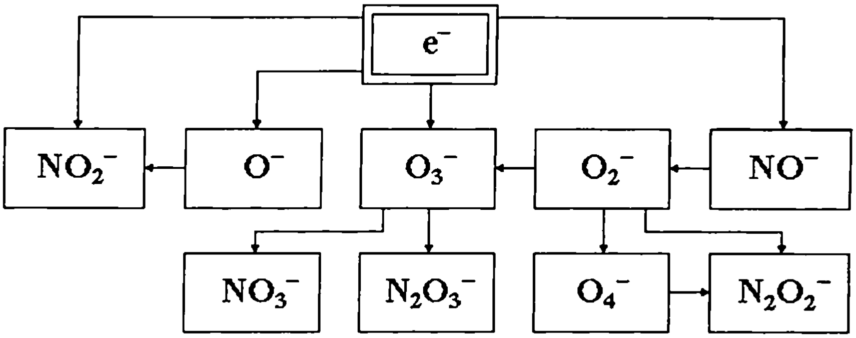

Figure 4.3.2: Block diagram of negative ion chemistry

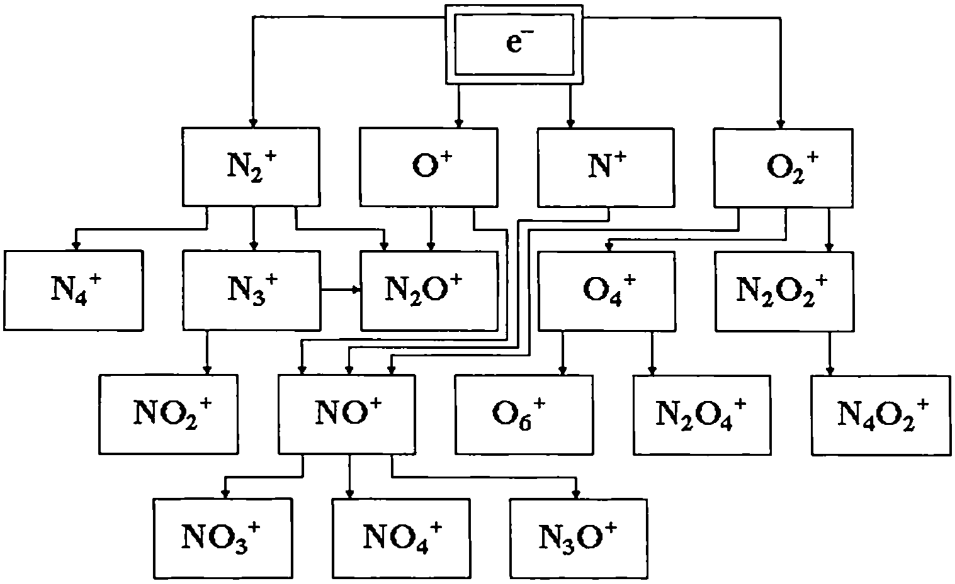

Figure 4.3.3: Block diagram of positive ion chemistry

4.4. Transport Coefficients (Mobility and Diffusion)

The ion mobility (μ_k) and the diffusion coefficient (D_k) of the ions and the neutral radicals for the 36 trace chemical species found in the corona reactor are utilized in Equation 4.2.4 and 4.2.5. Therefore, their values will need to be determined. Ion mobility can be define as the preferred directional movement of the charged particles due to the existence of an external electric field, while diffusion can be define as the movement of particle from an area of high concentration to an area of lower concentration due to the concentration gradient [65].

Since the diffusion coefficient of many ions and neutral radicals (as well as the ion mobility) in air is not well known, a systemic way of estimating their values are required. Statistical mechanics states that the diffusion coefficient of a particle is inversely proportional to the particle's mass [66]:

$$D_k \propto \left(\frac{1}{m_k}\right)^{1/2} \qquad (4.4.1)$$

Therefore, the diffusion coefficient of two different type of particles can be related by:

$$\frac{D_{k_1}}{D_{k_2}} \approx \left(\frac{m_{k_2}}{m_{k_1}}\right)^{1/2} \qquad (4.4.2)$$

This approximation is valid if the mean free path of the two particles is about the same.

From Equation 4.4.2, one can approximate the diffusion coefficient of the ions and neutral particles provided that a reference coefficient is known. For the neutral particles, the diffusion coefficient of the molecular oxygen is used as the reference (D_{O_2} = 0.178 cm^2/s). The diffusion coefficient of O_2 is utilized as the reference value for the negative ions$^-$ ($D_{O_2^-}$ = 0.045 cm^2/s), and the diffusion coefficient of O_2^+ is used as the reference value for the positive ions ($D_{O_2^+}$ = 0.069 cm^2/s).

The mobility and the diffusion coefficient of an ion can be related using the Einstein relation [65], and the diffusion coefficient of the ions can be computed as:

$$D_k = \frac{k_b T}{e} \mu_k \tag{4.4.3}$$

here k_b is the Boltzmann constant, T is the temperature of the ions and e is the charge of an electron. With Equation 4.4.3, the ion mobility can be approximated with a relationship similar to the one shown in Equation 4.4.2, provided that the temperature and the mean free path of the two ions are similar:

$$\frac{\mu_{k_1}}{\mu_{k_2}} \approx \left(\frac{m_{k_2}}{m_{k_1}} \right)^{1/2} \tag{4.4.4}$$

In the present model, the mobility of the O_2^- is taken as the reference mobility for the negative ions ($\mu_{O_2^-} = 2.0$ cm^2/Vs), while the mobility of the O_2^+ is utilized as the reference mobility for the positive ions ($\mu_{O_2^+} = 1.0$ cm^2/Vs). The values of both the diffusion coefficient and the ion mobility utilized by the present model are listed in Table 9.2.1 in Appendix II.

4.5. Strategy for Numerical Simulation

For the present model, a simple substitution method is used to solve for the system of coupled nonlinear equations listed in Table 4.5.1. In order to utilize this substitution method, the non-linear equations will need to be rearrange. In Table 4.5.1, the coupled nonlinear equation is listed as follow:

$$\sum_{i=1}^{36} A_i [x]_i = 0 \qquad (4.5.1)$$

where A_i are the sum of all other variables in the term(s) containing the concentration of x_i but not the concentration of x_i itself, which includes all other concentrations not equals to species *i*. To compute the concentration of one of the species, one can first assumed that all other variables beside the concentration of the species is known. With this assumption, the concentration of species *k* can be computed as:

$$[x]_k = \frac{-\sum_{i \neq k} A_i [x]_i}{A_k} \qquad (4.5.2)$$

With Equation 4.5.2, the concentration of specie *k* can be easily calculated.

The problem here is that the concentrations of the 36 trace species are not readily available since they are what one try to determine. To overcome this problem, initial guesses for all 36 trace species are inputted into the program. These initial guesses are then used to calculate the concentrations of species *k*.

Once all 36 trace species concentrations are computed. They are compared with the concentrations calculated in the last iteration (or the initial guesses for the first iteration). If the difference between the two concentrations (current and previous) for any one of the 36 trace species concentrations is greater than 0.5%, iteration for this system of equations at the current radial position will continue. Otherwise, the solution for this radial position is assume to be converged and the result will be outputted.

When solving for a system of nonlinear equations, possibility exists that solution(s) for some of the concentrations will be negative, which is physically impossible. Consequently, a systematic way of eliminating the negative concentration(s) from the solution is needed. Currently, a minimum cutoff value of 1.0 cm^{-3} is utilized in the model. Once the concentration of any species is below this cutoff value, the concentration at this radial position and any radial position greater than this radial position will be set to 1×10^{-6} cm^{-3}, which should very small when compared to the concentrations of other species and will be assume to be equal to zero. This small value of 1×10^{-6} cm^{-3} is used instead of zero is because division occurs during the concentration calculations (Equation 4.5.2), and a concentration of zero may lead to a division by zero error during the execution of the numerical simulation.

In this way, one should be able to compute the concentrations of the 36 species of neutral particles and ions at any given radial position in the corona reactor. However, the substitution method requires the user to input an initial guess of concentrations as a starting point. Consequently, the numerical simulation will start from the radial position closest to the coaxial wire and work its way towards the grounded electrode. An initial guess for all the concentrations at the first radial position is supplied to the model (1.0×10^{14} cm^{-3} for the 20 kV simulation and 1×10^{12} cm^{-3} for all other simulations). Once the steady-state concentrations for the current radial position are computed, they will be utilized as the initial guesses for the next radial position. This strategy should be sufficient to determine all the steady-state concentrations for all the species in all radial positions, provided that the initial concentration guesses are not too far away from the solutions. Otherwise it may be difficult for the substitution method to locate. A flow diagram of the computational program is shown in Figure 4.5.1. Finally, it took on average about 15 minutes for the program to complete one current-voltage simulation on a 33 MHz 486 personal computer.

Table 4.5.1: A table of the radicals, negative and positive ions transport equations

	Balance for	The Transport Equation
1	NO^-	$k_{26}[O^-][N_2O] + k_{144}[NO][e^-][M] - k_3[NO^-][N_2O] - k_4[NO^-][NO] - k_6[NO^-][NO_2] - k_{32}[O_2][NO^-] - k_{69}[NO^-][X^+] + k_{179}[O][N_2O_2^-] + \mu_{NO^-}\nabla\cdot\left(n_{NO^-}\vec{E}\right) + D_{NO^-}\nabla^2 n_{NO^-} = 0$
2	NO_2^-	$k_6[NO^-][NO_2] + k_{12}[NO_3^-][NO] + k_{18}[NO_3^-][O] + k_{28}[O^-][NO_2] + k_{39}[O_2^-][N_2O] + k_{41}[O_2^-][NO_2] + k_{51}[NO_3^-][O_3] + k_{62}[O_3^-][NO] + k_{137}[NO_2][e^-] - k_7[NO_2^-][N_2O] - k_8[NO_2^-][N_2O_5] - k_9[NO_2^-][NO_2] - k_{50}[NO_2^-][O_3] - k_{70}[NO_2^-][NO^+] + \{k_{138}[N_2] + k_{139}[O_2] + k_{134}[NO_2] + k_{135}[NO]\}[NO_2][e^-] - k_{177}[N][NO_2^-] + k_{182}[N_2O_2^-][O_3] + k_{185}[O][N_2O_3^-] - k_{193}[NO_2^-][N_2O_4] + \mu_{NO_2^-}\nabla\cdot\left(n_{NO_2^-}\vec{E}\right) + D_{NO_2^-}\nabla^2 n_{NO_2^-} = 0$
3	NO_3^-	$k_7[NO_2^-][N_2O] + k_8[NO_2^-][N_2O_5] + k_9[NO_2^-][NO_2] - k_{12}[NO_3^-][NO] - \{k_{18} + k_{19} + k_{20} + k_{21}\}[NO_3^-][O] + k_{50}[NO_2^-][O_3] - k_{51}[NO_3^-][O_3] + k_{57}[O_3^-][N_2O] + k_{61}[O_3^-][NO] + k_{63}[O_3^-][NO_2] + k_{67}[O_4^-][NO] - k_{71}[NO_3^-][NO^+] - k_{178}[NO_3^-][N] + k_{181}[N_2O_2^-][O_3] + k_{186}[O][N_2O_3^-] + k_{188}[O_3][N_2O_3^-] + k_{193}[NO_2^-][N_2O_4] + \mu_{NO_3^-}\nabla\cdot\left(n_{NO_3^-}\vec{E}\right) + D_{NO_3^-}\nabla^2 n_{NO_3^-} = 0$
4	O_2^-	$k_{19}[NO_3^-][O] + k_{32}[NO^-][O_2] - k_{36}[O_2^-][N] - k_{37}[O_2^-][N_2] - k_{38}[O_2^-][N_2][M] - \{k_{39} + k_{40}\}[O_2^-][N_2O] - k_{41}[O_2^-][NO_2] - \{k_{42} + k_{43}\}[O_2^-][O] - k_{44}[O_2^-][O_2] - k_{45}[O_2^-][O_2][M] - k_{54}[O_2^-][O_3] + k_{58}[O_3^-][N_2O] + k_{64}[O_3^-][O] + \{k_{140}[O_2] + k_{148}[N_2]\}[e^-][O_2] - \{k_{72}[O_4^+] + k_{73}[N_2^+] + k_{74}[O_2^+]\}[O_2^-] + k_{136}[NO][O_2][e^-] + k_{180}[O][N_2O_2^-] + \mu_{O_2^-}\nabla\cdot\left(n_{O_2^-}\vec{E}\right) + D_{O_2^-}\nabla^2 n_{O_2^-} = 0$
5	O_3^-	$k_{20}[NO_3^-][O] + k_{35}[O_2][O_2][O^-] + k_{40}[O_2^-][N_2O] + k_{53}[O^-][O_3] + k_{54}[O_2^-][O_3] - k_{55}[O_3^-][M] - k_{56}[O_3^-][N_2][N_2] - k_{57}[O_3^-][N_2O] - k_{58}[O_3^-][N_2O] - k_{59}[O_3^-][N_2O] - k_{60}[O_3^-][N_2O] - k_{61}[O_3^-][NO] - k_{62}[O_3^-][NO] - k_{63}[O_3^-][NO_2] - k_{64}[O_3^-][O] + k_{68}[O_4^-][O] + k_{176}[O_3][e^-][M] - k_{75}[O_3^-][X^+] - k_{131}[O_3^-][N_2O] + k_{187}[N_2O_3^-][O] + \mu_{O_3^-}\nabla\cdot\left(n_{O_3^-}\vec{E}\right) + D_{O_3^-}\nabla^2 n_{O_3^-} = 0$

Table 4.5.1: Continue

	Balance for	The Transport Equation
6	O^-	$k_{42}[O_2^-][O] - k_{23}[O^-][N] - k_{24}[O^-][N_2] - k_{25}[O^-][N_2][M] - k_{26}[O^-][N_2O] - k_{27}[O^-][NO] - k_{28}[O^-][NO_2] - k_{29}[O^-][O] - k_{34}[O^-][O_2] - k_{35}[O^-][O_2][O_2] - k_{53}[O^-][O_3] + k_{145}[O][e^-][M] - k_{146}[e^-][O^-] + k_{147}[e^-][O_2] + k_{141}[e^-][O_3] - \{k_{76}[O^+] + k_{77}[N^+] + k_{132}[O_2] + k_{133}[N_2]\}[O^-] + \mu_{O^-}\nabla\cdot\left(n_{O^-}\vec{E}\right) + D_{O^-}\nabla^2 n_{O^-} = 0$
7	$N_2O_2^-$	$k_{38}[O_2^-][N_2][M] + k_{65}[O_4^-][N_2] - k_{78}[N_2O_2^-][X^+] - \{k_{179} + k_{180}\}[O][N_2O_2^-] - \{k_{181}+k_{182}\}[N_2O_2^-][O_3] - \{k_{183}+k_{184}\}[N_2O_2^-][N] + \mu_{N_2O_2^-}\nabla\cdot\left(n_{N_2O_2^-}\vec{E}\right) + D_{N_2O_2^-}\nabla^2 n_{N_2O_2^-} = 0$
8	O_4^-	$k_{45}[O_2^-][O_2][M] + k_{59}[O_3^-][N_2O] - \{k_{65}[N_2] + k_{66}[N_2O] + k_{67}[NO] + k_{68}[O] + k_{79}[X^+]\}[O_4^-] + \mu_{O_4^-}\nabla\cdot\left(n_{O_4^-}\vec{E}\right) + D_{O_4^-}\nabla^2 n_{O_4^-} = 0$
9	$N_2O_3^-$	$k_{56}[O_3^-][N_2][N_2] + k_{66}[O_4^-][N_2O] - k_{80}[N_2O_3^-][X^+] - \{k_{185} + k_{186} + k_{187}\}[O][N_2O_3^-] - k_{188}[O_3][N_2O_3^-] - k_{189}[N][N_2O_3^-] + \mu_{N_2O_3^-}\nabla\cdot\left(n_{N_2O_3^-}\vec{E}\right) + D_{N_2O_3^-}\nabla^2 n_{N_2O_3^-} = 0$
10	N_2O_5	$k_{11}[NO_3][NO_2][M] - \{k_1[M] + k_8[NO_2^-] + k_{13}[O] + k_{81}[NO^+] + k_{82}[O_2^+] + k_{110}[NO_2^+]\}[N_2O_5] + D_{N_2O_5}\nabla^2 n_{N_2O_5} = 0$
11	NO_3	$k_1[N_2O_5][M] - k_{10}[NO_3][NO] - k_{11}[NO_3][NO_2][M] + k_{16}[NO_2][O][M] - k_{17}[NO_3][O] + k_{49}[NO_2][O_3] + k_{82}[N_2O_5][O_2^+] - 2\times k_{126}[NO_3][NO_3] + k_{182}[N_2O_2^-][O_3] + k_{188}[O_3][N_2O_3^-] + k_{190}[O][N_2O_4] + D_{NO_3}\nabla^2 n_{NO_3} = 0$
12	NO_2	$k_1[N_2O_5][M] - k_5[NO_2][N] - k_6[NO^-][NO_2] + 2\times k_8[NO_2^-][N_2O_5] - k_9[NO_2^-][NO_2] + 2\times k_{10}[NO_3][NO] - k_{11}[NO_3][NO_2][M] + k_{12}[NO_3^-][NO] + 2\times k_{13}[N_2O_5][O] + k_{14}[NO][O][M] - k_{15}[NO_2][O] - k_{16}[NO_2][O][M] + k_{17}[NO_3][O] + k_{19}[NO_3^-][O] + k_{21}[NO_3^-][O] + k_{27}[O^-][NO] - k_{28}[O^-][NO_2] + 2\times k_{31}[NO][NO][O_2] + k_{36}[O_2^-][N] - k_{41}[O_2^-][NO_2] + k_{48}[NO][O_3] - k_{49}[NO_2][O_3] - k_{63}[O_3^-][NO_2] - k_{137}[NO_2][e^-] - k_{138}[NO_2][N_2][e^-] - k_{139}[NO_2][O_2][e^-] + k_{83}[NO][NO_2^+] - k_{84}[NO_2][O^+] + 2\times k_{162}[N_2O_4^+][e^-] + k_{164}[NO_4^+][e^-] + k_{170}[N_2O_3^+][e^-] - \{k_{127}+k_{128}+k_{129}+k_{130}\}[NO_2][N] - \{k_{134}[NO_2] + k_{135}[NO]\}[NO_2][e^-] + k_{178}[NO_3^-][N] + \{k_{179}[O] + k_{181}[O_3] + k_{184}[N]\}[N_2O_2^-] + \{k_{185}[O] + k_{189}[N]\}[N_2O_3^-] + \{k_{190}[O] + 2\times k_{191}[M] + k_{192}[O_2^+] + k_{193}[NO_2^-]\}[N_2O_4] + D_{NO_2}\nabla^2 n_{NO_2} = 0$

Table 4.5.1: Continue

	Balance for	The Transport Equation
16	N_2O	$k_5 [NO_2][N] - k_7 [NO_2^-][N_2O] + k_{24} [O^-][N_2] - k_{26} [O^-][N_2O] - k_{39} [O_2^-][N_2O] - k_{40} [O_2^-][N_2O] - \{k_{57} + k_{58} + k_{59} + k_{60}\}[O_3^-][N_2O] - k_{66} [O_4^-][N_2O] + k_{101} [N_2O_3^+][O_2] + k_{102} [N_3^+][O_2] - k_{98} [N_2O][O^+] - k_{103} [N_2O] [N_2^+] - k_{119} [N_2O][O_4^+] - k_{121} [N_2O][O_2^+][M] + 2\times k_{159} [N_4O_2^+][e^-] + k_{126} [NO_3][NO_3] + k_{128} [NO_2][N] - k_{131} [O_3^-] [N_2O] + k_{180} [O][N_2O_2^-] + k_{183} [N_2O_2^-][N] + k_{187} [O][N_2O_3^-] + k_{189} [N][N_2O_3^-] + D_{N_2O}\nabla^2 n_{N_2O} = 0$
17	O_3	$k_{33} [O][O_2][M] + k_{34} [O^-][O_2] + k_{43} [O_2^-][O] - k_{46} [O_3][M] - k_{47} [N][O_3] - k_{48} [NO][O_3] - k_{49} [NO_2][O_3] - k_{50} [NO_2^-][O_3] - k_{51} [NO_3^-][O_3] - k_{52} [O][O_3] - k_{53} [O^-][O_3] - k_{54} [O_2^-][O_3] + k_{55} [O_3^-] [M] - k_{141} [O_3][e^-] - k_{176} [O_3][e^-][M] - k_{104} [O_3][NO^+] - k_{108} [O_3][NO^+][M] + 2\times k_{166} [O_6^+][e^-] + k_{169} [N_2O_3^+][e^-] + k_{126} [NO_3][NO_3] + k_{132} [O^-][O_2] - \{k_{181}+k_{182}\} [N_2O_2^-][O_3] - k_{188} [O_3] [N_2O_3^-] + D_{O_3}\nabla^2 n_{O_3} = 0$
18	O^+	$k_{85} [N^+][O_2] + k_{99} [O][N_2^+] - \{k_{95} [N_2] + k_{90} [NO] + k_{84} [NO_2] + k_{98} [N_2O]\}[O^+] - k_{76} [O^-][O^+] - k_{157} [O^+][e^-] + k_{175} [O_2][e^-] - \mu_{O^+} \nabla\cdot\left(n_{O^+} \bar{E}\right) + D_{O^+} \nabla^2 n_{O^+} = 0$
19	N_2O_4	$k_{71} [NO_3^-][NO^+] + k_{81} [N_2O_5][NO^+] + k_{110} [N_2O_5][NO_2^+] - k_{190} [O][N_2O_4] - k_{191} [M][N_2O_4] - k_{192} [O_2^+][N_2O_4] - k_{193} [NO_2^-] [N_2O_4] + D_{N_2O_4}\nabla^2 n_{N_2O_4} = 0$
20	$N_4O_2^+$	$k_{105} [N_2O_2^+][N_2][M] - \{k_{159} + k_{160}\} [N_4O_2^+][e^-] - k_{194} [N_4O_2^+] [Y^-] - \mu_{N_4O_2^+} \nabla\cdot\left(n_{N_4O_2^-} \vec{E}\right) + D_{N_4O_2^+}\nabla^2 n_{N_4O_2^+} = 0$
21	N_3O^+	$k_{106} [NO^+][N_2][N_2] - k_{161} [N_3O^+][e^-] - k_{195} [N_3O^+][Y^-] - \mu_{N_3O^+} \nabla\cdot\left(n_{N_3O^+} \vec{E}\right) + D_{N_3O^+} \nabla^2 n_{N_3O^+} = 0$
22	$N_2O_4^+$	$k_{107} [O_4^+][N_2][M] - \{k_{162} + k_{163}\}[N_2O_4^+][e^-] - k_{196} [N_2O_4^+][Y^-] - \mu_{N_2O_4^+} \nabla\cdot\left(n_{N_2O_4^+} \vec{E}\right) + D_{N_2O_4^+}\nabla^2 n_{N_2O_4^+} = 0$
23	N_2O^+	$k_{103} [N_2O][N_2^+] + k_{92} [NO][N_3^+] + k_{98} [N_2O][O^+] - \{k_{155} + k_{156}\} [N_2O^+][e^-] - k_{197} [N_2O^+][Y^-] - \mu_{N_2O^+} \nabla\cdot\left(n_{N_2O^+} \vec{E}\right) + D_{N_2O^+} \nabla^2 n_{N_2O^+} = 0$

Table 4.5.1: Continue

	Balance for	The Transport Equation
24	NO_4^+	$k_{108}[O_3][NO^+][M] - k_{164}[NO_4^+][e^-] - k_{198}[NO_4^+][Y^-] - \mu_{NO_4^+}\nabla\cdot\left(n_{NO_4^+}\vec{E}\right) + D_{NO_4^+}\nabla^2 n_{NO_4^+} = 0$
25	NO_3^+	$k_{109}[NO^+][N_2][O_2] + k_{110}[N_2O_5][NO_2^+] - k_{165}[NO_3^+][e^-] - k_{199}[NO_3^+][Y^-] - \mu_{NO_3^+}\nabla\cdot\left(n_{NO_3^+}\vec{E}\right) + D_{NO_3^+}\nabla^2 n_{NO_3^+} = 0$
26	N_2^+	$k_{173}[N_2][e^-] - k_{111}[N_2^+][N_2][N_2] - k_{103}[N_2O][N_2^+] - k_{112}[O_2][N_2^+] - \{k_{94} + k_{99}\}[O][N_2^+] - k_{89}[NO][N_2^+] - k_{73}[O_2^-][N_2^+] - k_{115}[N_2][N_2^+] - k_{150}[N_2^+][e^-] - \mu_{N_2^+}\nabla\cdot\left(n_{N_2^+}\vec{E}\right) + D_{N_2^+}\nabla^2 n_{N_2^+} = 0$
27	N^+	$k_{172}[N_2][e^-] - \{k_{85} + k_{97} + k_{113}\}[N^+][O_2] - k_{88}[NO][N^+] - k_{114}[N^+][N_2][N_2] - k_{77}[O^-][N^+] - k_{149}[N^+][e^-] - \mu_{N^+}\nabla\cdot\left(n_{N^+}\vec{E}\right) + D_{N^+}\nabla^2 n_{N^+} = 0$
28	NO^+	$k_{83}[NO][NO_2^+] + k_{86}[O_2^+][N_2] + k_{87}[N][NO_2^+] + k_{88}[NO][N^+] + k_{89}[NO][N_2^+] + k_{90}[NO][O^+] + k_{91}[NO][O_2^+] + k_{93}[NO][N_3^+] + k_{94}[O][N_2^+] + k_{95}[O^+][N_2] + k_{96}[N][O_2^+] + k_{97}[N^+][O_2] + k_{100}[O][NO_2^+] + k_{102}[N_3^+][O_2] - k_{70}[NO_2^-][NO^+] - k_{71}[NO_3^-][NO^+] - k_{81}[N_2O_5][NO^+] - k_{104}[O_3][NO^+] - k_{106}[NO^+][N_2][N_2] - k_{108}[O_3][NO^+][M] - k_{109}[NO^+][N_2][O_2] - k_{122}[NO][NO^+][M] - k_{152}[NO^+][e^-] - \mu_{NO^+}\nabla\cdot\left(n_{NO^+}\vec{E}\right) + D_{NO^+}\nabla^2 n_{NO^+} = 0$
29	N_3^+	$k_{114}[N^+][N_2][N_2] + k_{115}[N_2^+][N_2] - \{k_{92} + k_{93}\}[NO][N_3^+] - \{k_{102} + k_{116}\}[N_3^+][O_2] - k_{151}[N_3^+][e^-] - \mu_{N_3^+}\nabla\cdot\left(n_{N_3^+}\vec{E}\right) + D_{N_3^+}\nabla^2 n_{N_3^+} = 0$
30	O_6^+	$k_{117}[O_4^+][O_2][M] - k_{166}[O_6^+][e^-] - \mu_{O_6^+}\nabla\cdot\left(n_{O_6^+}\vec{E}\right) + D_{O_6^+}\nabla^2 n_{O_6^+} = 0$
31	O_4^+	$k_{101}[N_2O_3^+][O_2] + k_{118}[O_2^+][O_2][O_2] + k_{125}[N_2O_2^+][O_2] - k_{72}[O_2^-][O_4^+] - k_{107}[O_4^+][N_2][M] - k_{117}[O_4^+][O_2][M] - k_{119}[N_2O][O_4^+] - k_{167}[O_4^+][e^-] - \mu_{O_4^+}\nabla\cdot\left(n_{O_4^+}\vec{E}\right) + D_{O_4^+}\nabla^2 n_{O_4^+} = 0$
32	N_4^+	$k_{111}[N_2^+][N_2][N_2] - k_{120}[N_4^+][O_2] - k_{168}[N_4^+][e^-] - \mu_{N_4^+}\nabla\cdot\left(n_{N_4^+}\vec{E}\right) + D_{N_4^+}\nabla^2 n_{N_4^+} = 0$

Table 4.5.1: Continue

	Balance for	The Transport Equation
33	$N_2O_3^+$	$k_{119}\,[N_2O][O_4^+] + k_{121}\,[N_2O][O_2^+][M] - k_{101}\,[N_2O_3^+][O_2] - \{k_{169} + k_{170}\}\,[N_2O_3^+][e^-]\ - \mu_{N_2O_3^+}\nabla\cdot\left(n_{N_2O_3^+}\vec{E}\right) + D_{N_2O_3^+}\nabla^2 n_{N_2O_3^+} = 0$
34	$N_2O_2^+$	$k_{122}\,[NO][NO^+][M] + k_{123}\,[O_2^+][N_2][N_2] - k_{105}\,[N_2O_2^+][N_2][M] - k_{124}\,[N_2O_2^+][N_2] - k_{125}\,[N_2O_2^+][O_2] - k_{171}\,[N_2O_2^+][e^-]\ - \mu_{N_2O_2^+}\nabla\cdot\left(n_{N_2O_2^+}\vec{E}\right) + D_{N_2O_2^+}\nabla^2 n_{N_2O_2^+} = 0$
35	NO_2^+	$k_{81}\,[N_2O_5][NO^+] + k_{82}\,[N_2O_5][O_2^+] + k_{84}\,[NO_2][O^+] + k_{104}\,[O_3][NO^+] + k_{116}\,[N_3^+][O_2] - k_{83}\,[NO][NO_2^+] - k_{87}\,[N][NO_2^+] - k_{100}\,[O][NO_2^+] - k_{110}\,[N_2O_5][NO_2^+] - \{k_{153} + k_{154}\}[NO_2^+][e^-] + k_{192}\,[O_2^+][N_2O_4]\ - \mu_{NO_2^+}\nabla\cdot\left(n_{NO_2^+}\vec{E}\right) + D_{NO_2^+}\nabla^2 n_{NO_2^+} = 0$
36	O_2^+	$k_{112}\,[N_2^+][O_2] + k_{113}\,[N^+][O_2] + k_{120}\,[N_4^+][O_2] + k_{124}\,[N_2O_2^+][N_2] + k_{174}\,[O_2][e^-] - k_{74}\,[O_2^-][O_2^+] - k_{82}\,[N_2O_5][O_2^+] - k_{86}\,[O_2^+][N_2] - k_{91}\,[NO][O_2^+] - k_{96}\,[N][O_2^+] - k_{118}\,[O_2^+][O_2][O_2] - k_{121}\,[N_2O][O_2^+][M] - k_{123}\,[O_2^+][N_2]\,[N_2] - k_{158}\,[O_2^+][e^-] - k_{192}\,[O_2^+][N_2O_4]\ - \mu_{O_2^+}\nabla\cdot\left(n_{O_2^+}\vec{E}\right) + D_{O_2^+}\nabla^2 n_{O_2^+} = 0$

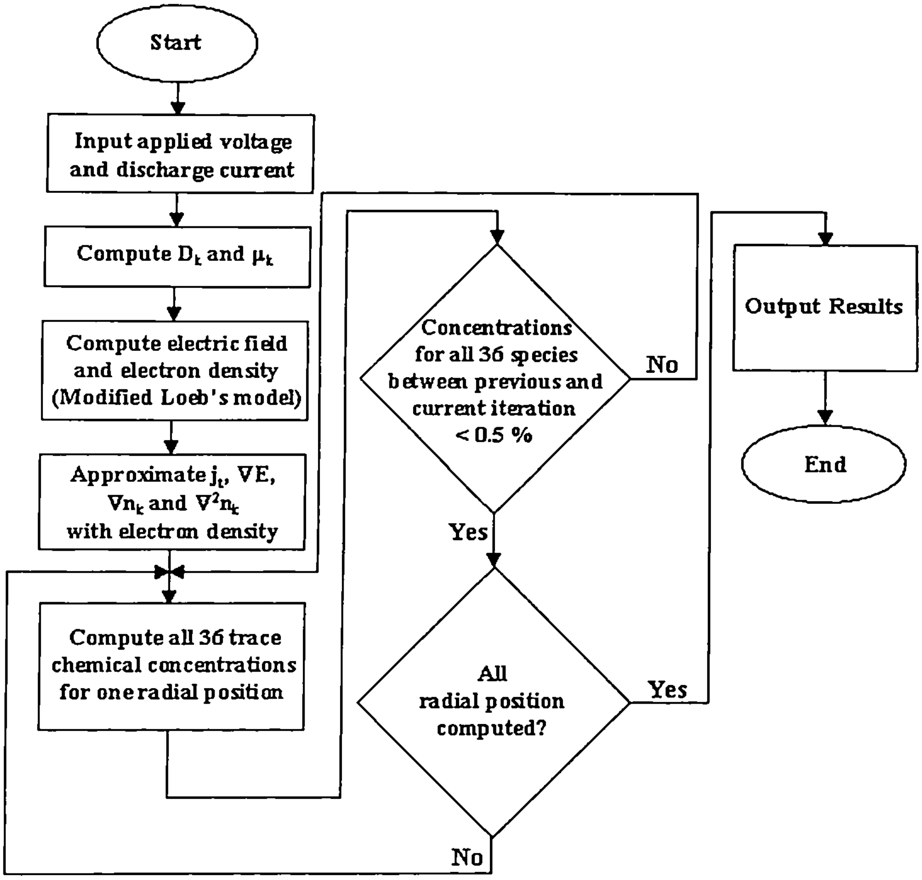

Figure 4.5.1: Flow diagram for the computational program

5. Numerical Simulation Results

This chapter is divided into three sections. The first section examines the effect of the applied voltage on the concentrations of the 36 trace chemical species. The second section investigates the effect of the gas flow rate on the 36 trace chemical concentrations. The last section explores the sensitivity of the simulation program to different conditions like radial step sizes and convergence tolerance.

5.1. Effect of Applied Voltage

To study the effect of the applied voltage on the chemical species concentrations, five different applied voltages without gas flow are simulated. The magnitude of these five voltage are: 9.9 kV, 13.0 kV, 15.0 kV, 17.0 kV and 20.0 kV, with a corresponding time averaged discharge current of 1.0×10^{-4} A, 5.0×10^{-4} A, 9.0×10^{-4} A, 1.5×10^{-3} A and 2.5×10^{-3} A as shown in Figure 3.2.1.

The effect of the applied voltage on the electric field computation (Equation 4.2.22) is shown in Figure 5.1.1. From this figure, one can observed that the magnitude of the electric field is largest near the corona wire, and decreases as the radial distance increases. The magnitude of the electric field also increases with increasing applied voltage. Similar tendencies are observed for the radial electron density profiles and the radial electron temperature profiles as shown in Figures 5.1.2 and 5.1.3 respectively. When comparing these three figures, one can observed the effects of the applied voltage is most significant for the radial electron density profiles, while the radial electron temperature profiles tends to be the least affected.

Since the divergence of the ion density ($\nabla\cdot n_k$) and the Laplacian of the particle density ($\nabla^2 n_k$) are approximated using the radial electron density profiles in this model (Equations 4.2.24 and 4.2.25), they can be determined once the radial electron density profiles are computed. The magnitude of these results are shown in Figures 5.1.4 and 5.1.5. In Figure 5.1.4, the magnitude of the electric field times the divergence of the ion density is plotted instead of just the divergence of the ion density. It is because this multiplication term is used in the charge transport equation (Equation 4.2.4).

From Figure 5.1.4, one can observe that the ion density divergence times the electric field tends to the greatest near the corona wire, and decreases as the radial distance increases. The magnitude of this term also increases with increasing applied voltage. For the Laplacian of the particle density computation, the magnitude of this term is also greatest near the corona wire and decreases as the radial distance increases. However, the applied voltage have very minimal effect on the computation of the Laplacian as one can observe in Figure 5.1.5.

The simulation results for the applied voltage of –9.9 kV is shown in Figures 5.1.6 to 5.1.11. These figures show that the concentrations of the trace neutral species are generally higher than the concentrations of the negative ions, which in term are generally higher than the concentrations of the positive ions. One may also observe that the concentrations for some of the negative ions tends to increase ($N_2O_2^-$) or remain constant (O_2^-, O_4^- and NO^-) as the radial distance increases (Figures 5.1.6 and 5.1.7), while the concentrations for all the radicals (except NO) and positive ions tends to decrease as the radial distance increases (Figures 5.1.8 to 5.1.11). This is consistent with the negative voltage applied to the corona wire, which generates an electric field that drives the negative ions towards the grounded electrode, and attracts the positive ions towards the corona wire. The electric field should have very minimal effect on the neutral radicals since they are not ionized.

From Figures 5.1.6 and 5.1.7, one can observed that $N_2O_2^-$ is the negative ion with the highest concentration near the corona wire and the grounded electrode. Its concentration near the corona wire is about 1×10^{12} cm^{-3} and gradually increases to about 1×10^{14} cm^{-3} near the grounded electrode. The negative ion with the next highest concentration near the corona wire is NO_3^-, which have a concentration of about 4.0×10^{11} cm^{-3} near the corona wire, and decrease to about 1×10^{10} cm^{-3} near the grounded electrode. The negative species with the third highest concentration near the corona wire is NO_2^-, which have a concentration of about 5×10^{10} cm^{-3} near the corona wire, increases to about 3×10^{11} cm^{-3} at $r \approx 0.8$ cm and decrease to about 2×10^{10} cm^{-3} near the grounded electrode. The species with the next highest concentration near the corona wire are $N_2O_3^-$ and O_2^-, which have a concentrations of just about 1×10^{10} cm^{-3} near the corona wire. However, the concentration of O_2^- tends to remain constant for all the radial positions, while the concentration of $N_2O_3^-$ tends to decrease as the radial distance increases (decreased to about 1×10^{8} cm^{-3} near the grounded electrode).

For the neutral radicals, the species with the highest concentration is N_2O, which have a concentration of above 1×10^{16} cm^{-3} near the corona wire and gradually decrease to about 1×10^{14} cm^{-3} near the grounded electrode. Ozone have the second highest concentration near the corona wire (about 2×10^{16} cm^{-3}) but decrease dramatically as the radial distance increases (to about 8×10^{9} cm^{-3} near the grounded electrode). The radicals with the second highest concentration near the grounded electrode are both NO and NO_2, which have a concentration of about 1×10^{12} cm^{-3} near the grounded electrode. However the concentration of the NO_2 tends to decrease as the radial distance increases towards the grounded electrode (NO_2 concentration near the corona wire is about 1×10^{15} cm^{-3}), while the concentration of NO tends to remain constant as the radial distance increases (NO concentration near the corona wire is about 2×10^{12} cm^{-3}).

For the positive ions, the species with the highest concentration near the corona wire is N_3O^+, which have a concentration of above 1×10^{10} cm^{-3} near the corona wire and decrease to below 1×10^{5} cm^{-3} near the grounded electrode (still the highest species concentration near the grounded electrode). The species with the second highest concentration near the corona wire is $N_4O_2^+$ (1×10^{9} cm^{-3}), and its concentration decreases to below 1×10^{4} cm^{-3} near the grounded electrode. The concentration of $N_2O_4^+$ is also very close to the concentrations of N_3O^+ or $N_4O_2^+$. $N_2O_4^+$ have a concentration of about 6×10^{8} cm^{-3} near the corona wire and decrease to about 1×10^{3} cm^{-3} near the grounded electrode.

From Figures 5.1.10 and 5.1.11, one may noticed that O_6^+, NO_2^+, N_2^+, and N_4^+ are not shown in these figures. This is because all of these ions' concentrations are equal to 1×10^{-6} cm^{-3}. From Table 4.5.1, one can observed that all of these positive ions have relatively small production term(s), which may lead to a very small computed concentrations as show in the present results. Similar results are observed for the higher applied voltages, except for N_2^+, and N_4^+ at radial position equals to 0.1469 cm (first computed radial position) which respectively have a concentrations of 1.52×10^1 cm^{-3} and 3.06×10^1 cm^{-3} for the –13.0 kV case, a concentrations of 1.85×10^2 cm^{-3} and 3.73×10^2 cm^{-3} for the –15.0 kV case, a concentrations of 1.47×10^3 cm^{-3} and 2.95×10^3 cm^{-3} for the –17.0 kV case and a concentrations of 1.33×10^4 cm^{-3} and 2.67×10^4 cm^{-3} for the –20.0 kV case.

Similar results are observed for all other applied voltage simulated in the present work, which are shown in Figures 5.1.12 to 5.1.17 for the –13 kV case, in Figures 5.1.18 to 5.1.23 for the –15 kV case, in Figures 5.1.24 to 5.1.29 for the –17 kV case and in Figures 5.1.30 to 5.1.35 for the –20 kV case. However for the higher applied voltage (–17 kV and –20 kV), the positive ions with the highest concentrations are switched from N_3O^+, $N_4O_2^+$ and $N_2O_4^+$ to NO^+ (concentration of above 1×10^9 cm^{-3} near the corona wire and decreases to below 1×10^7 cm^{-3} near the grounded electrode at V = –20.0 kV), N_3^+ (concentration of just below 1×10^9 cm^{-3} near the corona wire and decreases to below 1×10^6 cm^{-3} near the grounded electrode at V = –20.0 kV) and $N_2O_3^+$ (concentration of above 1×10^{10} cm^{-3} near the corona wire and decreases to below 1×10^{6} cm^{-3} near the grounded electrode at V = –20.0 kV).

Finally from Figures 5.1.12 to 5.1.35, one may observed that the concentration of NO_x (sum of NO and NO_2) tends to increase as the applied voltage increases. However, the increase is mainly due to the increases in NO concentration, and the NO_2 concentration tends to decrease very slightly at the radial positions near the grounded electrode as the applied voltage is increased. Also several toxic byproducts like O_3, NO, NO_2 and N_2O_4 are observed in the simulation results. However, their maximum computed concentrations (at V = –20 kV) are less than the acceptable limit of 25 ppm and therefore should not be a safety concern.

From Figures 5.1.12 to 5.1.35, one may also observed that as the applied voltage increases, the concentrations of all the ions and radicals tends to increase as well. To demonstrated this effect more clearly, the total concentration of positive ions, negative ions and neutral radicals are show in Figures 5.1.36, 5.1.37 and 5.1.38 respectively. From these figures, one can observed that as the applied voltage increases, the total concentrations of these three groups also increases. However, the increase is most significant for the negative ions.

In order to calculate the negative ions current density computed by this model for various applied voltages, the total concentration for all the negative ions

(Figure 5.1.37) is multiplied by the magnitude of the electric field and then divided by the radial distance as shown in Figure 5.1.39. Figure 5.1.39 shows that the total negative ion current flux increases with increasing applied voltage, and is relatively constant for all of the radial positions except near the corona wire. This exception may be caused by the fact that the concentrations near the corona wire contains the largest computation error as will be demonstrated in Section 5.3. Therefore, the values near the corona wire may not be accurate.

Since the total concentrations for the negative ions are much greater than the total concentrations for the positive ions, the current densities for the different applied voltages may be estimated from the linear portion of Figure 5.1.39 by assuming the mobility of all the negative ions is approximately equals to the mobility of the $N_2O_2^-$ (and neglecting the concentrations of the positive ions). This assumption should be valid since the concentration of $N_2O_2^-$ dominates the total concentrations of the negative ions at the larger radial positions (near the grounded electrode). The calculated current densities are: 3.7×10^0 mA/cm^3, 3.7×10^1 mA/cm^3, 1.9×10^2 mA/cm^3, 1.5×10^3 mA/cm^3 and 3.7×10^3 mA/cm^3 for the applied voltage of –9.9 kV, –13.0 kV, –15.0 kV, –17.0 kV and –20.0 kV respectively. From these calculations, one can observed that the ion current density increases by about a factor of 1000 as the applied voltage is increased by about a factor of 2.

By comparison with experimental results, the present results agree with Donohoe et al. [2], Ito et al. [3], Masuda et al. [4], Hill et al. [5] and Brahdvold and Martinez [6] which observed significant amounts of N_2O, O_3 and NO_x (NO and NO_2) as well as trace amounts of N_2O_3, N_2O_4 and N_2O_5 from the corona discharge of air. Present model also predicted the existence of O_3^- as has been observed in McDaniel and Crane [31], Lecuiller et al. [32] and Goldman et al.'s [33] experiments.

By comparing the neutral radical densities with the results show in Mukkavilli et at. [28], one may observed the computed ozone and the NO_x (NO and NO_2) concentrations in this work disagree with the results show in Mukkavilli et al.'s work. The ozone concentration computed by Mukkavilli et al.'s tends to be much higher that the NO_x concentration, while the results in this work show that the concentrations of O_3 and NO_x are about the same near the corona wire and the concentration of the NO_x is much higher that the concentration of O_3 near the grounded electrode. Present results also show that N_2O is the radical species with the highest concentration. One possible reason for these discrepancies may be due to the fact that no ion species and very few radical species are considered in Mukkavilli et al.'s model. As a result, Mukkavilli et al's model may not be as accurate as the model presented in this work. Also Mukkavilli et al's model is designed for a pin-plate electrode system with 4890 cm/s of gas flow for streamer corona discharges, while the results presented in this section is intended for a coaxial wire-tube system with zero gas flow for a time averaged corona model. These differences in electrode geometry, type of corona and gas velocity will also affect the results.

From Penetrante's work [1], one can observed that a high concentrations of N_2O, NO_2 and NO_3 are predicted. This observation is similar to the results show in the present work. However, a high concentration of O_3 and N_2O_5 is also predicted in Penetrante's model. This minor difference with the present model may be due to the smaller number of ions, radical species as well as chemical reactions considered in Penetrante's model. Also a gas composition of 80% N_2, 20% O_2 with 400 ppm of NO in a volume averaged streamer corona is simulated in Penetrante's model, while a gas composition of 79% N_2 and 21% O_2 is simulated in the present model with time averaged radial density profiles. Finally Penetrante's work simulates a pulsed corona discharge while the present model simulates a dc corona discharge, and this difference in the type of corona discharge modelled should also affect the numerical results. Nevertheless, Penetrante's simulation results agree qualitatively well with the present results.

Finally if one compare the neutral radicals density with the results by Tochikubo et al. [41], one can observe that Tochikubo et al.'s results predict a relatively high concentration of NO_3. This is similar to the result from the present model. However, Tochikubo et al's model also predict a relatively high concentration of O_3, which is difference from the present result. Again this variation may be attributed to the difference type of corona discharge simulated (Tochikubo's model is intended for pulsed corona discharge), and the oversimplified number of chemical species and reactions considered by Tochikubo et al. (Tochikubo et al.'s model considered only very few radicals species and no ion species).

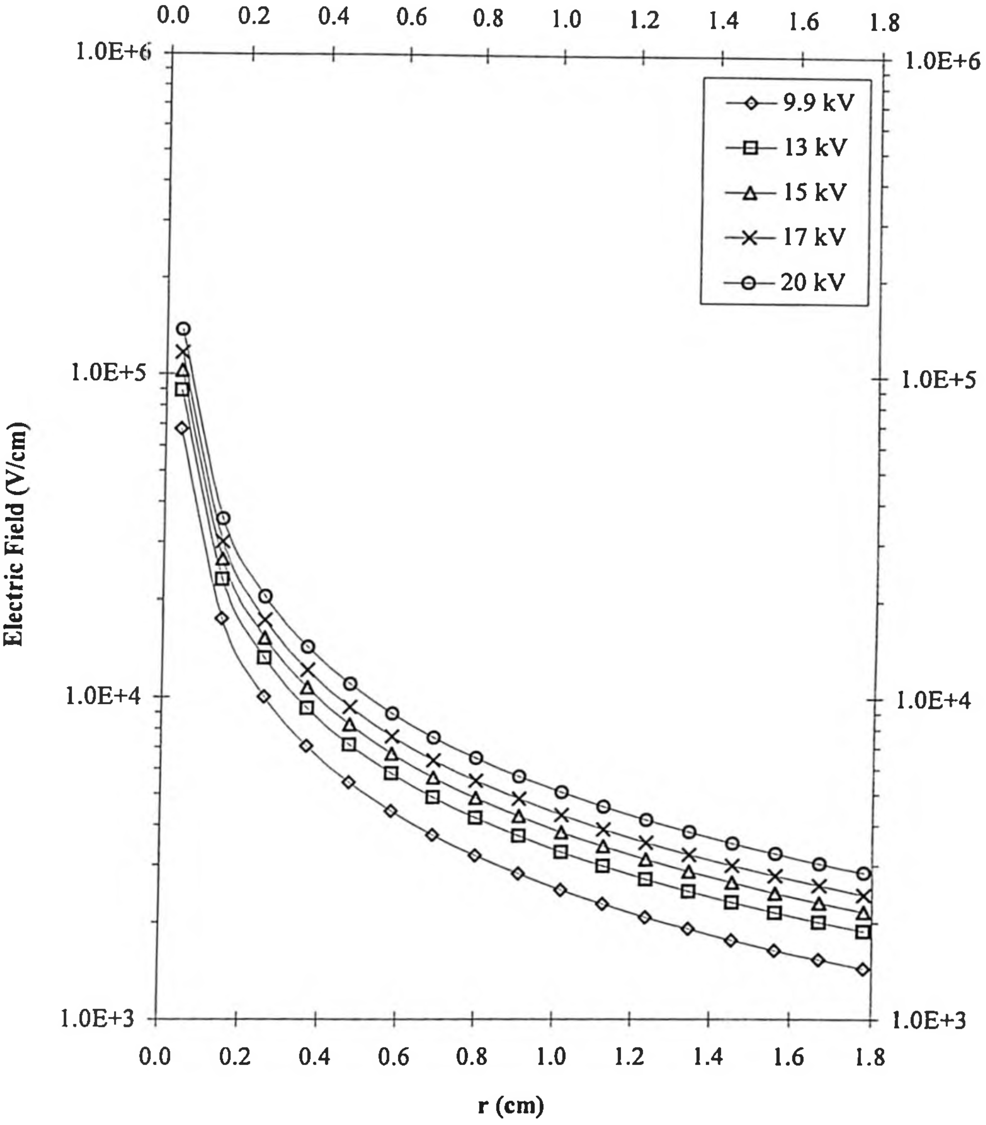

Figure 5.1.1: The effect of the applied voltage on the radial electric field profiles

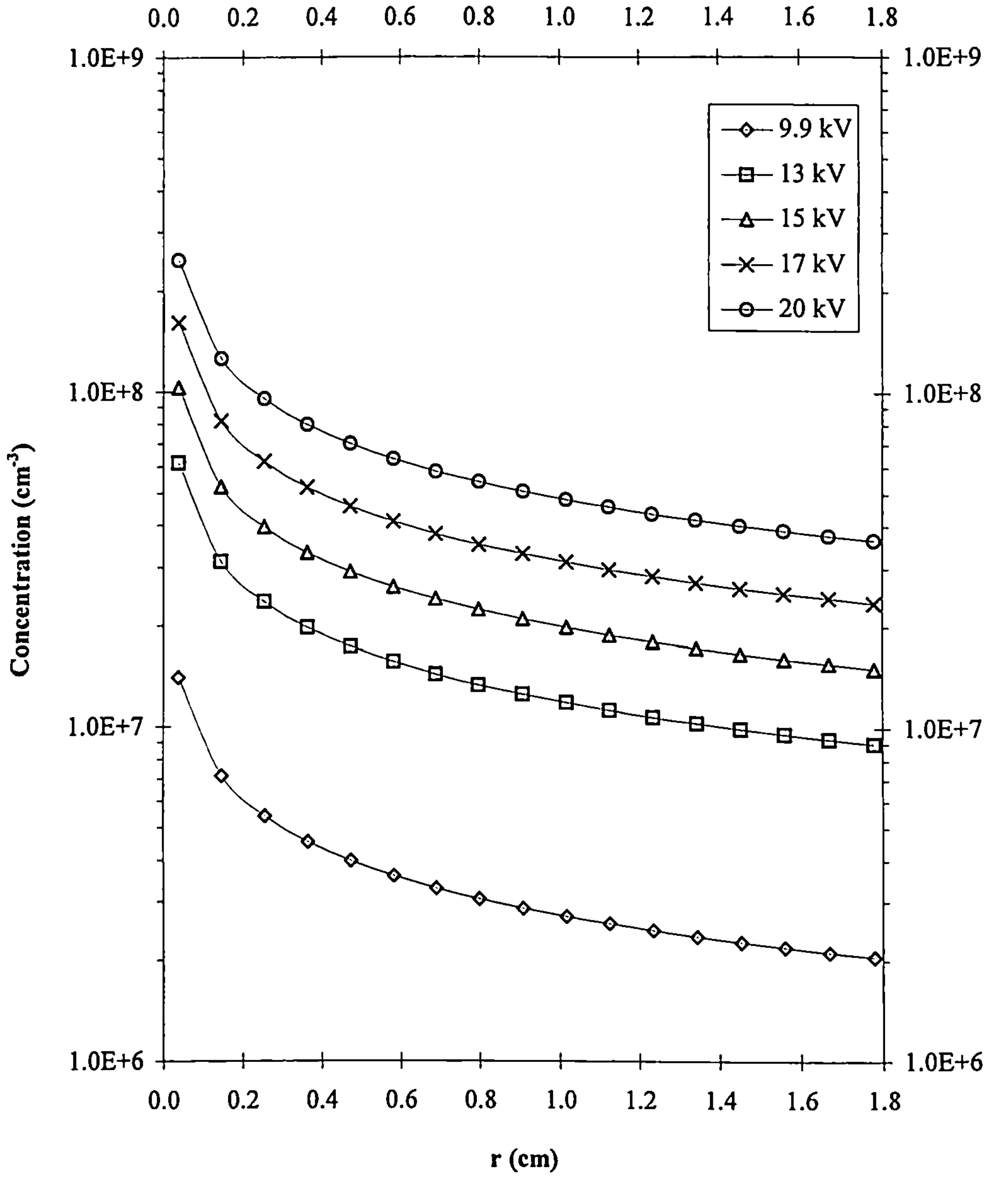

Figure 5.1.2: The effect of the applied voltage on the radial electron density profile

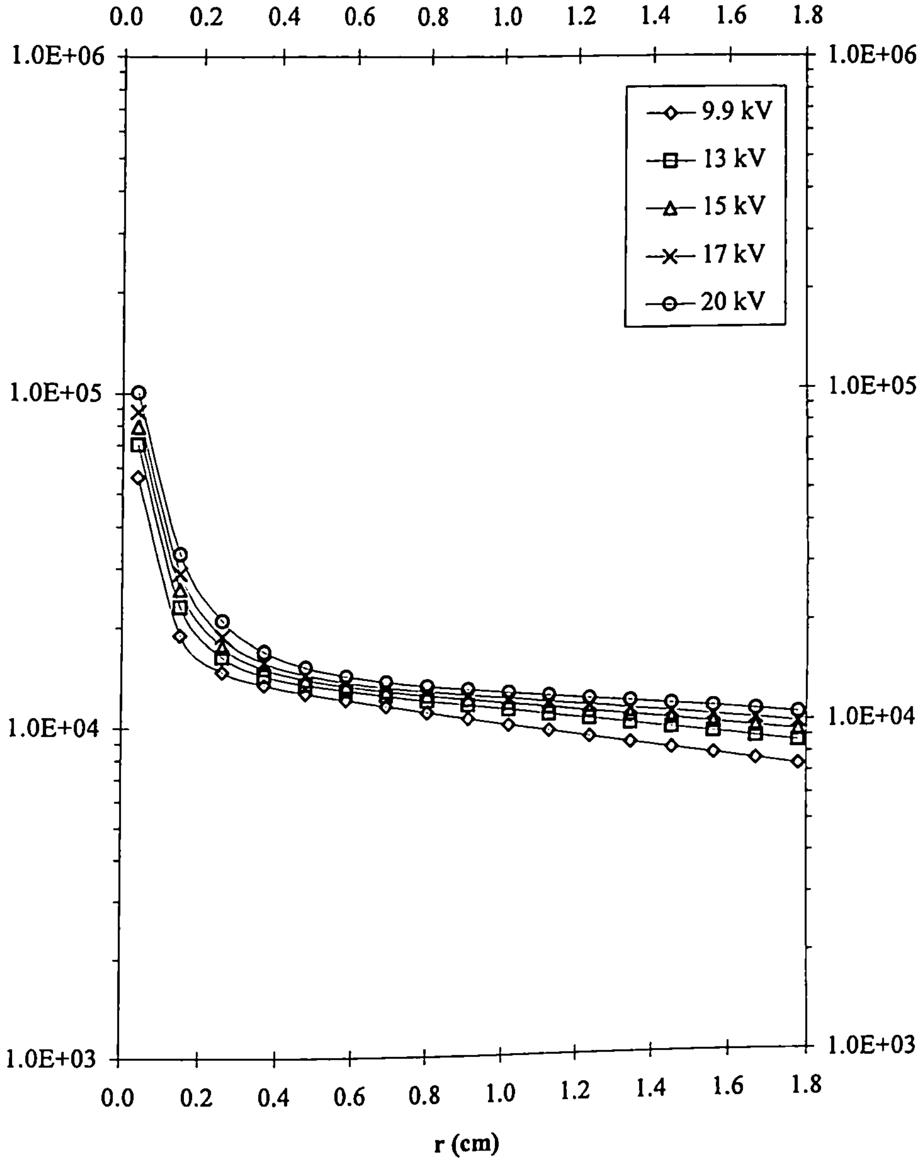

Figure 5.1.3: The effect of the applied voltage on the radial electron temperature profile

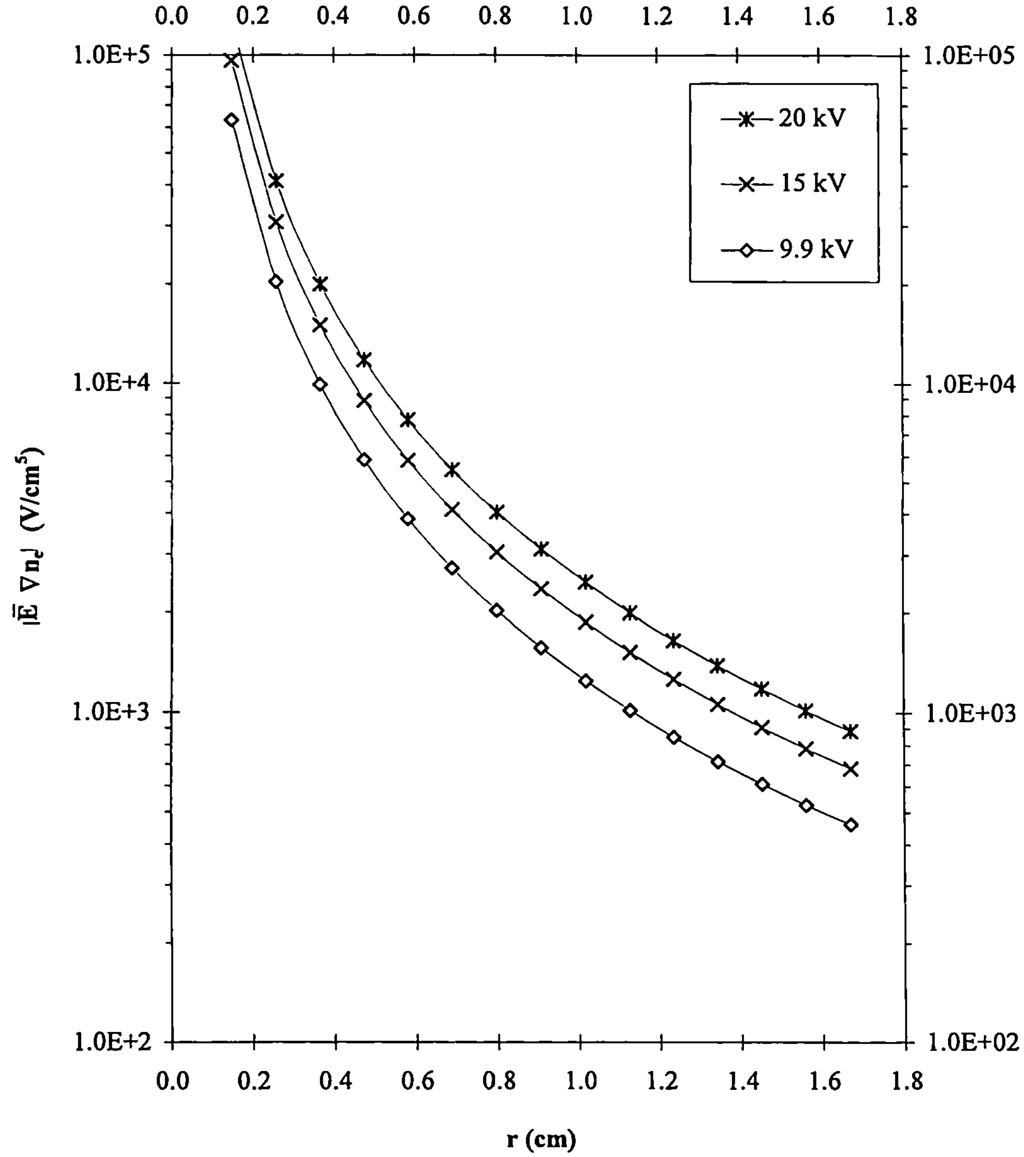

Figure 5.1.4: The effect of the applied voltage on the radial profiles of the electron density divergence times electric field

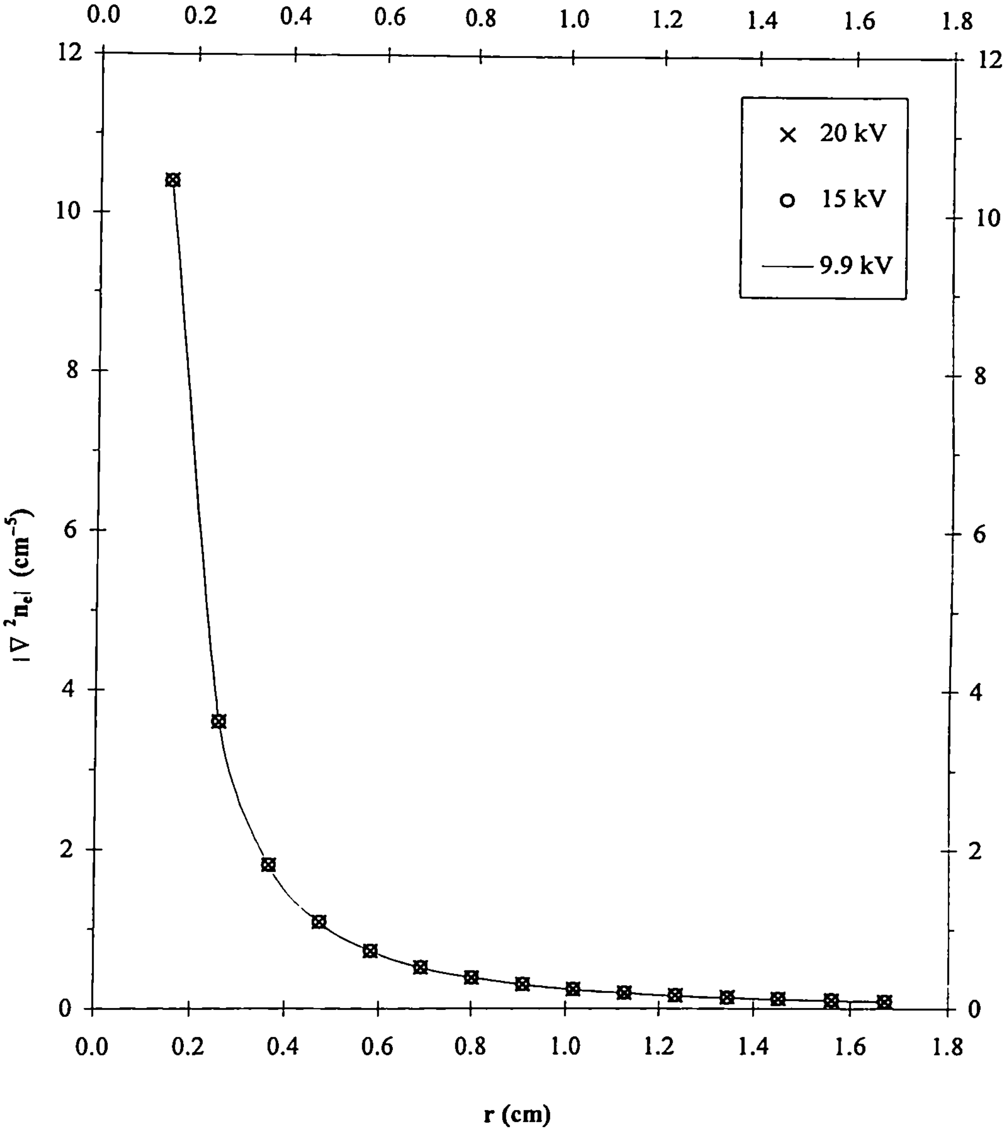

Figure 5.1.5: The effect of the applied voltage on the radial profiles of Laplacian of the electron density

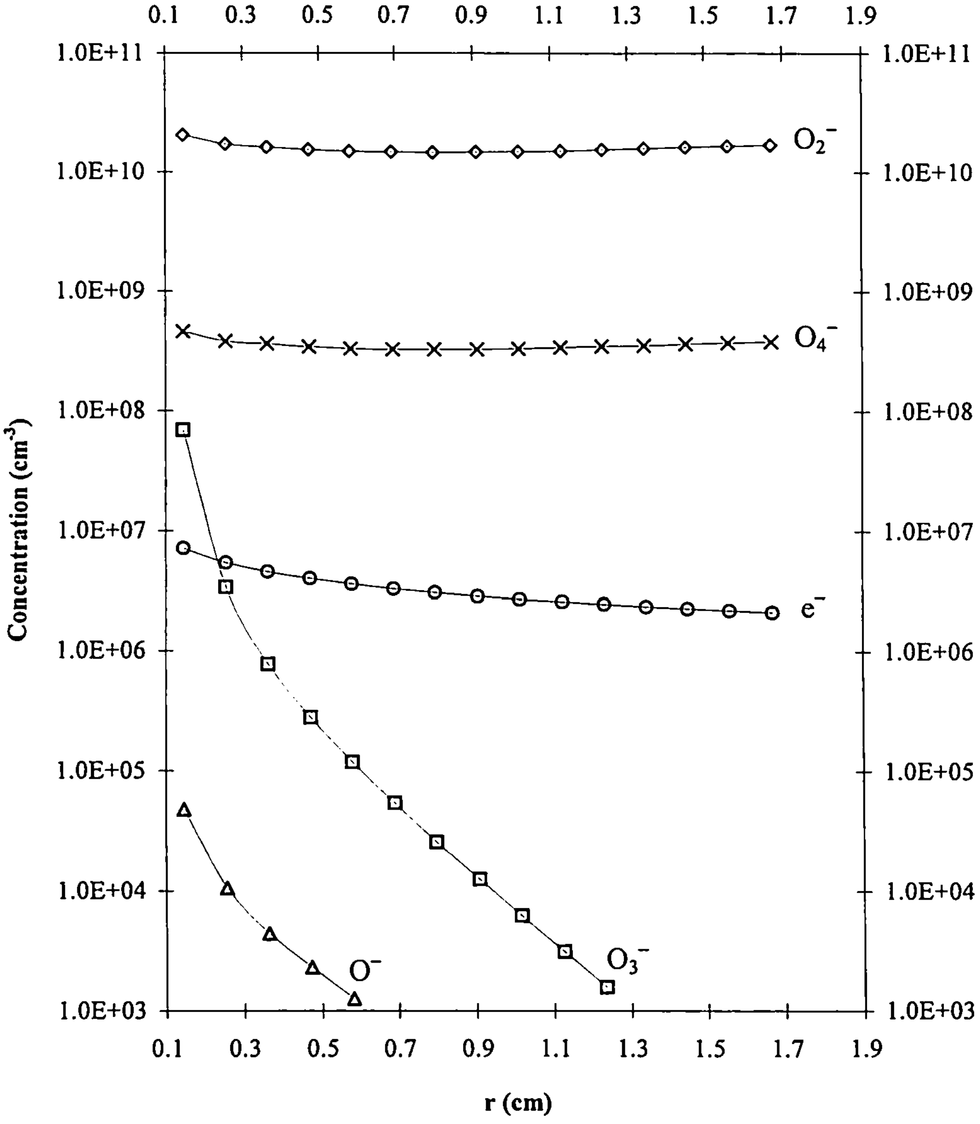

Figure 5.1.6: Radial electron and O_x^- negative ions concentration profiles for a corona discharge at $V = -9.9$ kV and $Q_g = 0$ L/min in a 21% O_2–79% N_2 atmosphere

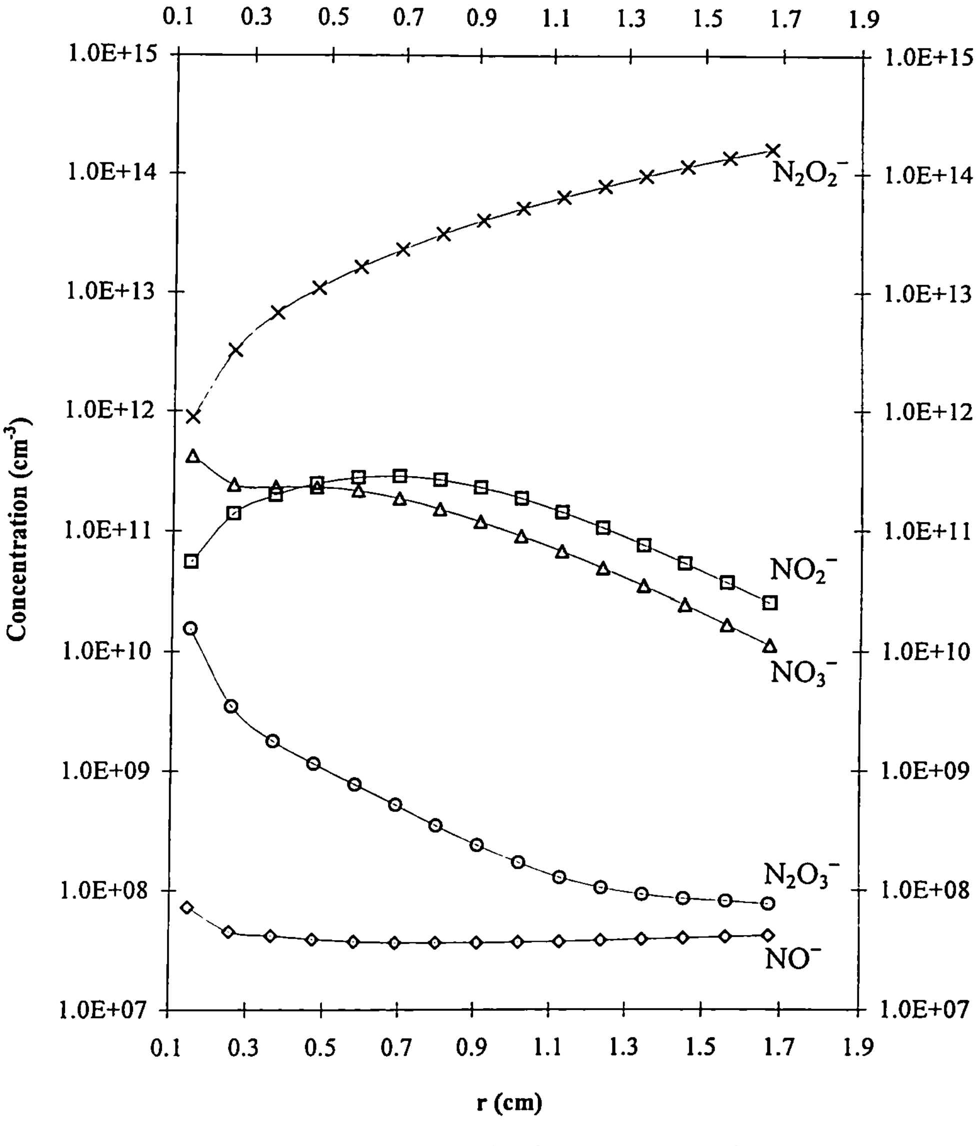

Figure 5.1.7: Radial $N_xO_y^-$ negative ions concentration profiles for a corona discharge at V = –9.9 kV and Q_g = 0 L/min in a 21% O_2–79% N_2 atmosphere

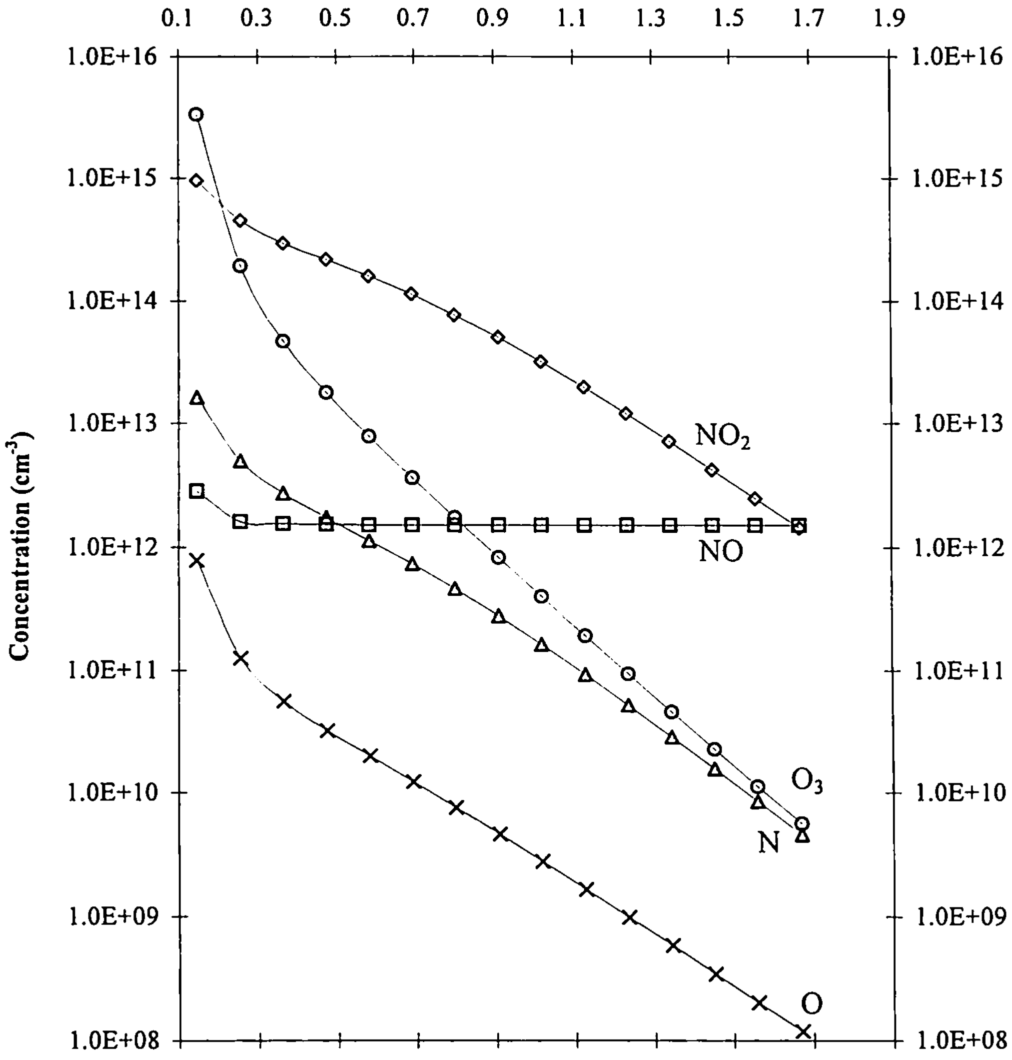

Figure 5.1.8: Radial lighter molecule radicals concentration profiles

for a corona discharge at V = –9.9 kV and Q_g = 0 L/min

in a 21% O_2–79% N_2 atmosphere

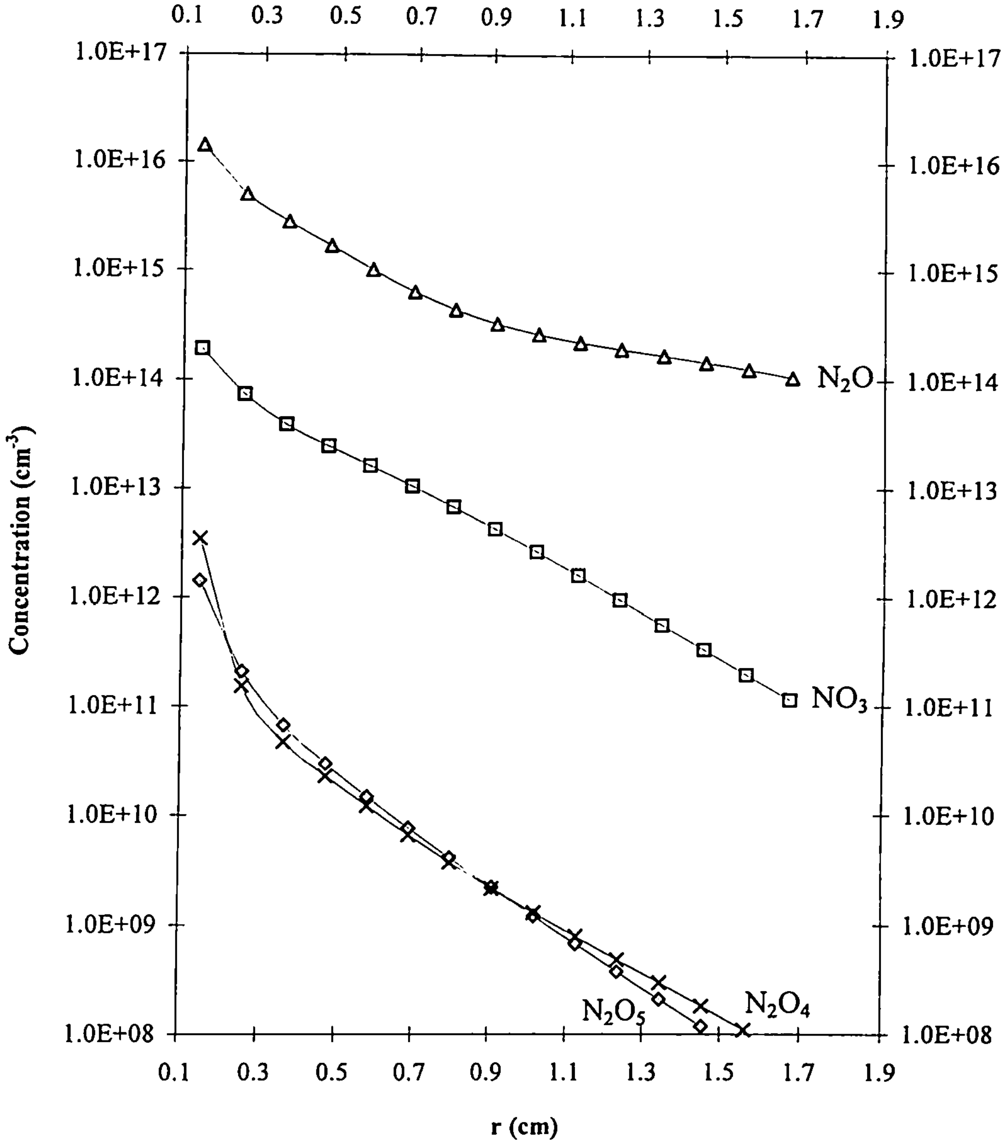

Figure 5.1.9: Radial heavier molecule radicals concentration profiles

for a corona discharge at V = –9.9 kV and Q_g = 0 L/min

in a 21% O_2–79% N_2 atmosphere

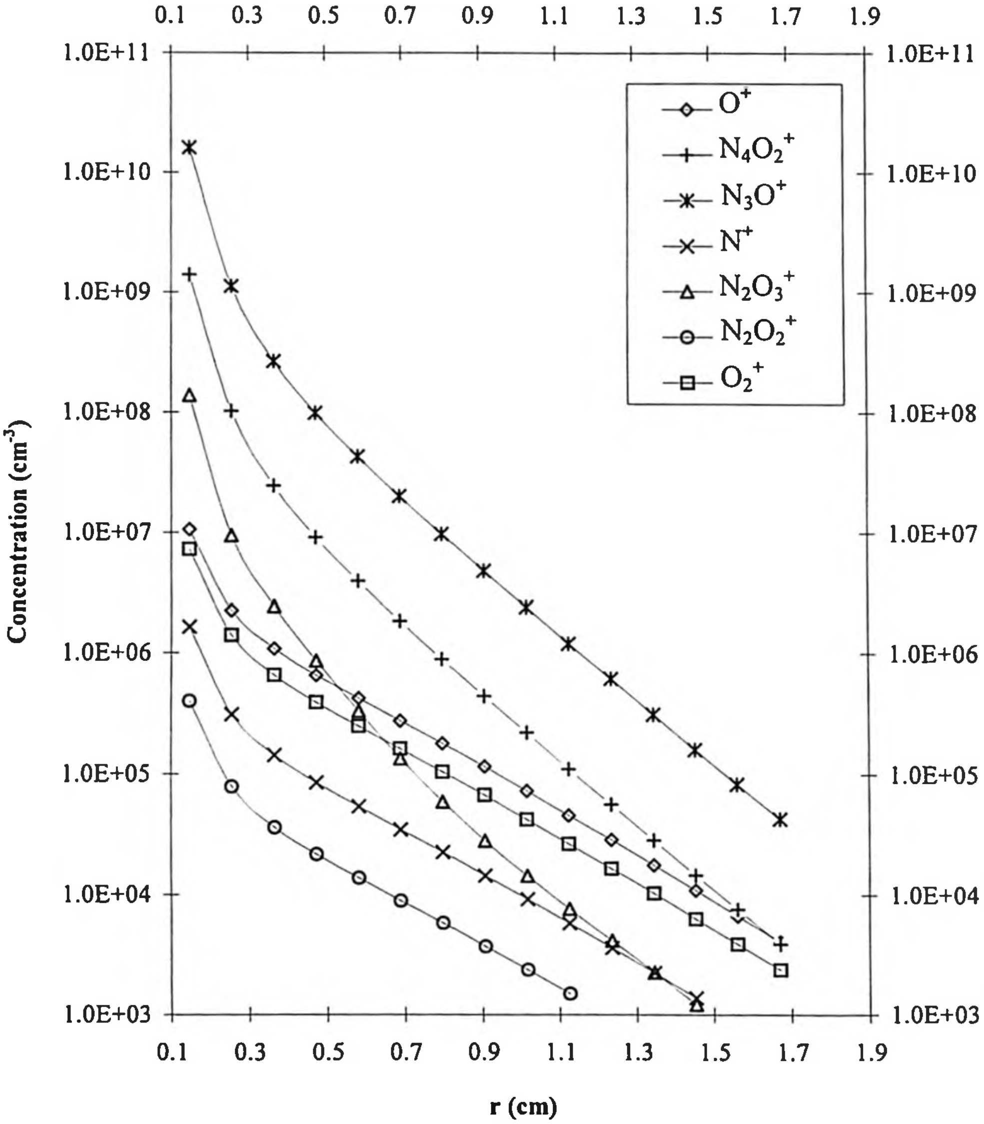

Figure 5.1.10: Radial positive ions concentration profiles for a corona discharge at V = –9.9 kV and Q_g = 0 L/min in a 21% O_2–79% N_2 atmosphere

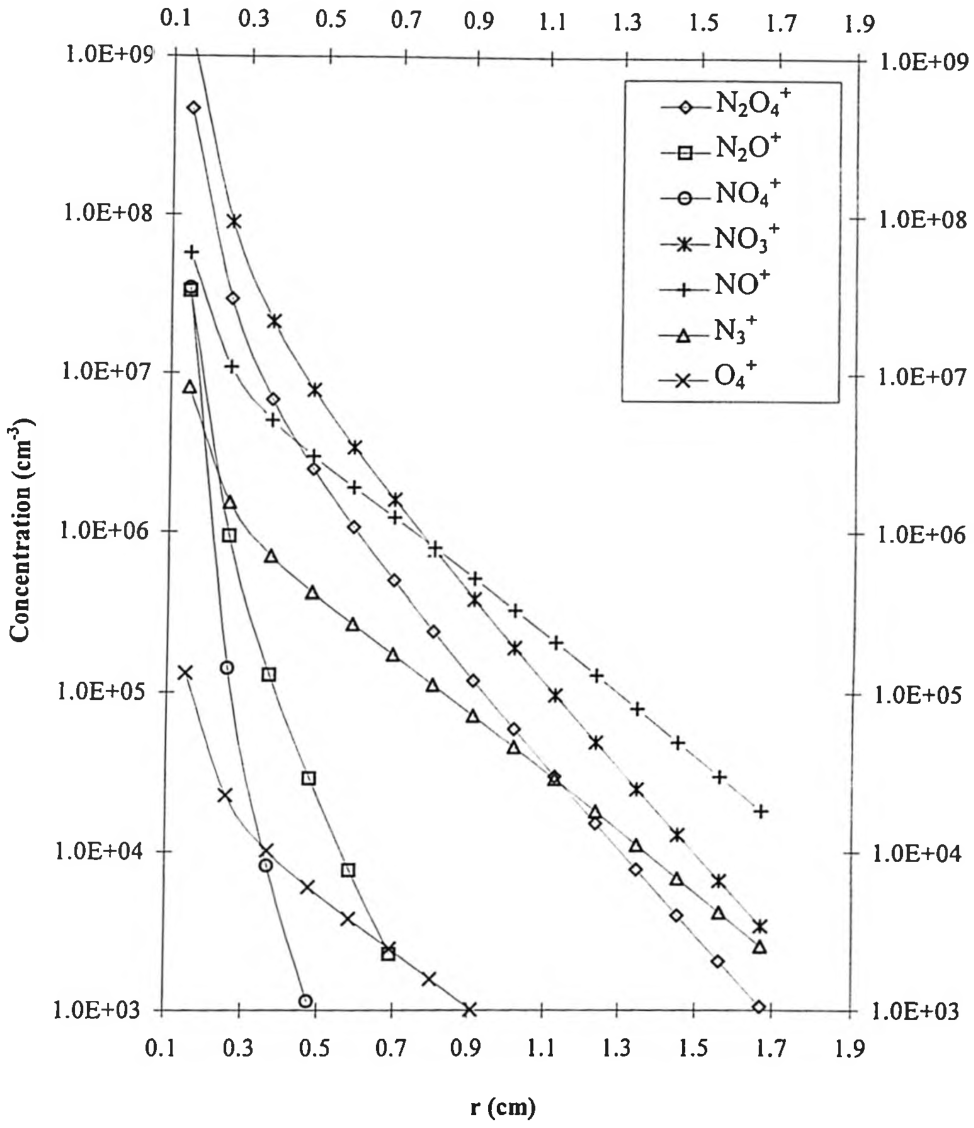

Figure 5.1.11: Radial positive ion concentration profiles for a corona discharge at V = –9.9 kV and Q_g = 0 L/min in a 21% O_2–79% N_2 atmosphere

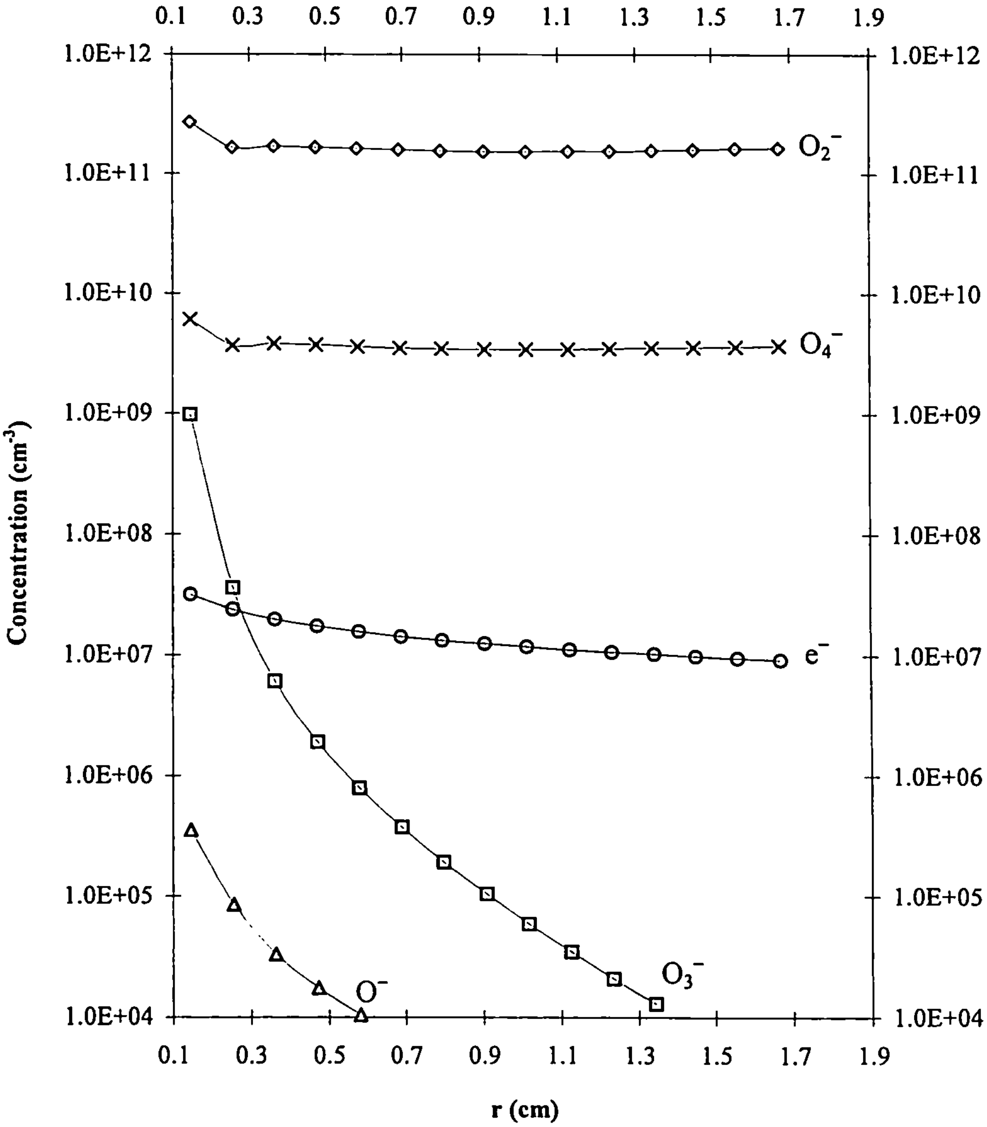

Figure 5.1.12: Radial electron and O_x^- negative ions concentration profiles for a corona discharge at $V = -13.0$ kV and $Q_g = 0$ L/min in a 21% O_2–79% N_2 atmosphere

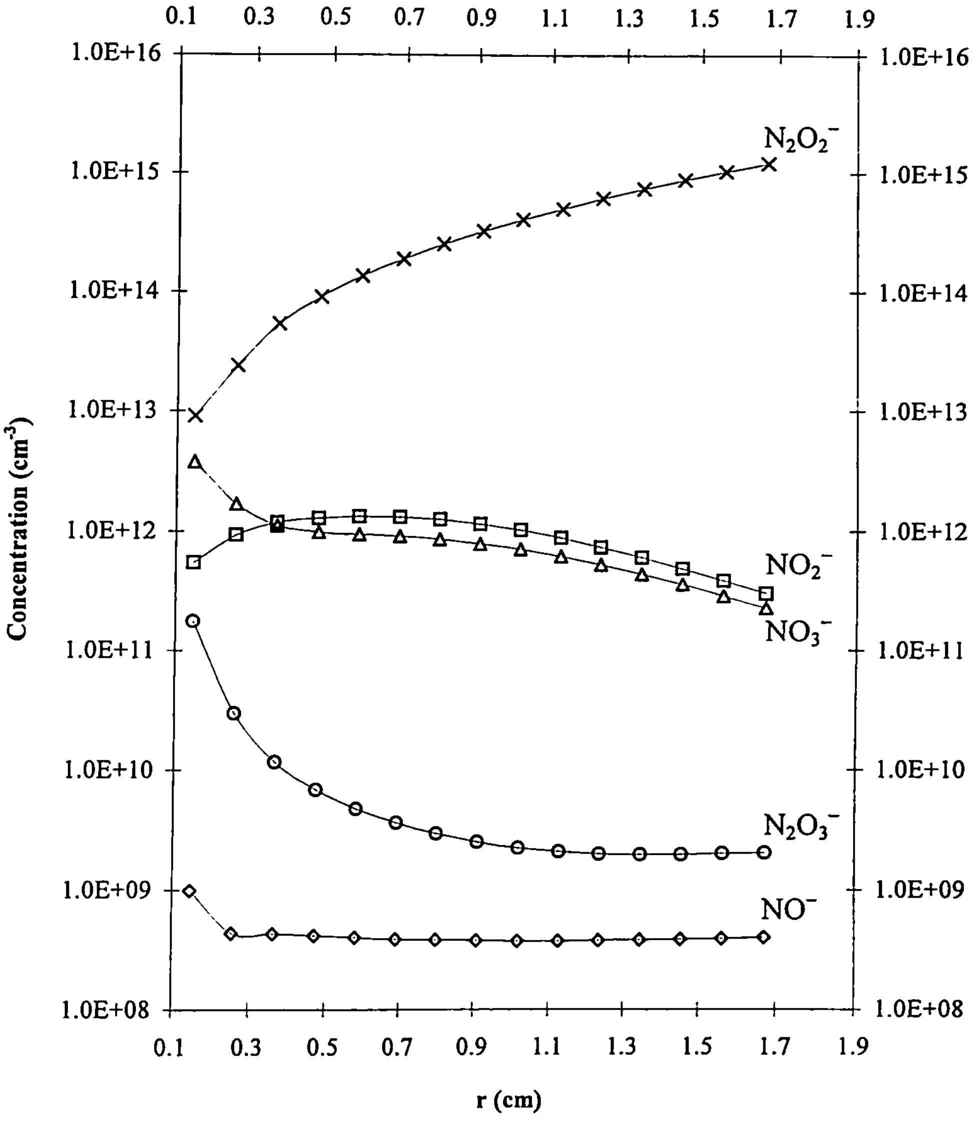

Figure 5.1.13: Radial $N_xO_y^-$ negative ions concentration profiles for a corona discharge at $V = -13.0$ kV and $Q_g = 0$ L/min in a 21% O_2–79% N_2 atmosphere

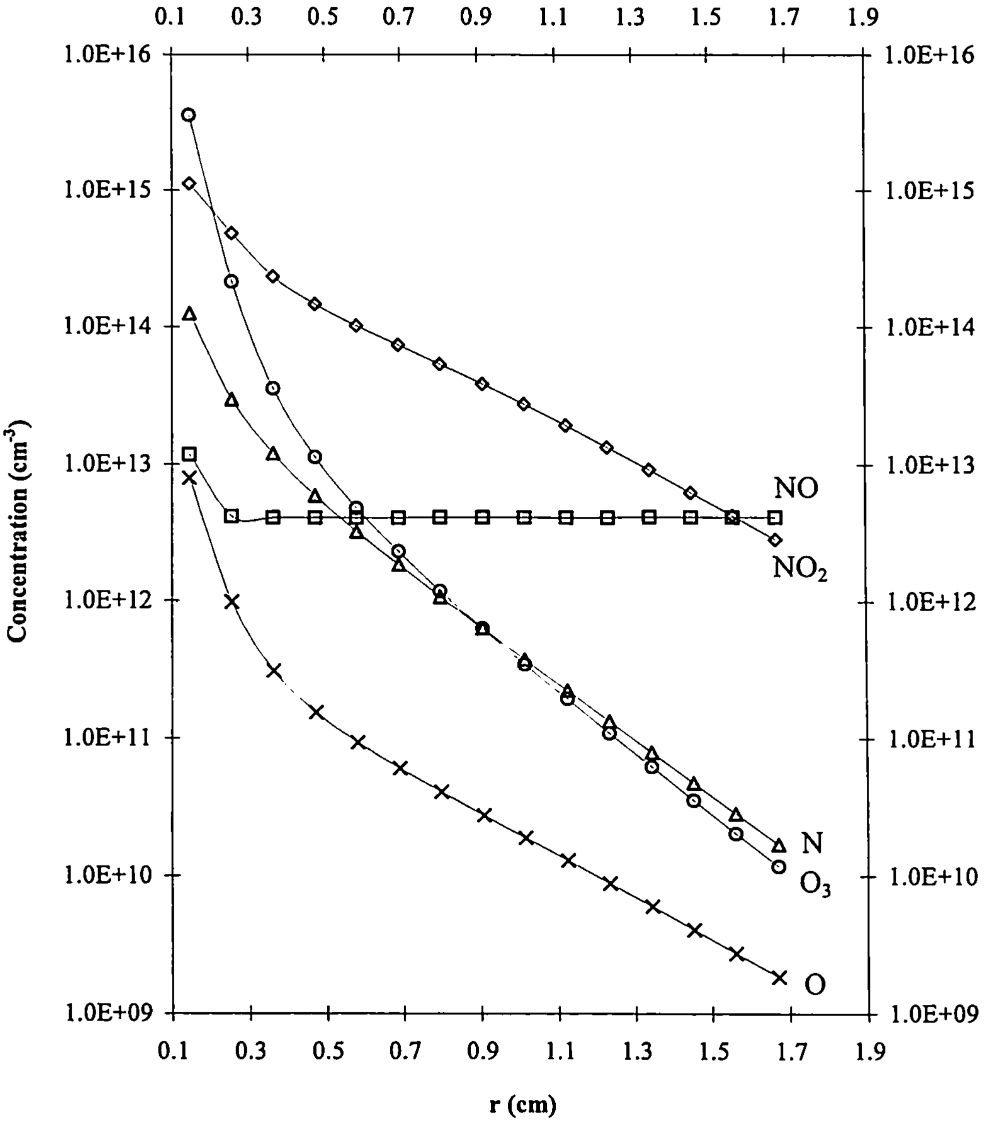

Figure 5.1.14: Radial lighter molecule radicals concentrations profiles for a corona discharge at V = –13.0 kV and Q_g = 0 L/min in a 21% O_2–79% N_2 atmosphere

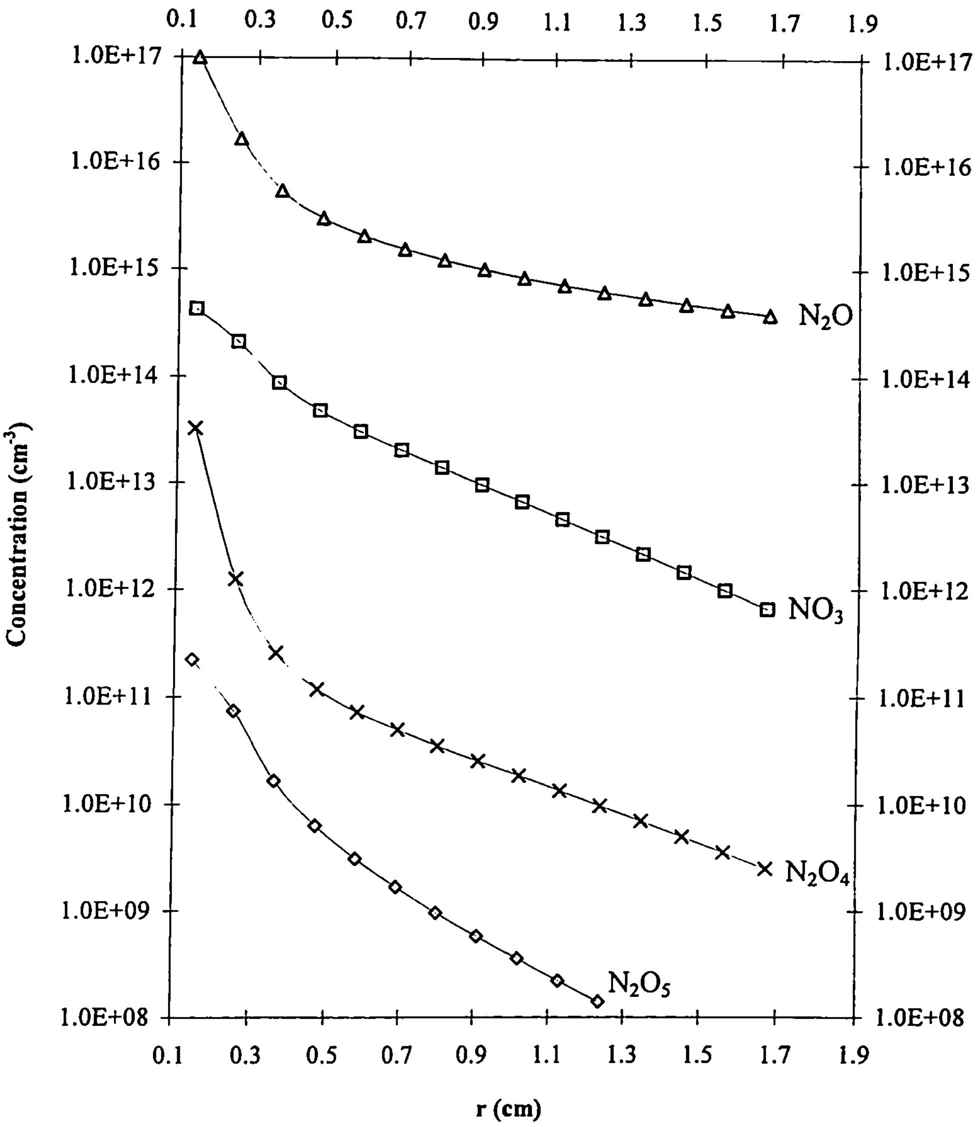

Figure 5.1.15: Radial heavier molecule radicals concentration profiles for a corona discharge at V = –13.0 kV and Q_g = 0 L/min in a 21% O_2–79% N_2 atmosphere

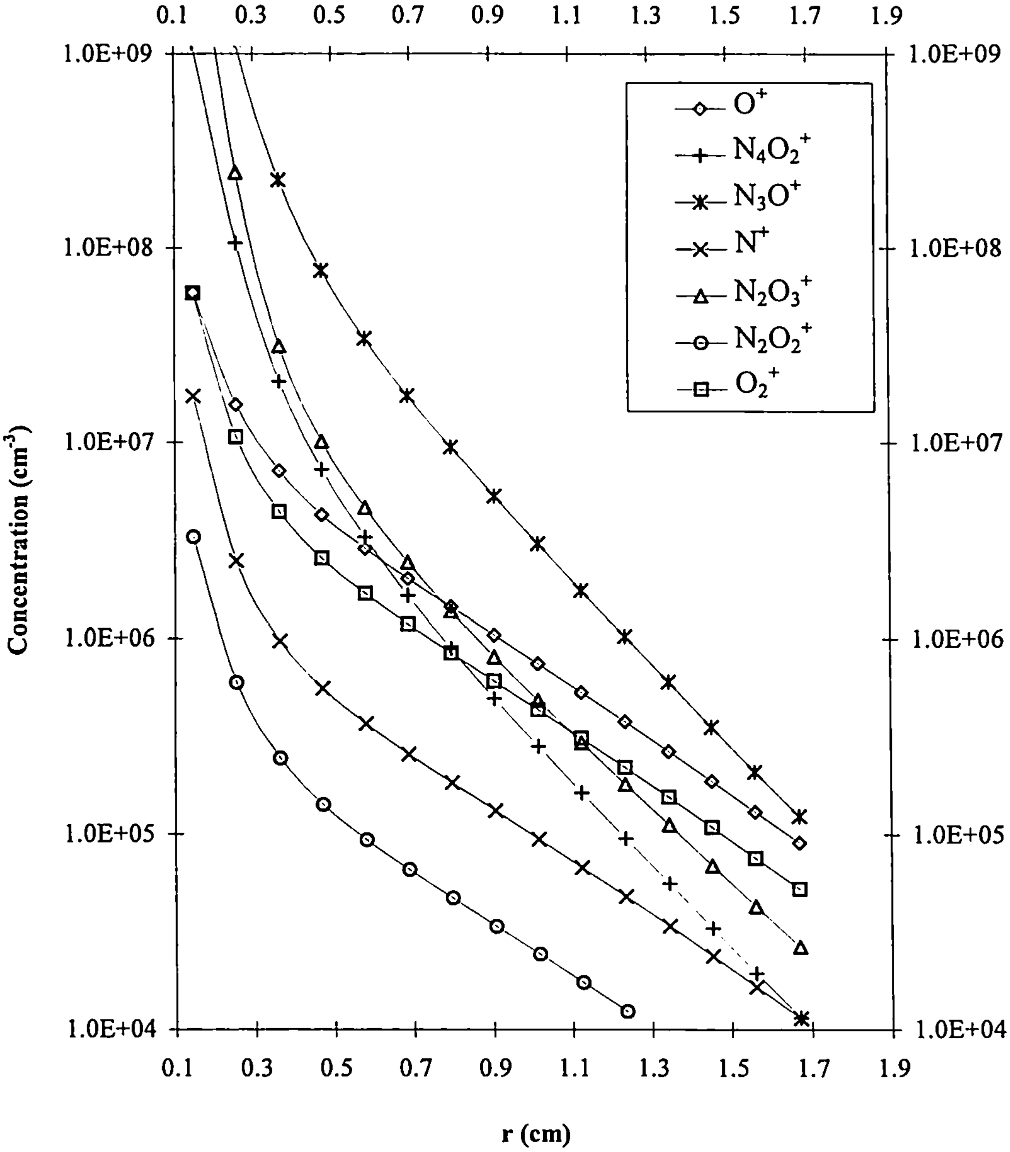

Figure 5.1.16: Radial positive ions concentration profiles for a corona discharge at V = –13.0 kV and Q_g = 0 L/min in a 21% O_2–79% N_2 atmosphere

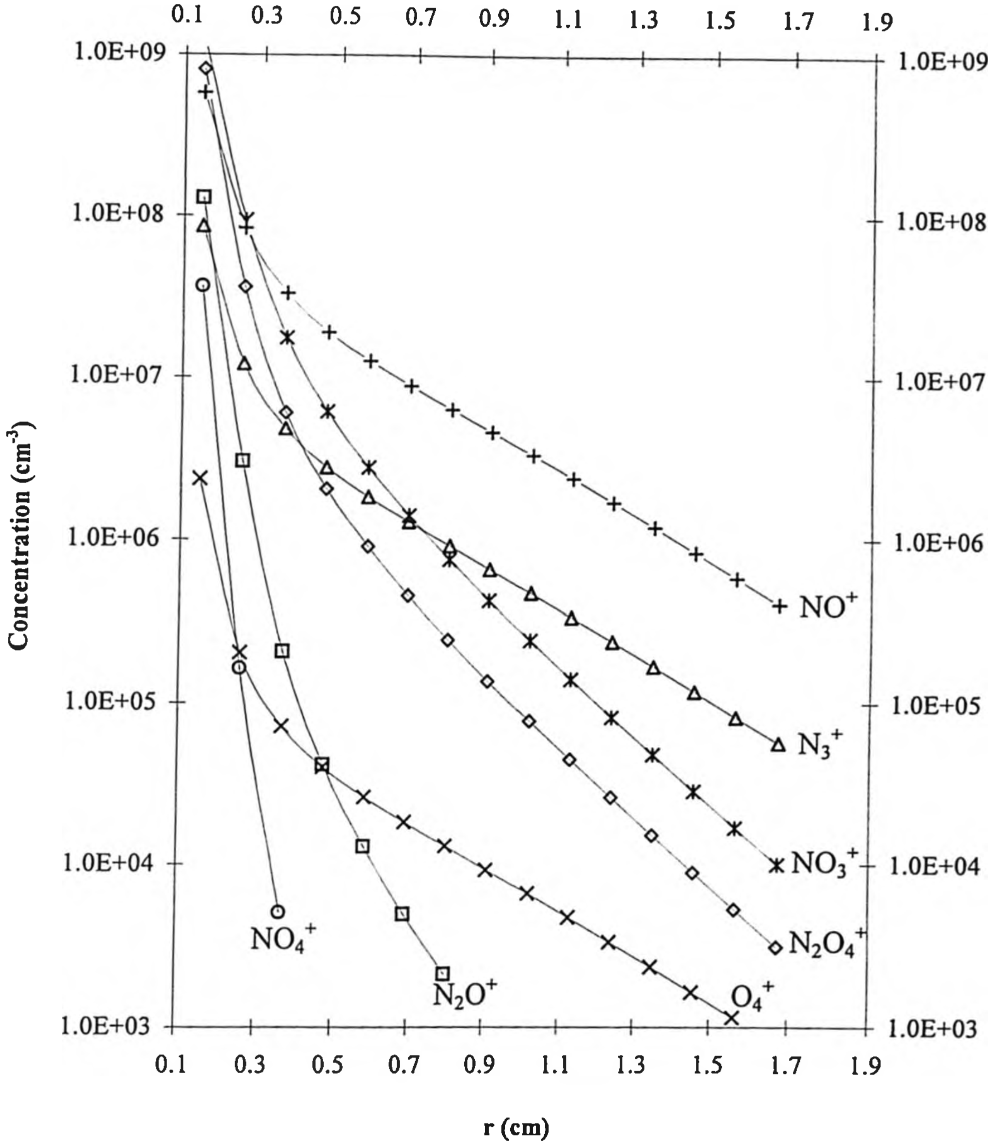

Figure 5.1.17: Radial positive ions concentrations profiles for a corona discharge at V = –13.0 kV and Q_g = 0 L/min in a 21% O_2–79% N_2 atmosphere

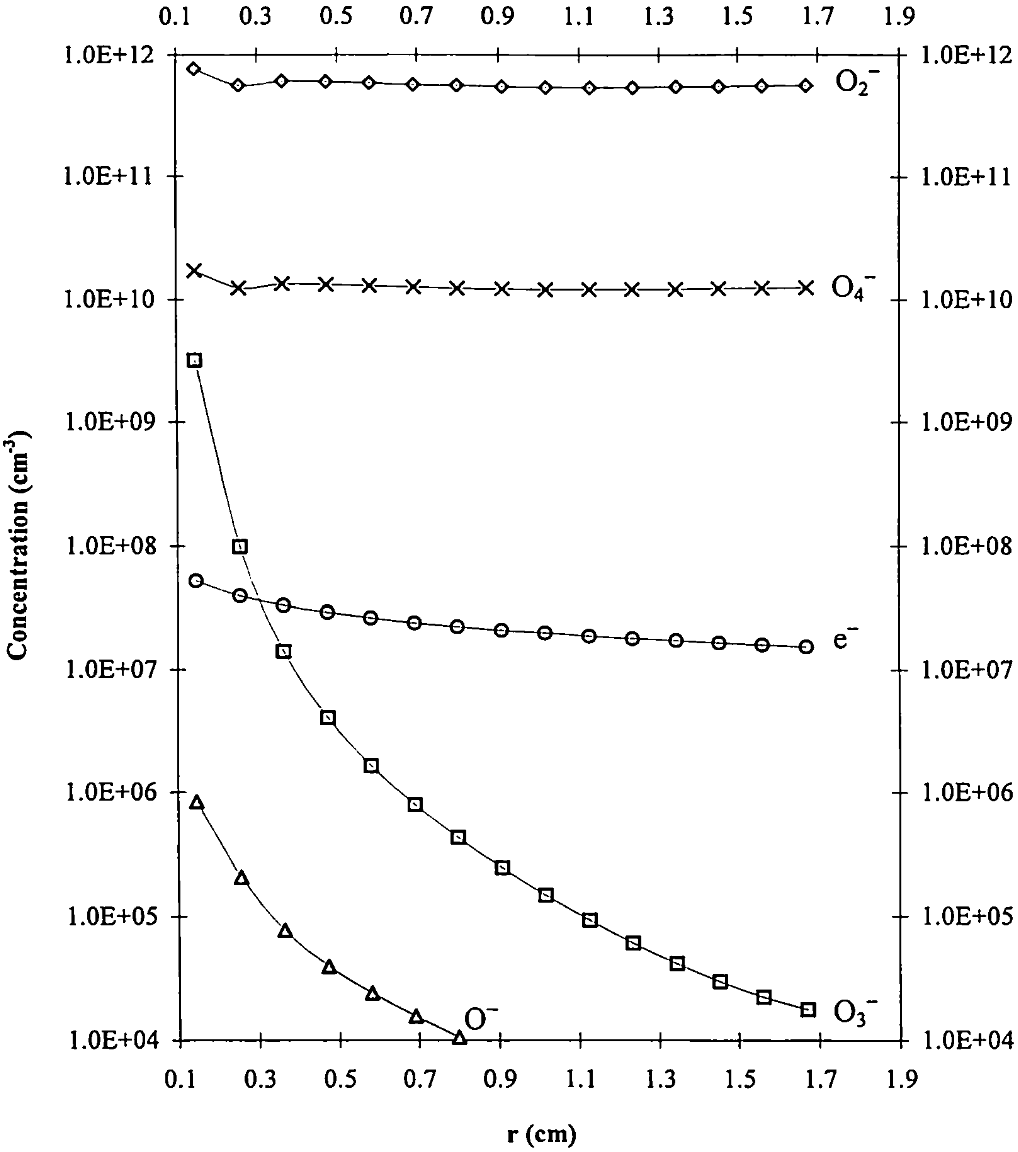

Figure 5.1.18: Radial electron and O_x^- negative ions concentration profiles for a corona discharge at $V = -15.0$ kV and $Q_g = 0$ L/min in a 21% O_2–79% N_2 atmosphere

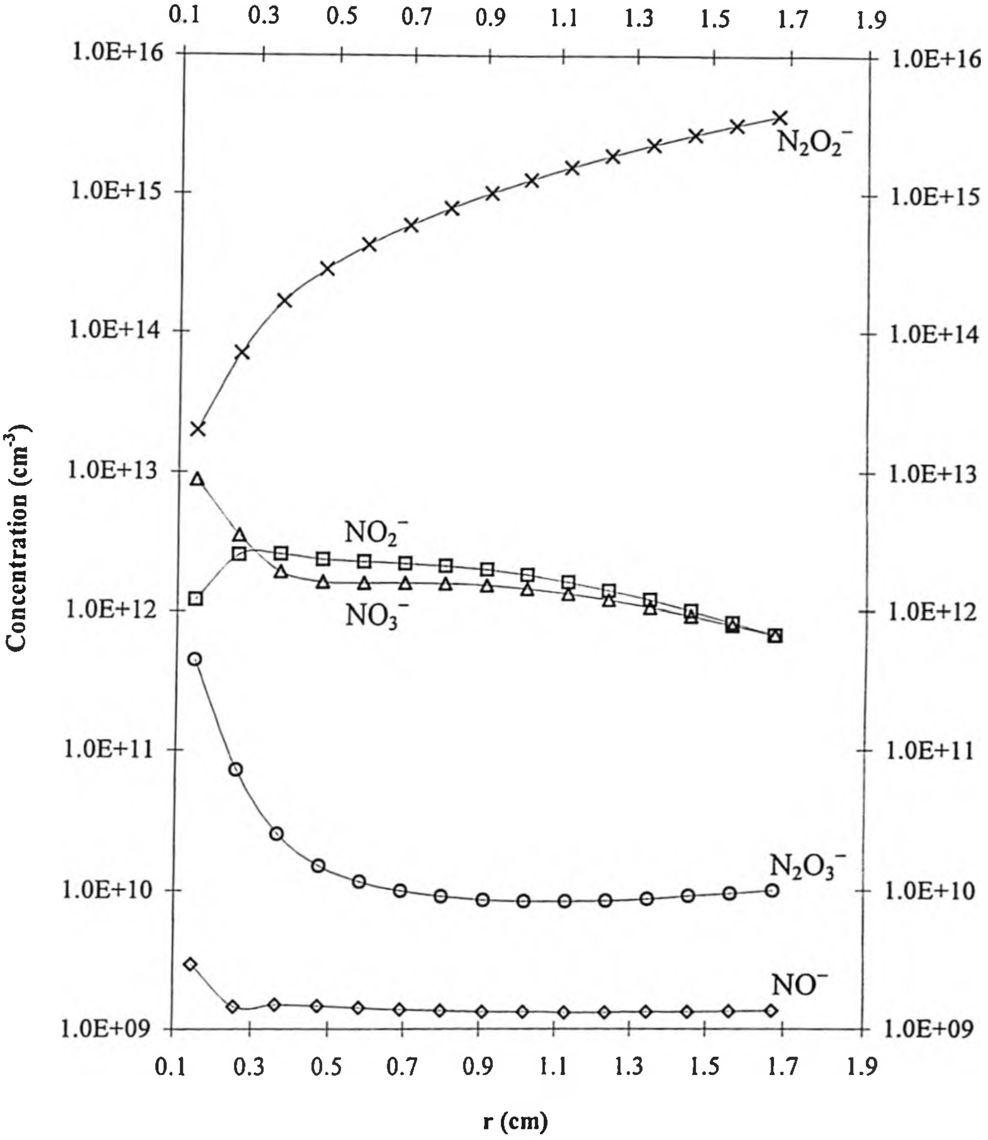

Figure 5.1.19: Radial $N_xO_y^-$ negative ions concentration profiles for a corona discharge at V = –15.0 kV and Q_g = 0 L/min in a 21% O_2–79% N_2 atmosphere

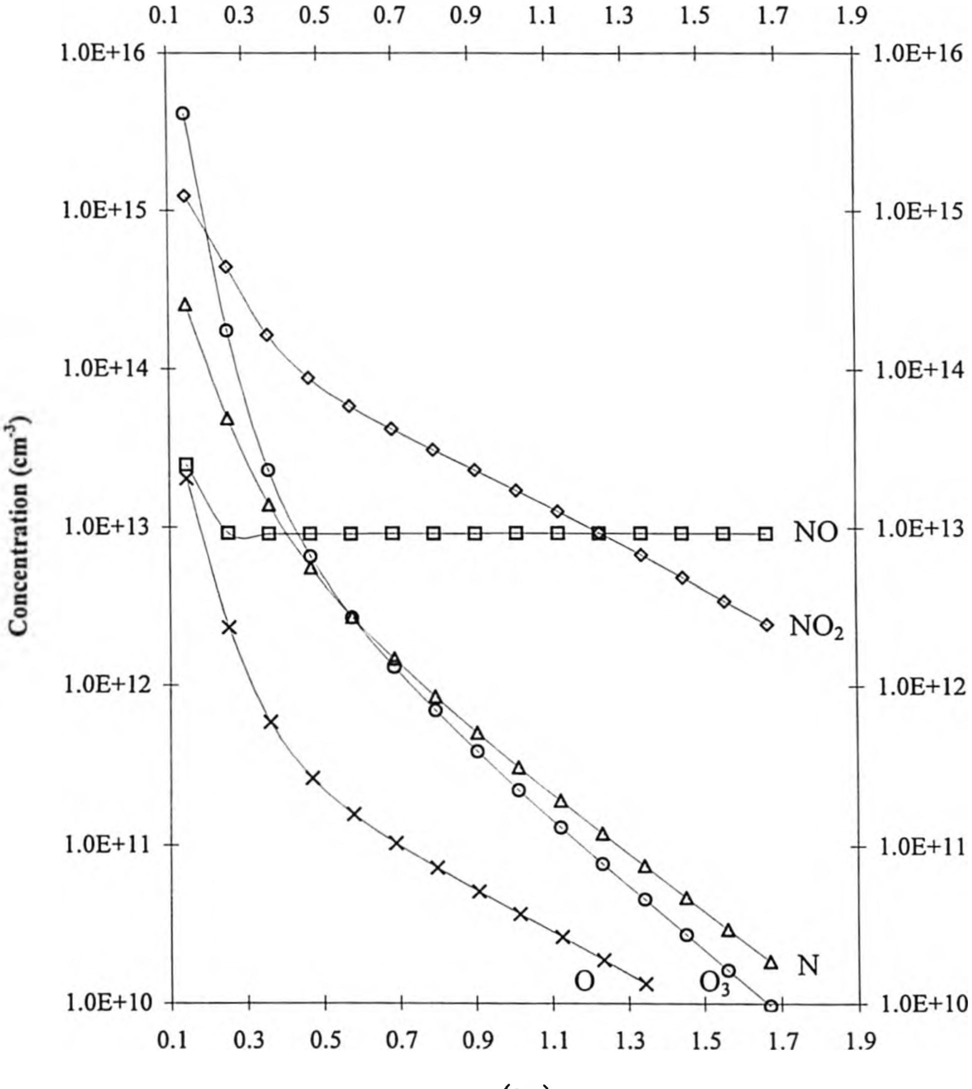

Figure 5.1.20: Radial lighter molecule radicals concentration profiles for a corona discharge at V = –15.0 kV and Q_g = 0 L/min in a 21% O_2–79% N_2 atmosphere

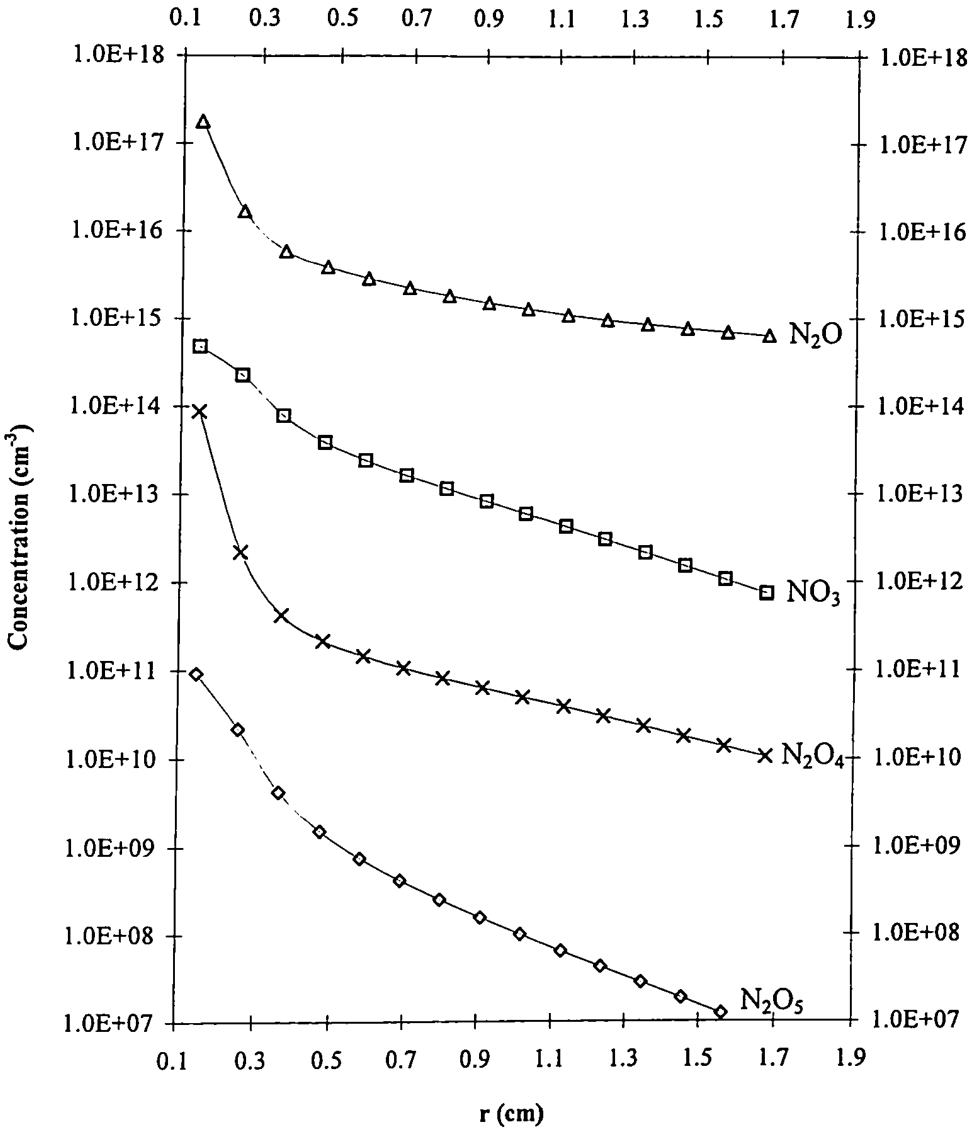

Figure 5.1.21: Radial heavier molecule radicals concentration profiles for a corona discharge at V = –15.0 kV and Q_g = 0 L/min in a 21% O_2–79% N_2 atmosphere

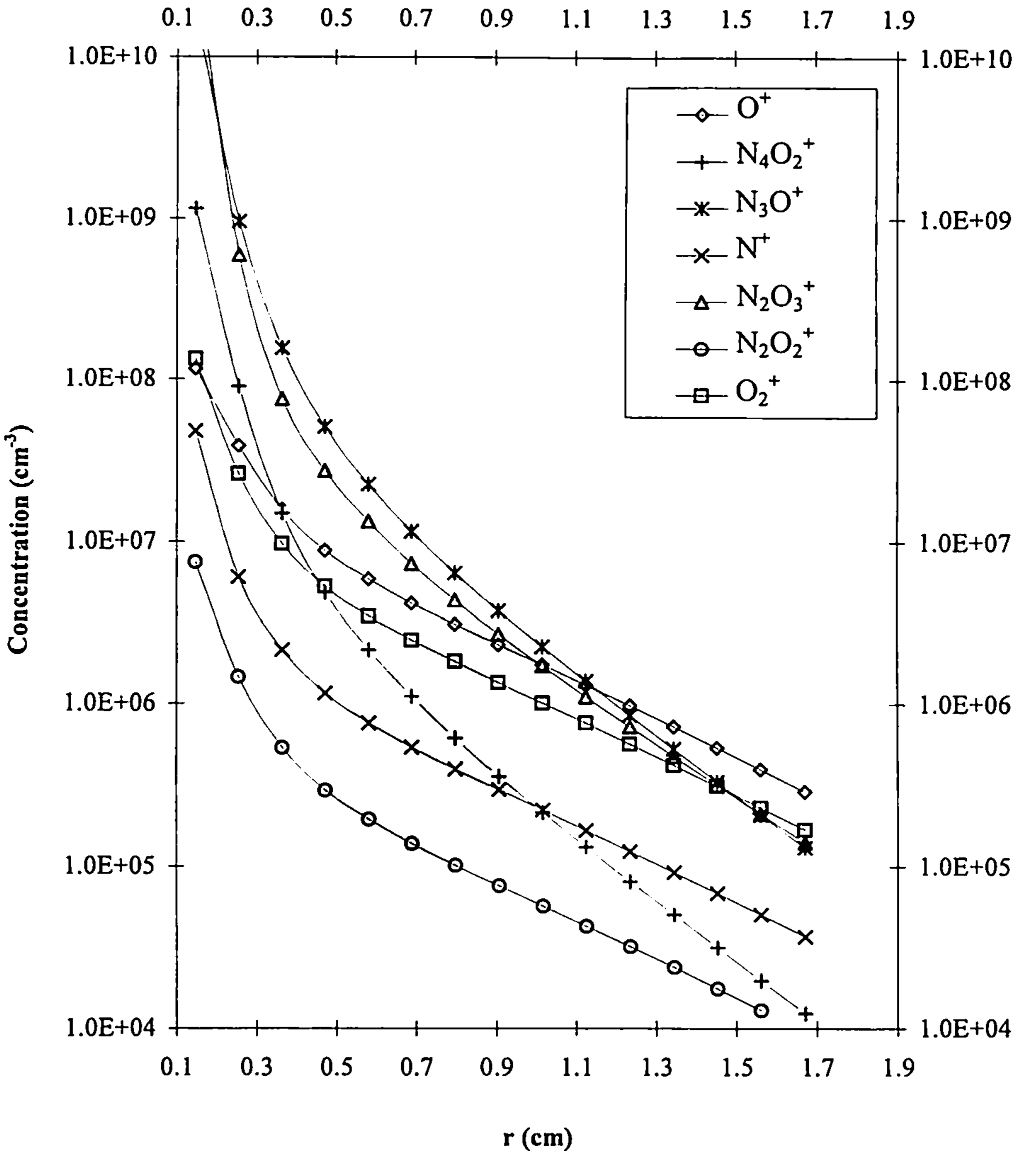

Figure 5.1.22: Radial positive ions concentration profiles for a corona discharge at V = –15.0 kV and Q_g = 0 L/min in a 21% O_2–79% N_2 atmosphere

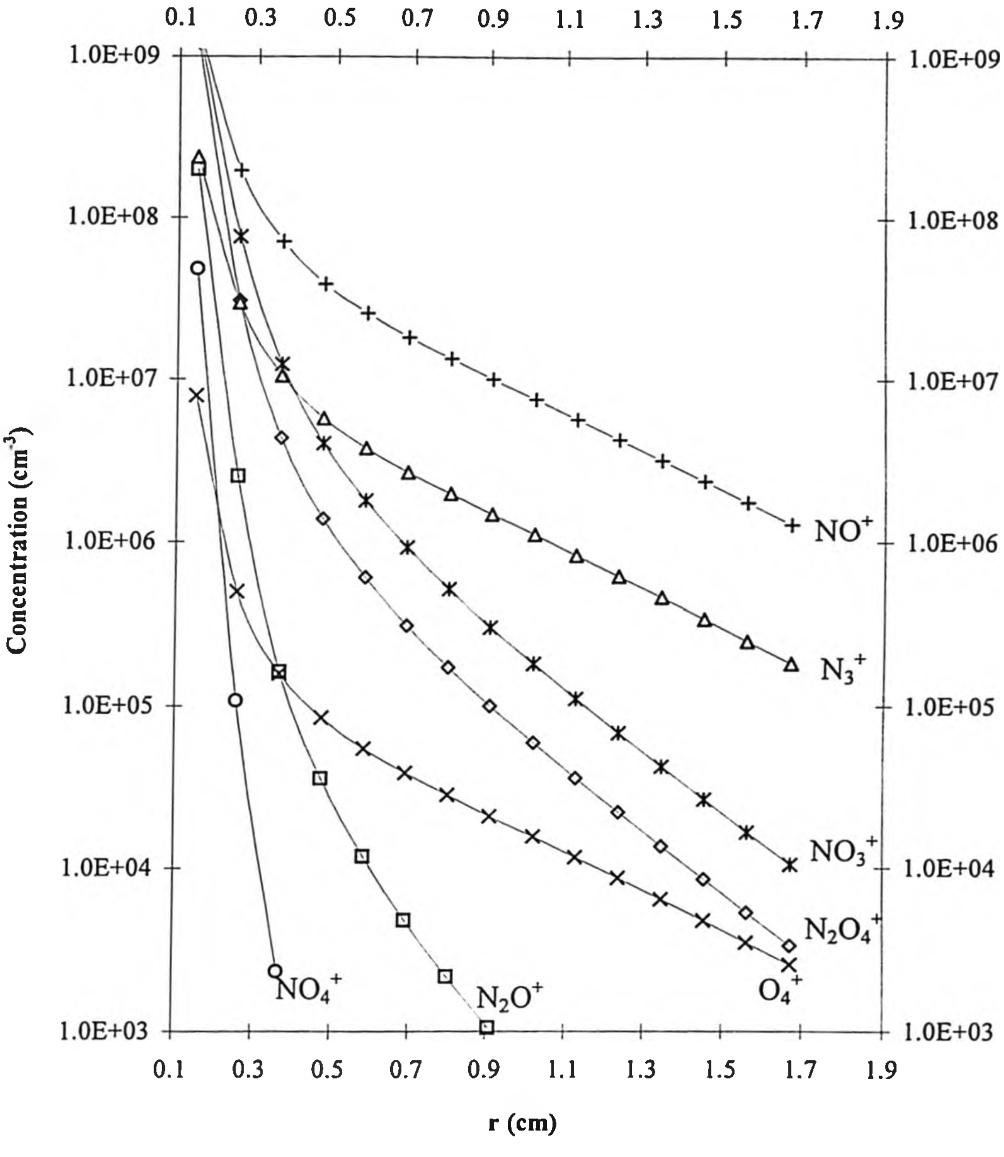

Figure 5.1.23: Radial positive ions concentration profiles for a corona discharge at V = –15.0 kV and Q_g = 0 L/min in a 21% O_2–79% N_2 atmosphere

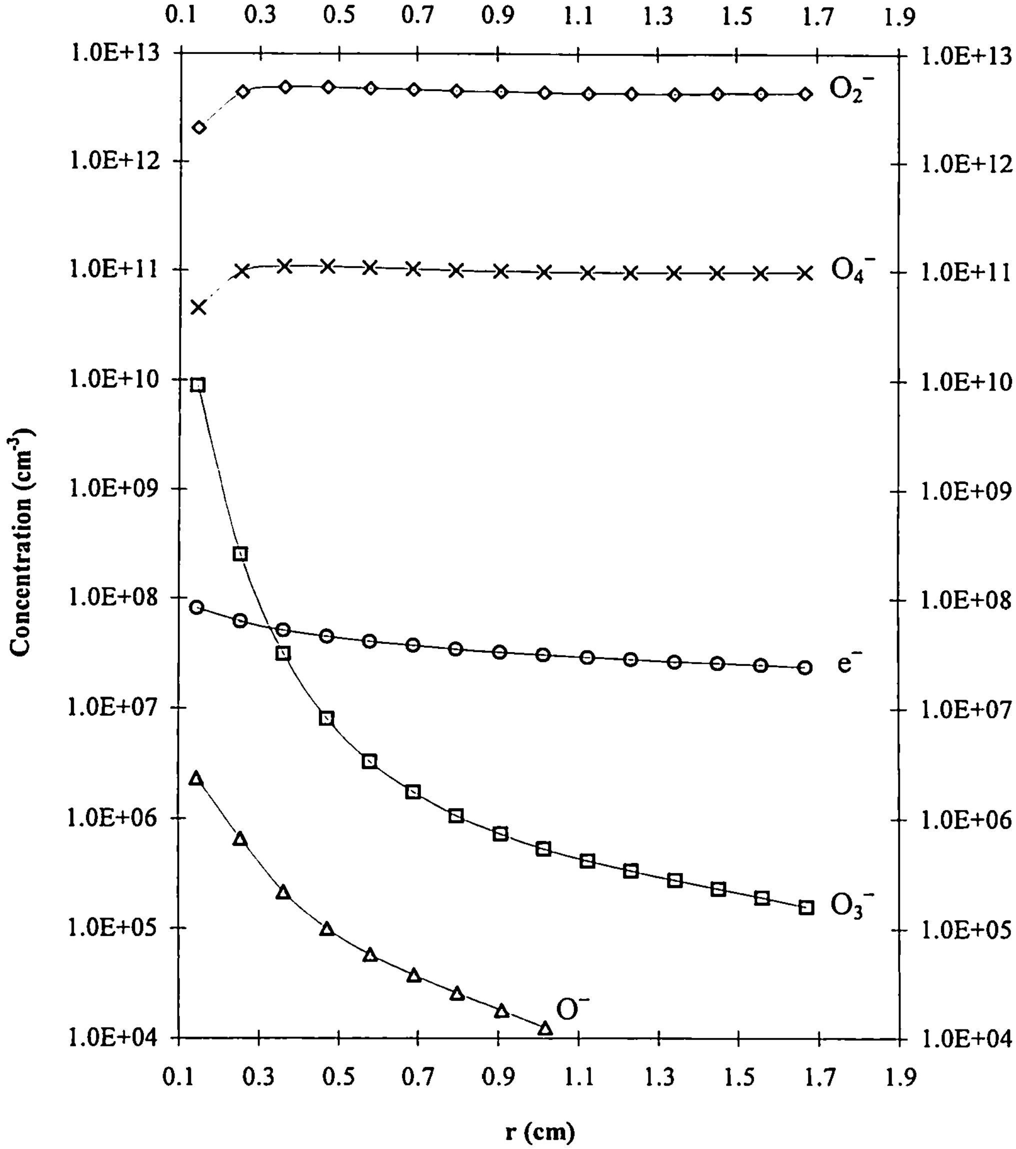

Figure 5.1.24: Radial electron and O_x^- negative ions concentration profiles for a corona discharge at V = –17.0 kV and Q_g = 0 L/min in a 21% O_2–79% N_2 atmosphere

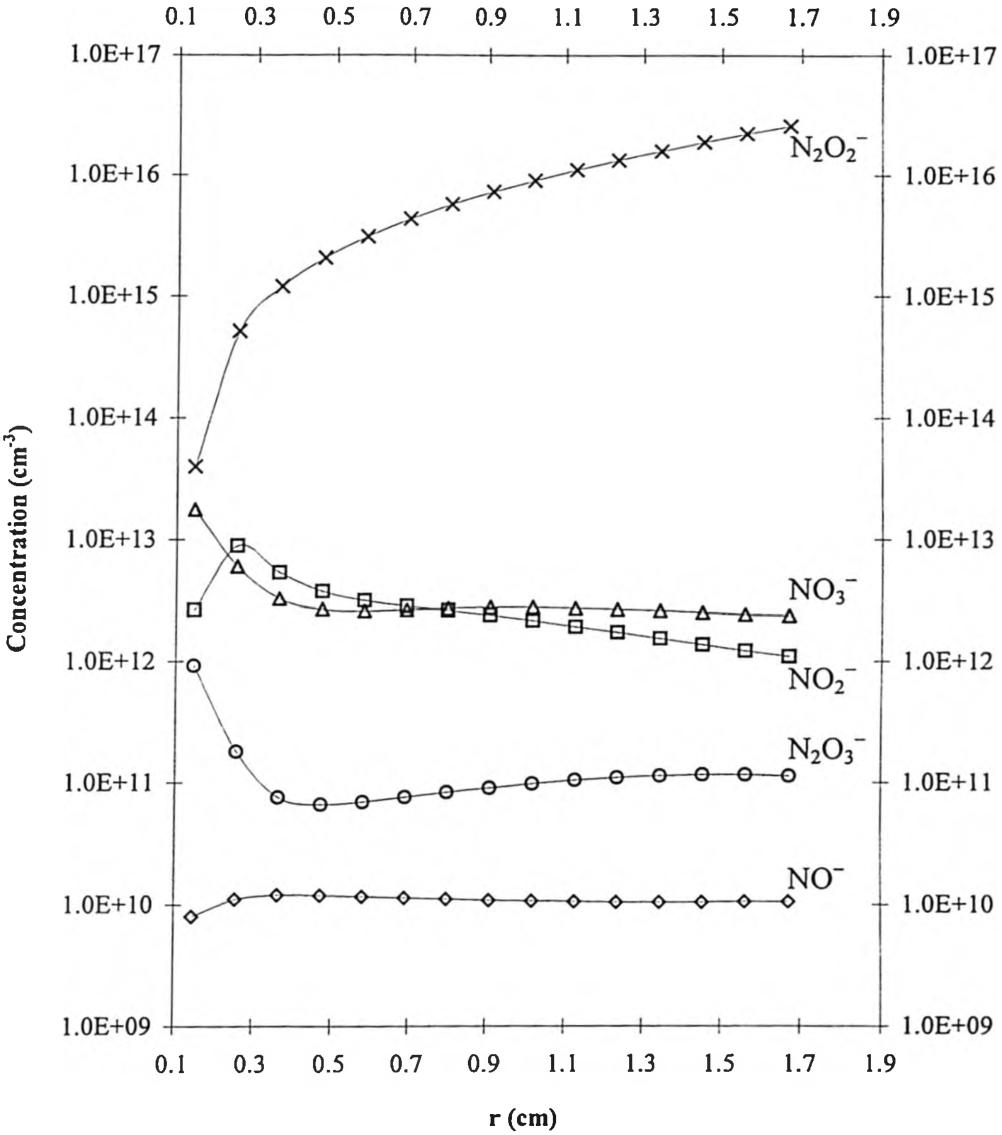

Figure 5.1.25: Radial $N_xO_y^-$ negative ions concentration profiles for a corona discharge at V = –17.0 kV and Q_g = 0 L/min in a 21% O_2–79% N_2 atmosphere

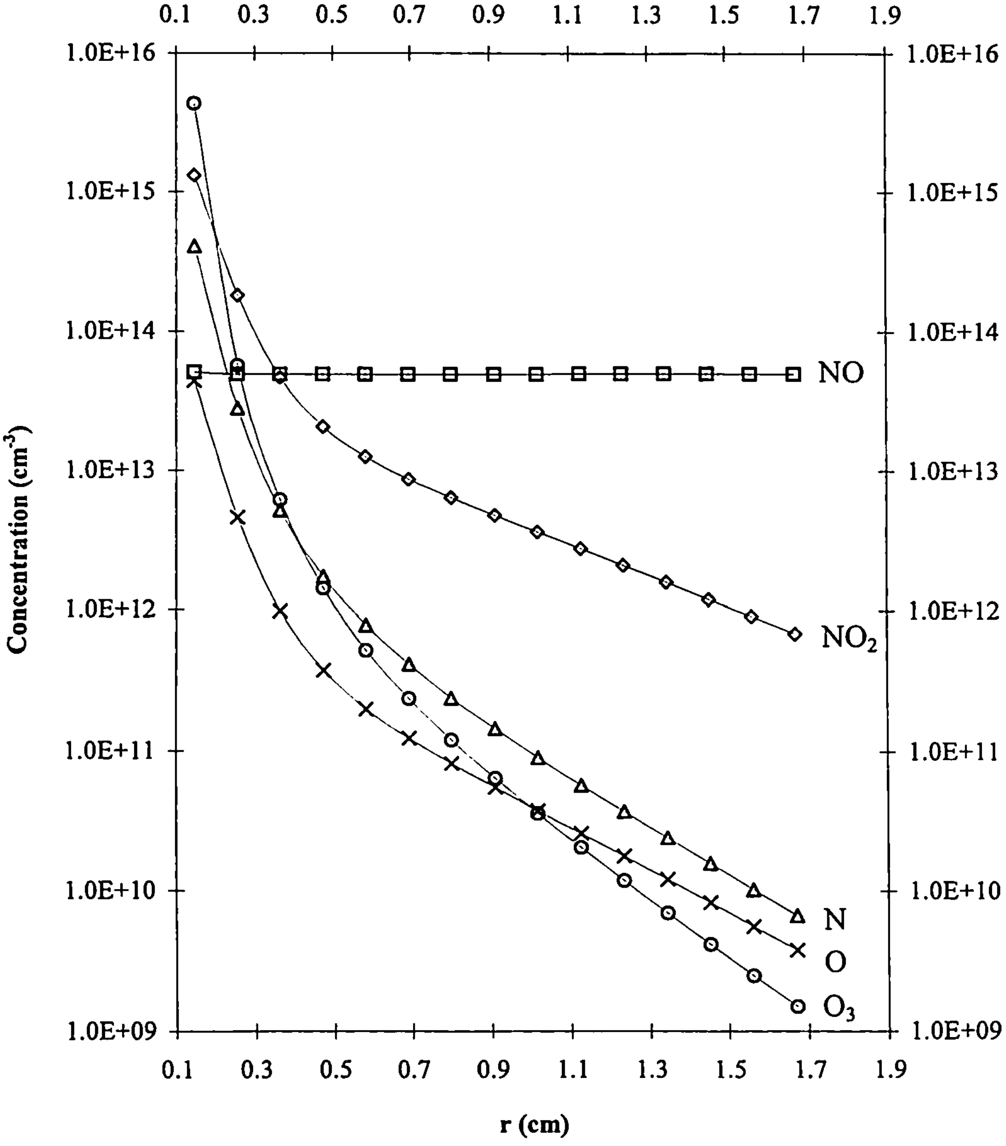

Figure 5.1.26: Radial lighter molecule radicals concentration profiles for a corona discharge at V = –17.0 kV and Q_g = 0 L/min in a 21% O_2–79% N_2 atmosphere

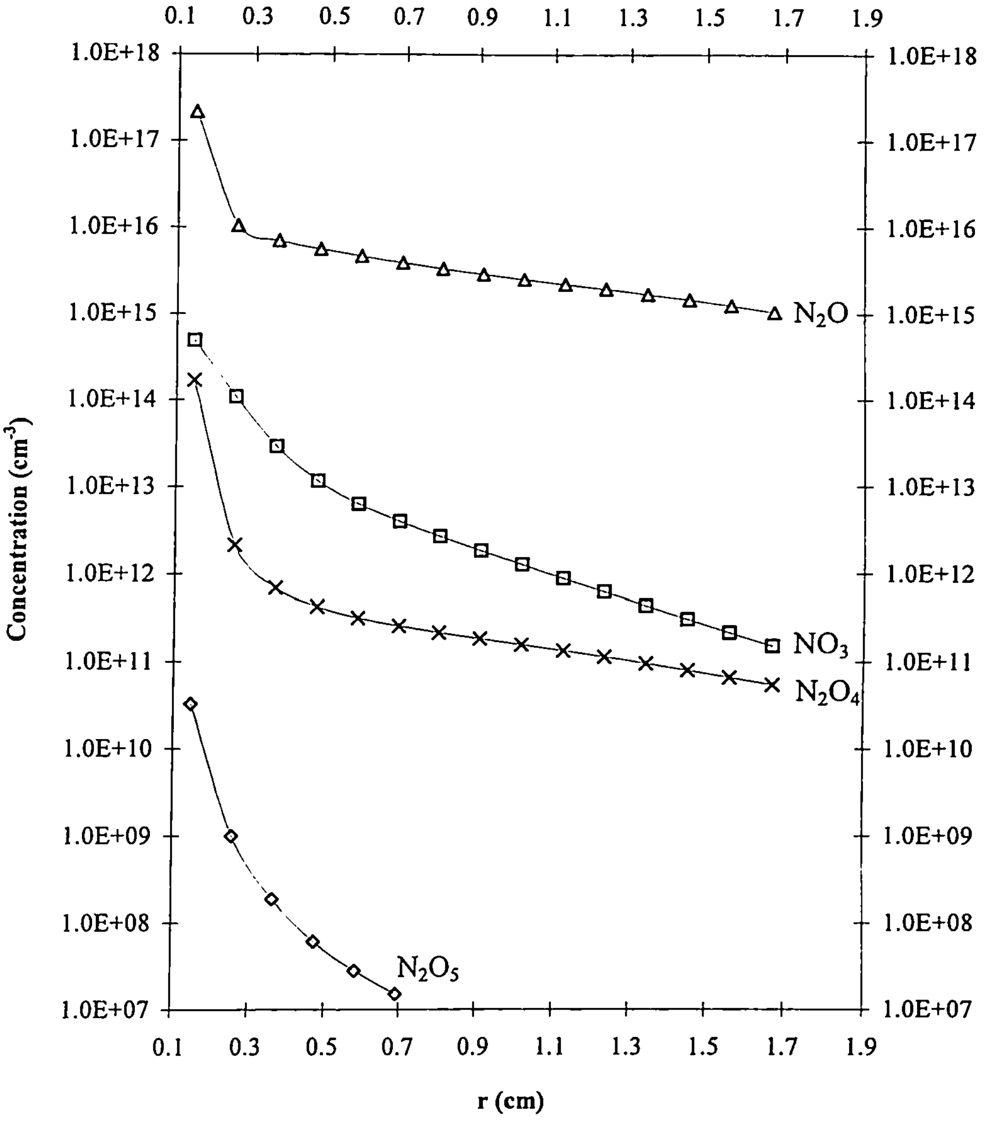

Figure 5.1.27: Radial heavier molecule radicals concentration profiles for a corona discharge at $V = -17.0$ kV and $Q_g = 0$ L/min in a 21% O_2–79% N_2 atmosphere

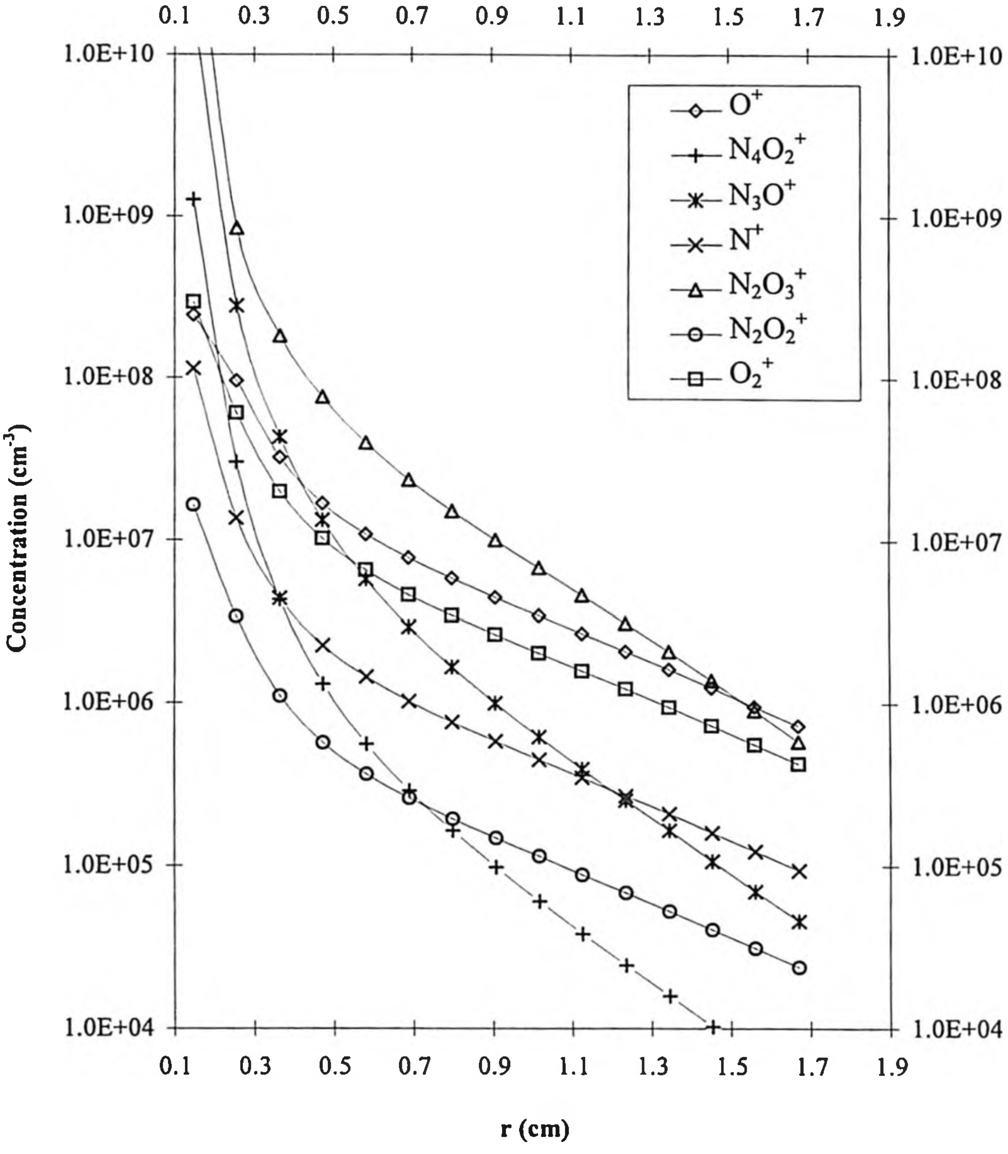

Figure 5.1.28: Radial positive ions concentration profiles for a corona discharge at V = –17.0 kV and Q_g = 0 L/min in a 21% O_2–79% N_2 atmosphere

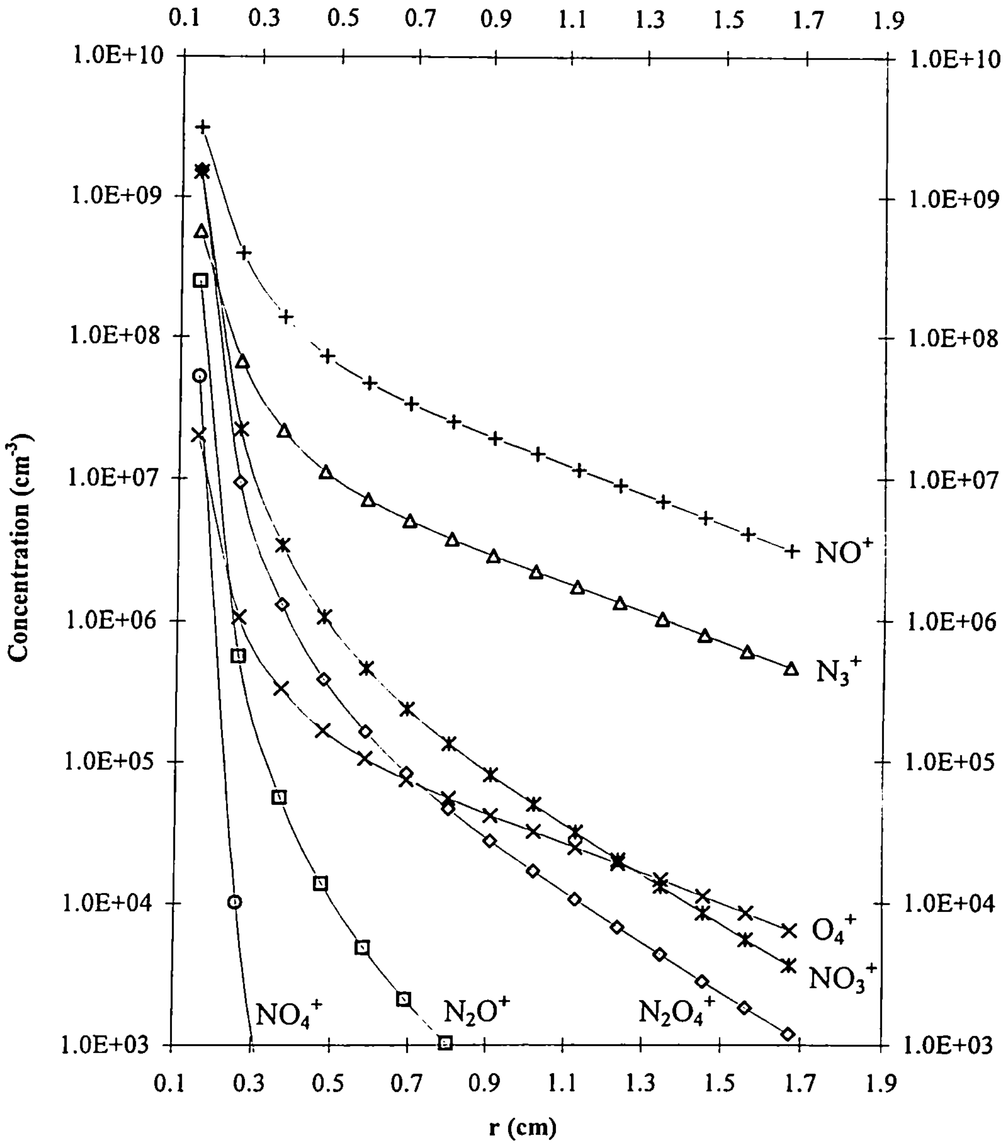

Figure 5.1.29: Radial positive ions concentration profiles for a corona discharge at V = –17.0 kV and Q_g = 0 L/min in a 21% O_2–79% N_2 atmosphere

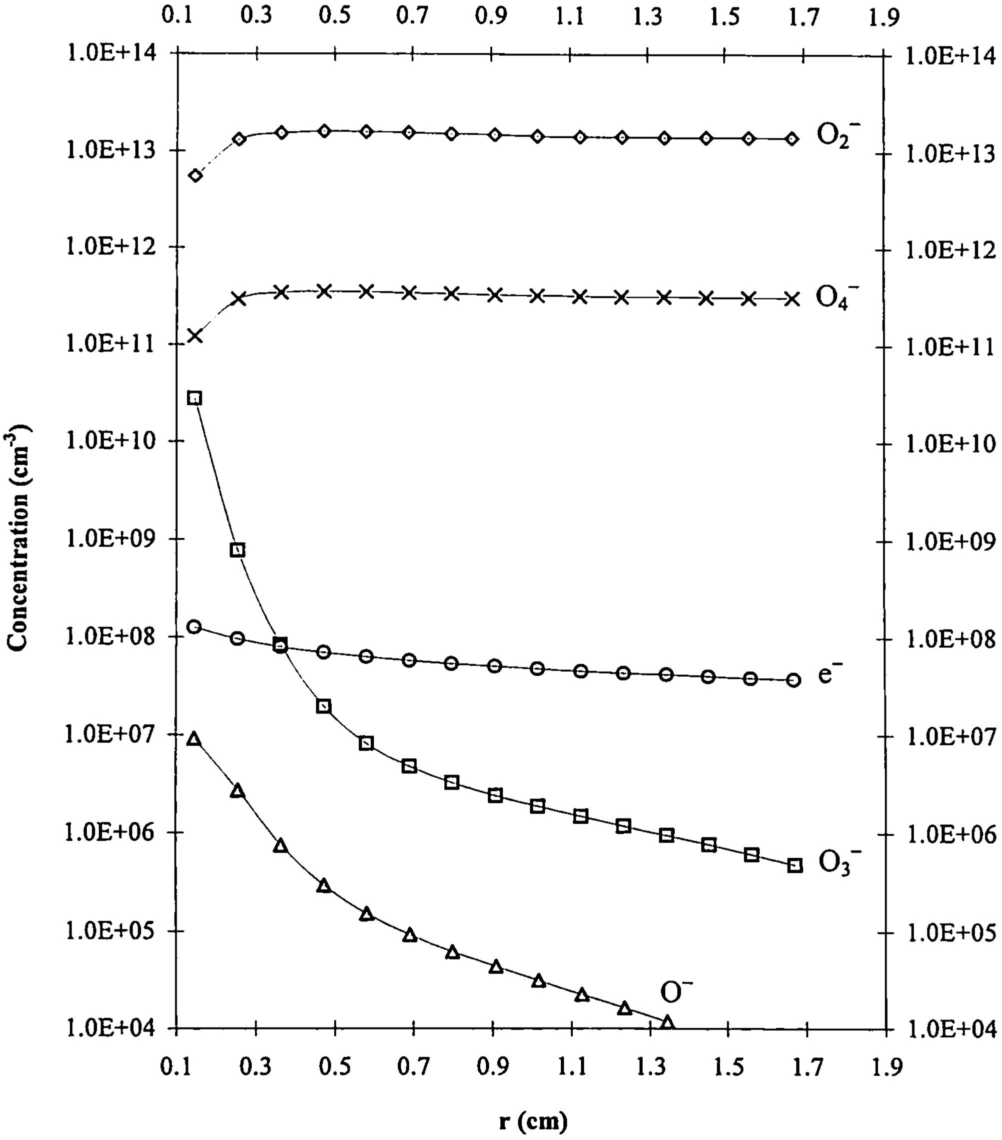

Figure 5.1.30: Radial electron and O_x^- negative ions concentration profiles for a corona discharge at $V = -20.0$ kV and $Q_g = 0$ L/min in a 21% O_2–79% N_2 atmosphere

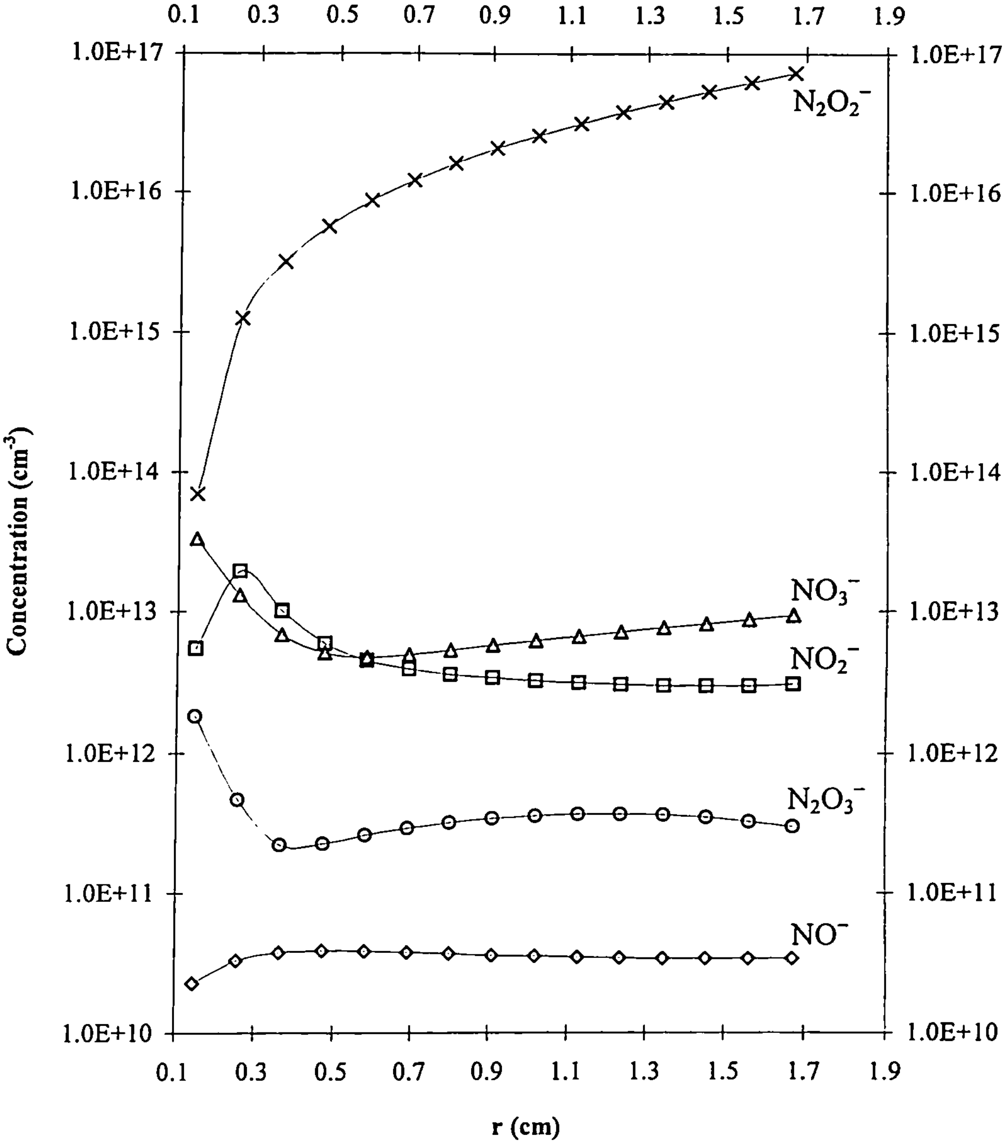

Figure 5.1.31: Radial $N_xO_y^-$ negative ions concentration profiles for a corona discharge at V = –20.0 kV and Q_g = 0 L/min in a 21% O_2–79% N_2 atmosphere

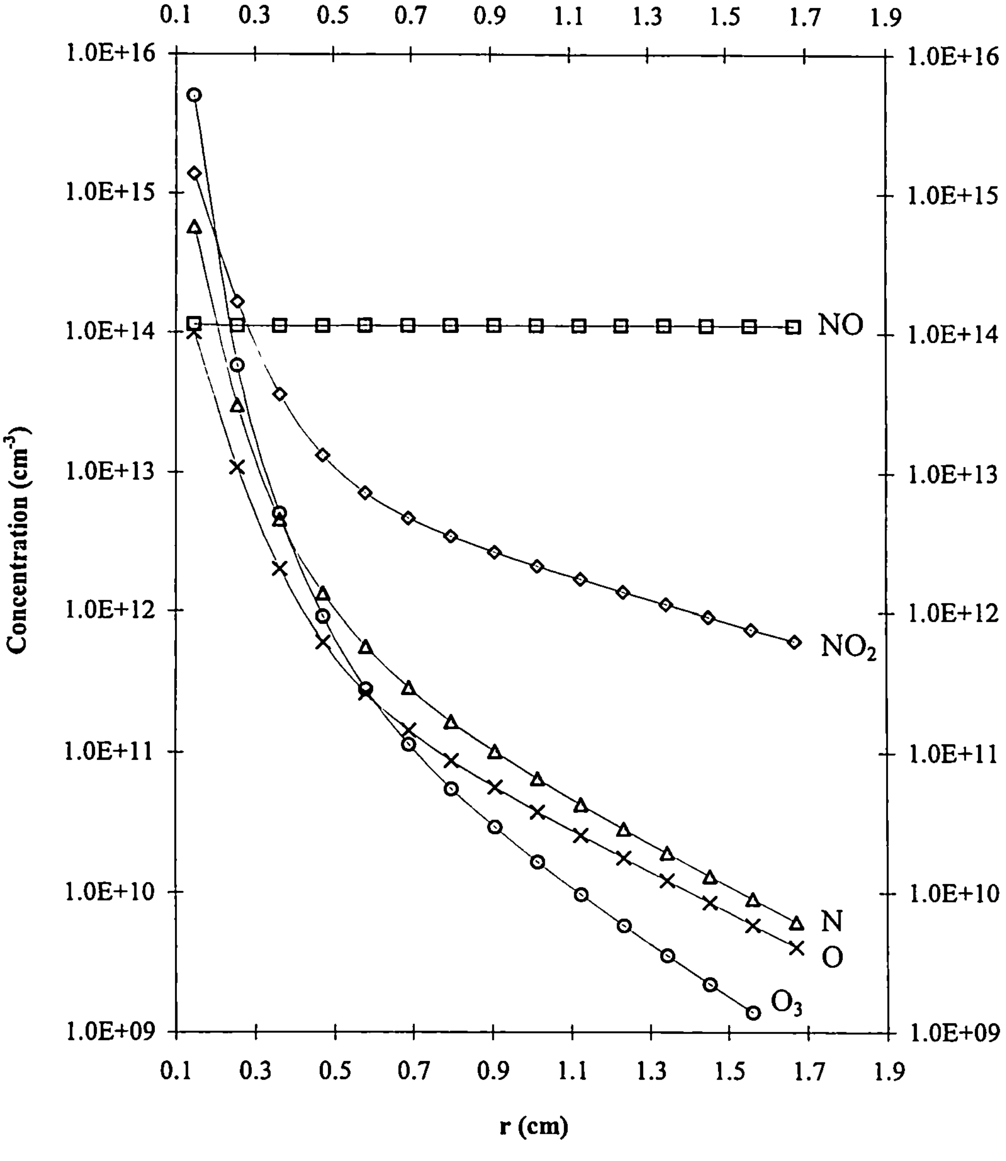

Figure 5.1.32: Radial lighter molecule radicals concentration profiles for a corona discharge at V = –20.0 kV and Q_g = 0 L/min in a 21% O_2–79% N_2 atmosphere

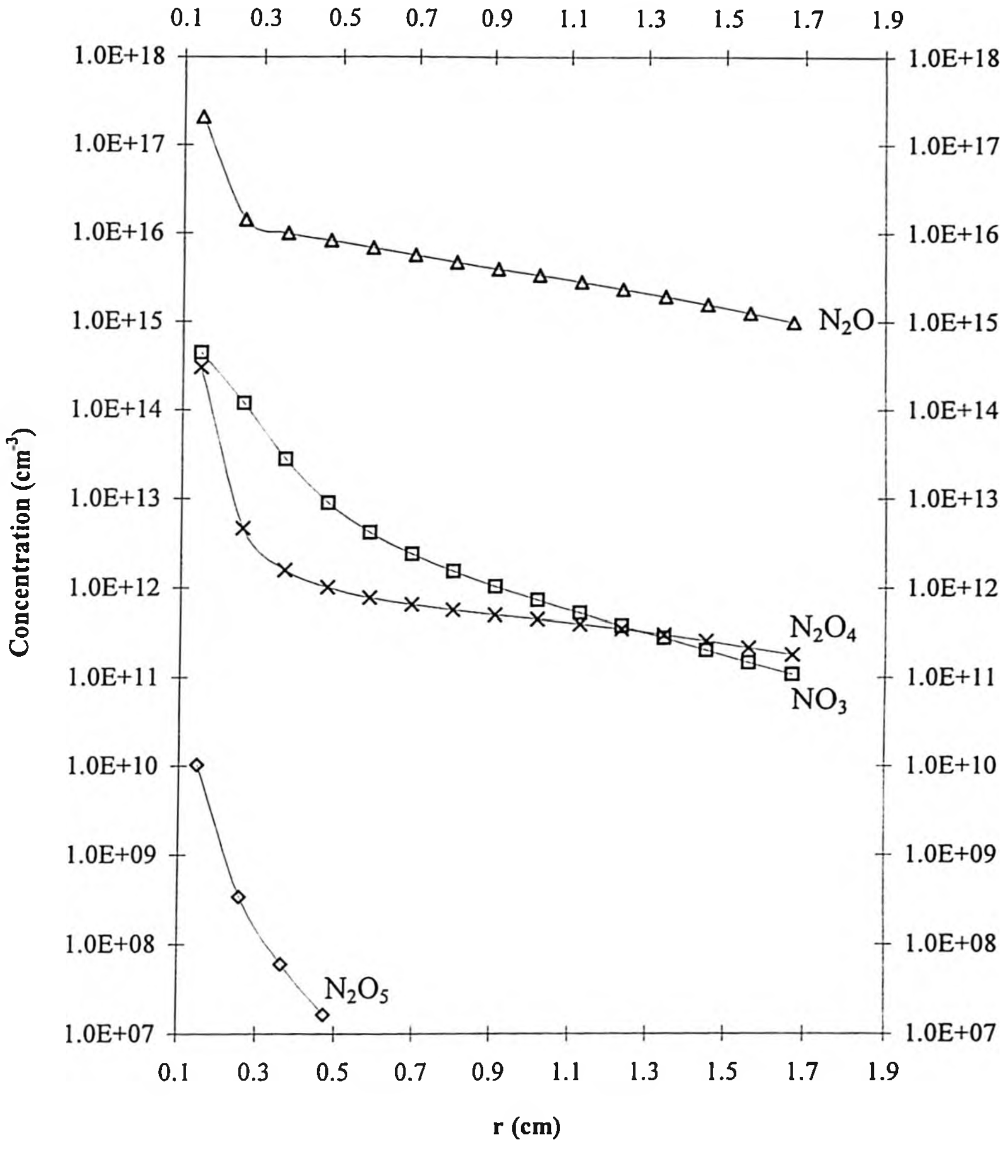

Figure 5.1.33: Radial heavier molecule radicals concentration profiles for a corona discharge at V = –20.0 kV and Q_g = 0 L/min in a 21% O_2–79% N_2 atmosphere

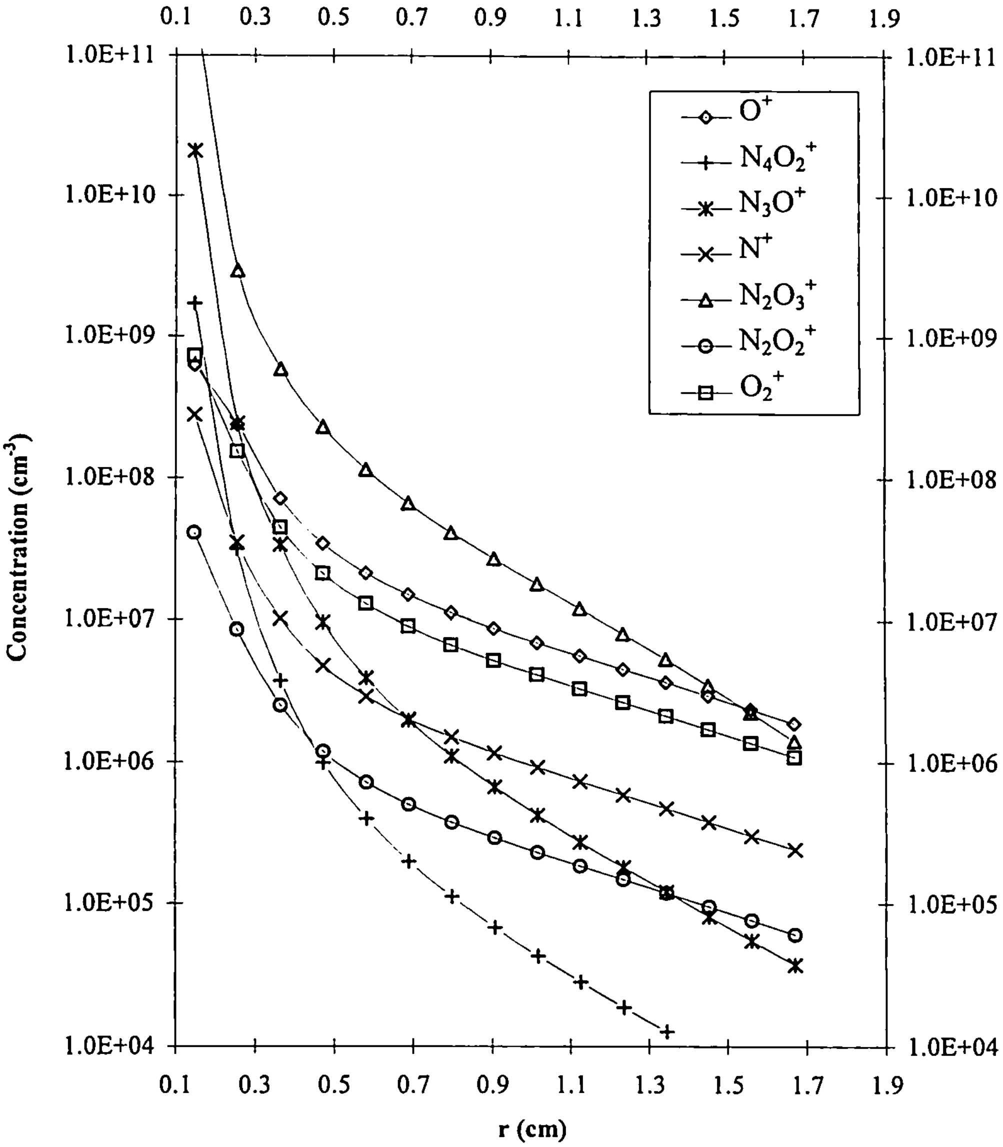

Figure 5.1.34: Radial positive ions concentration profiles for a corona discharge at V = –20.0 kV and Q_g = 0 L/min in a 21% O_2–79% N_2 atmosphere

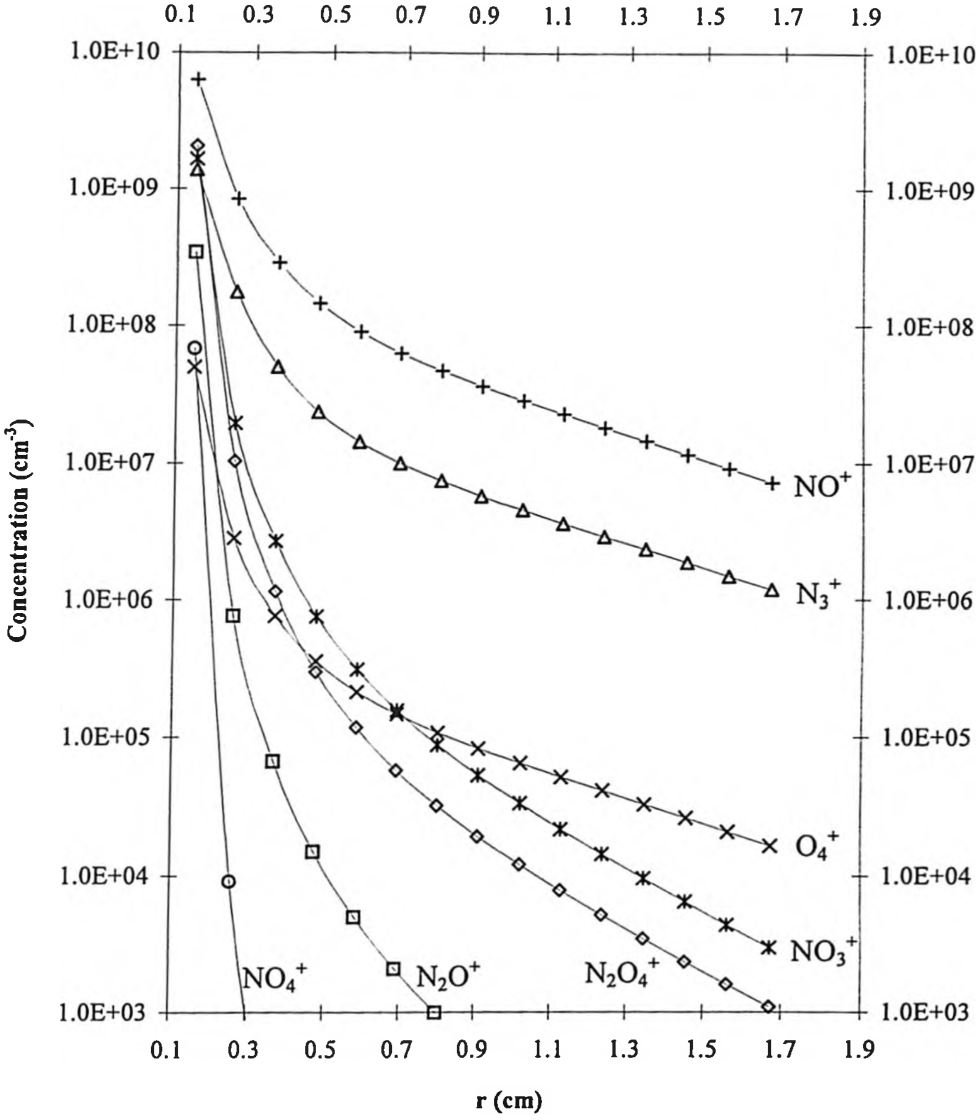

Figure 5.1.35: Radial positive ions concentration profiles for a corona discharge at V = –20.0 kV and Q_g = 0 L/min in a 21% O_2–79% N_2 atmosphere

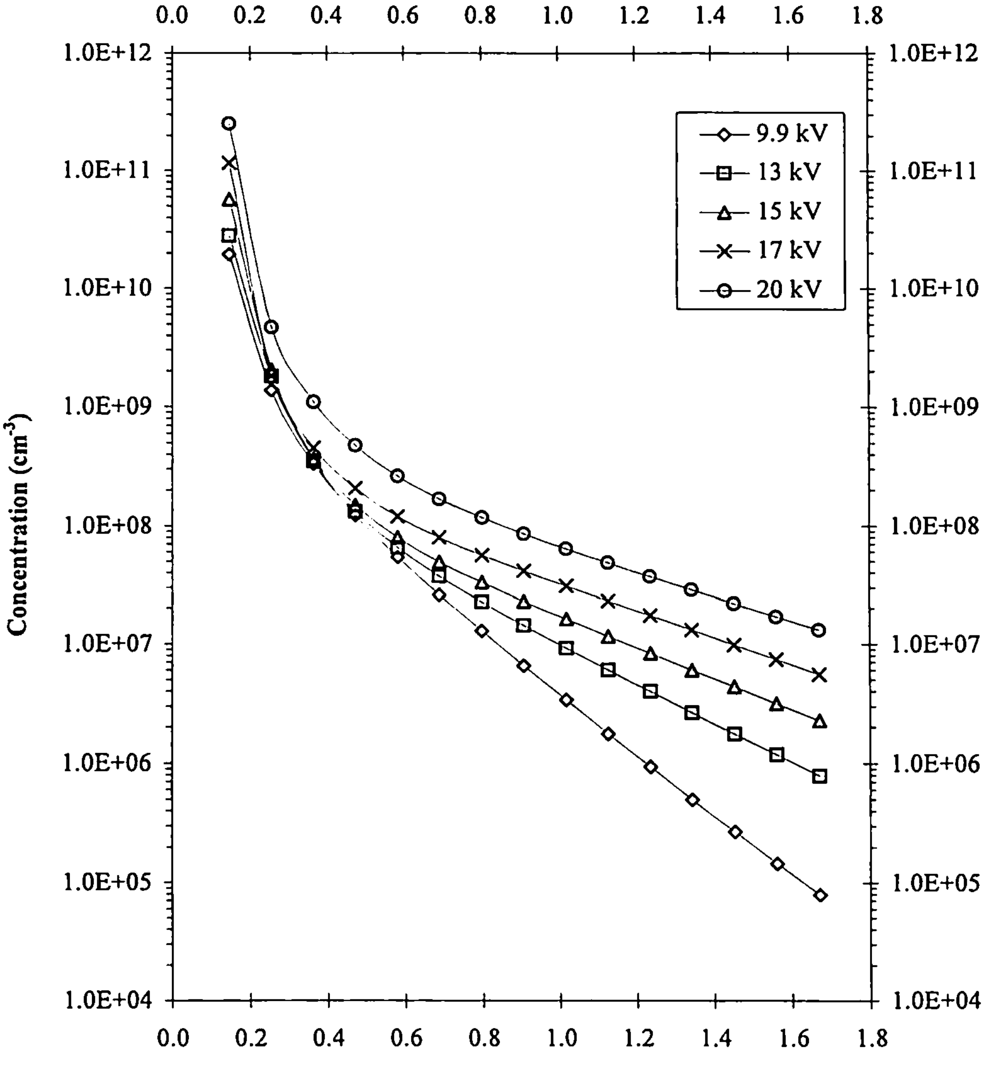

Figure 5.1.36: The effect of the applied voltage on the total positive ion density radial profiles

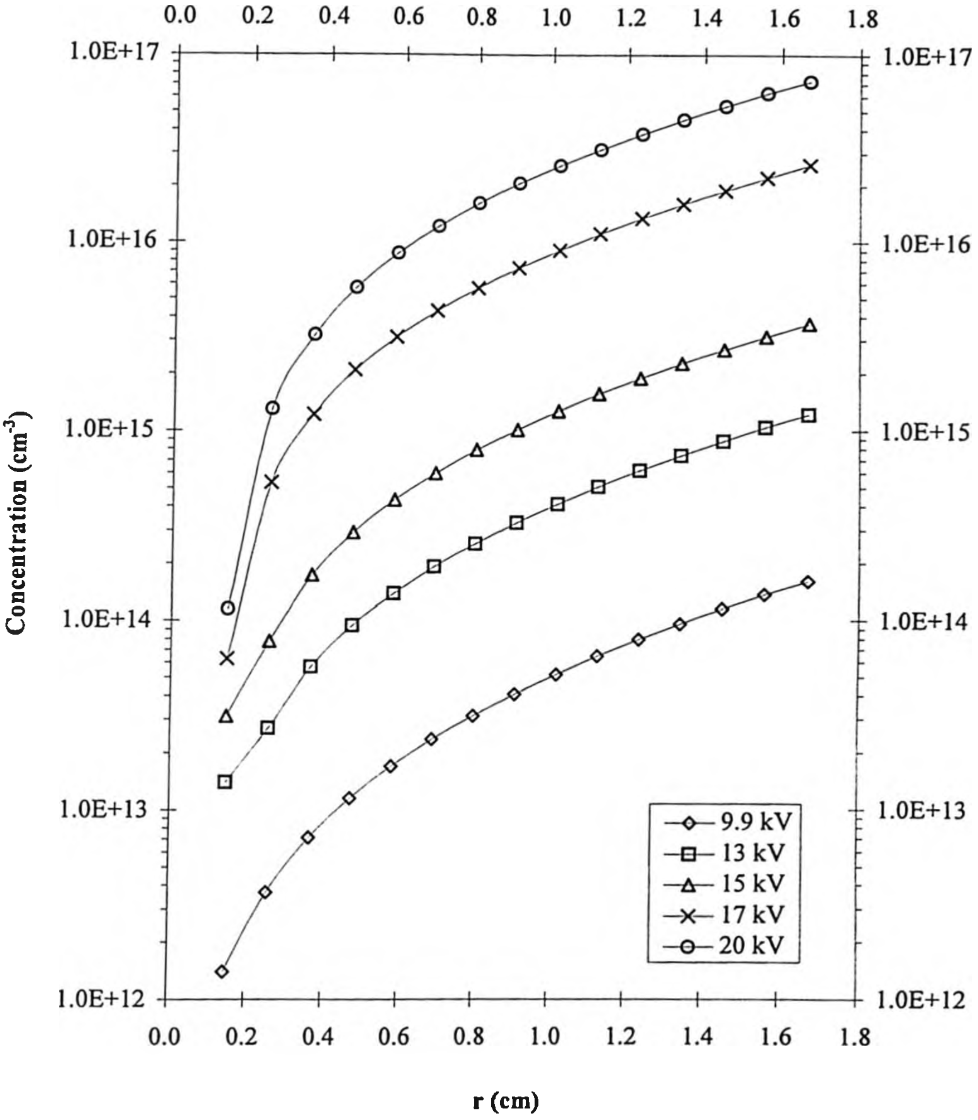

Figure 5.1.37: The effect of the applied voltage on the total negative ion density radial profiles

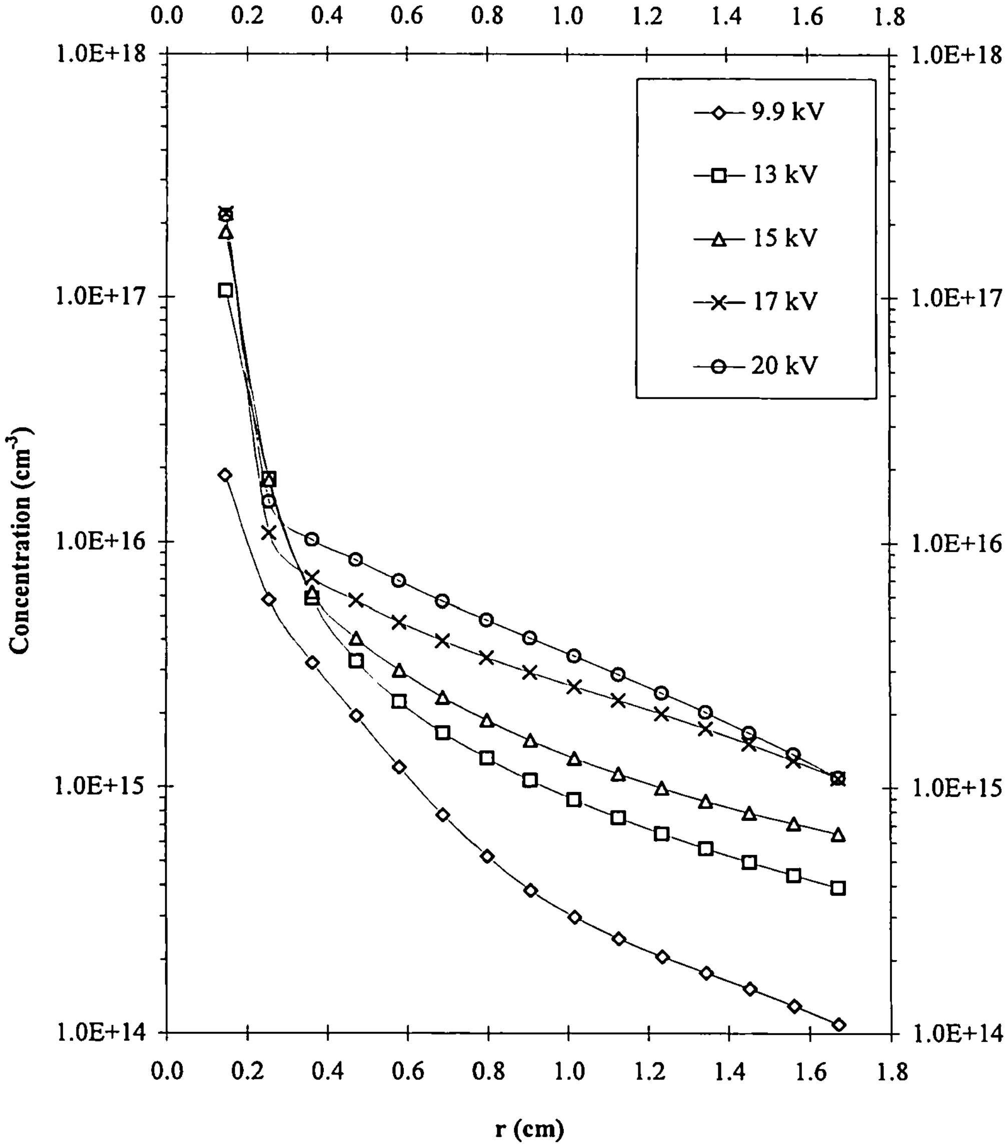

Figure 5.1.38: The effect of the applied voltage on the total neutral radical density radial profiles

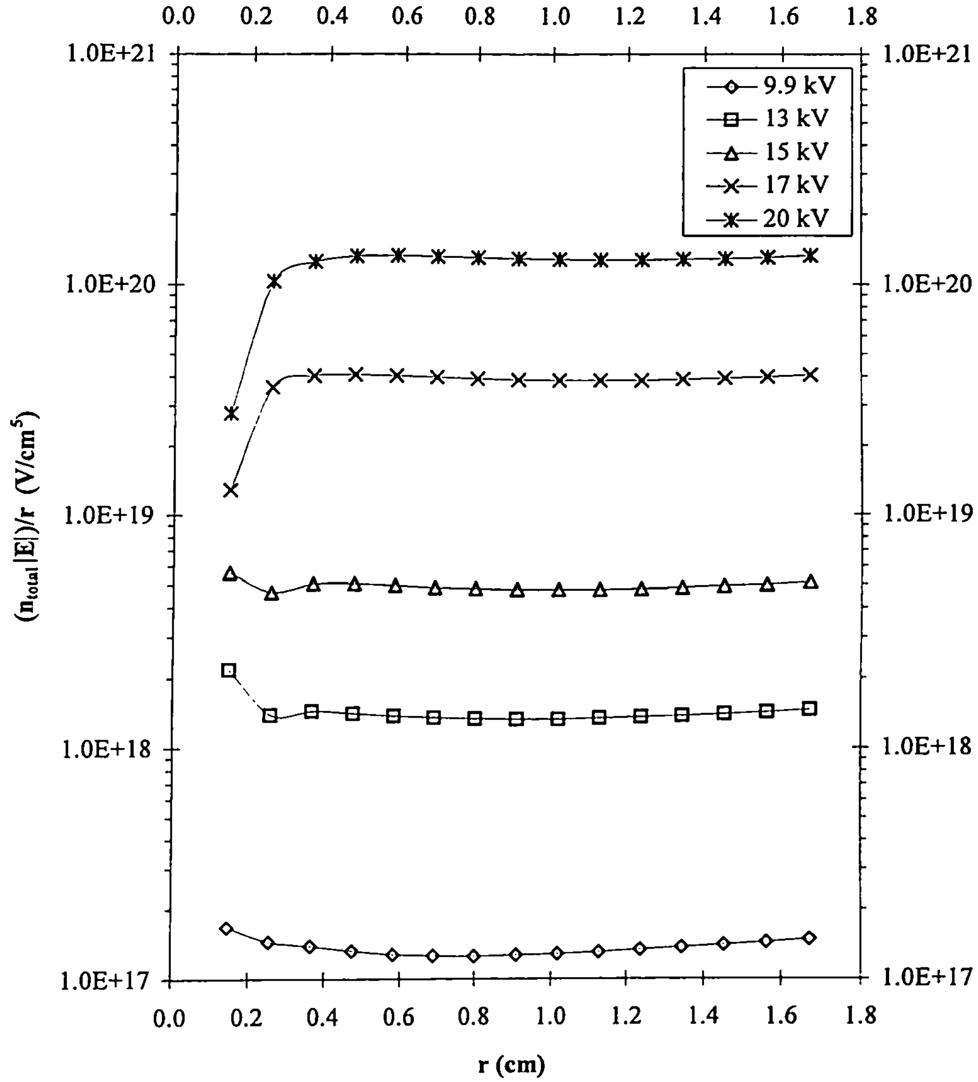

Figure 5.1.39: The effect of the applied voltage on the current density radial profiles

5.2. Effect of Gas Flow Rate

To study the effect of the gas flow rate on the 36 trace chemical compositions, four different flow rate at an applied voltage of −18.0 kV are simulated. These flow rates are: 0.0 L/min, 0.5 L/min, 1.0 L/min and 1.5 L/min, which correspond to an average velocity of 0.00 cm/s, 0.84 cm/s, 1.68 cm/s and 2.51 cm/s respectively. Due to these small velocity values, the effect of the gas convective transport term in the transport equations may be neglected (Section 4.2). The magnitude of the corresponding time averaged discharged currents for these four gas flow rate are: 1.8 mA, 2.0 mA, 2.2 mA and 2.4 mA as shown in Figure 3.2.2.

As mentioned in Section 3.2, an increase in gas flow rate tends to enhance the current density during a corona discharge up to a certain level, hence it may lead to a change in the radial electric field profile computed (Equation 4.2.22). The effect of the gas flow rate on the radial electric field profiles is shown in Figure 5.2.1. This figure show that the electric field is largest near the corona wire, and decreases as the radial distance increases. This observations are similar to the applied voltage effect as discussed in Section 5.1. However, the gas flow rate seems to have no significant effect on the electric field profiles as shown in Figure 5.2.1. This is expected since the low gas flow rate utilized in the present model have very small effects on the time averaged discharge current. The reason for not plotting the other two gas flow rates (0.5 L/min and 1.0 L/min) in this figure is because the data points are right on top of each other.

The results for the electron density profiles are shown in Figure 5.2.2. This figure shown that the electron density is largest near the corona wire, and decreases as the radial distance increases. This is comparable to the result show in Section 5.1. Another observation is that an increase in gas flow rate increases the electron density as expected due the time averaged discharge current dependence on the gas flow rate. However, the increase is small when compared to the applied voltage effect.

The effect of the gas flow rate on the radial electron temperature profiles is show in Figure 5.2.3. The result is similar to the electric field calculation. The temperature tends to be the largest near the corona wire and decreases as the radial distance increases. Also, the gas flow rate has no significant effect on the radial electron temperature profiles.

Since an increase in gas flow rate have only small effect on the electron density, the divergence of the ion density ($\nabla \cdot n_k$) and the Laplacian of the particle density ($\nabla^2 n_k$) is not plotted for this set of data. It is because these values are approximated using the radial electron density profiles (Equation 4.2.1 and 4.2.2). Therefore, a small change in electron density profiles will only lead to a small change in the results.

The effects of the gas flow rates on the radical, negative ion and positive ion concentrations are shown in Figures 5.2.4 to 5.2.27. Again, no significant amount of O_6^+, NO_2^+, N_2^+, and N_4^+ are observed. These positive ions have a concentration below 1.0 cm^{-3} for all radial position, except for N_2^+ and N_4^+ near the corona wire. Near the corona wire, the concentration of the N_2^+ increases from 3.27×10^3 cm^{-3} to 4.48×10^3 cm^{-3} as the gas flow increases from 0.0 L/min to 1.5 L/min, while the concentration of the N_4^+ increases from 6.59×10^3 cm^{-3} to 9.01×10^3 cm^{-3}.

Another observation from Figures 5.2.4 to 5.2.27 is that the concentrations of the neutral species are generally higher than the concentrations of the negative ions, which in term are generally higher than the concentrations of the positive ions. One may also observed that the concentrations for some of the negative ions tends to increase ($N_2O_2^-$) or remain constant (O_2^- and O_4^-) as the radial distance increases, while the concentrations for the neutral radicals (except NO) and positive ions tends to decrease as the radial distance increases. This is similar to the results show in Section 5.1. Under these gas flow rate ranges, the negative ion with the highest concentration is $N_2O_2^-$. The neutral radical with the highest concentration is N_2O, and the positive ion with the highest concentration is NO^+. These results are also consistent with the results for the higher applied voltage show in Section 5.1.

The effect of the gas flow rate on the total positive ion, negative ion and radical concentration radial profiles are show in Figures 5.2.28, 5.2.29 and 5.2.30 respectively. From these figures, one can observed that the gas flow rate has no significant effect on the total concentrations of the positive ions and neutral radicals when compared to the applied voltage results. However, a small increase (relative to the applied voltage effect) in the total density of the negative ions as the flow rate increases is shown in Figure 5.2.29.

The total concentration of the negative ions (Figure 5.2.29) multiplied by the magnitude of the electric field and then divided by the radial position are shown in Figure 5.2.31. This figure shows that the current density increases with increasing gas flow rate, and is approximately constant for all radial positions except near the corona wire. These results are also similar to the results discussed in Section 5.1.

Since the total concentrations for the negative ions are much greater than the total concentrations for the positive ions, the current densities for the different gas flow rates can be estimated from the linear portion of Figure 5.2.31 (by neglecting the concentrations of the positive ions). Here, the ion mobility of all the negative ions is assume to be approximately equals to the ion mobility of the $N_2O_2^-$. This assumption should be valid since the concentration of $N_2O_2^-$ dominates the total concentrations of the negative ions for the bigger radial positions (linear portion of Figure 5.2.31). The calculated current densities are:

2.2 A/cm^3, 3.0 A/cm^3, 3.7 A/cm^3, and 4.8 A/cm^3 for the gas flow rate of 0.0 L/min, 0.5 L/min, 1.0 L/min and 1.5 L/min respectively. From these results, one can realized that the current density increases by about a factor of 2 as the gas flow is increase by about a factor of 3 (to 4). (Since a gas flow rate of 1.5 L/min and 2.0 L/min generated the same discharge current for this applied voltage as stated in Section 3.2.) From these results, one may concluded that the effect of the gas flow rate on the current density is relatively small when compared with the applied voltage effect for the present conditions.

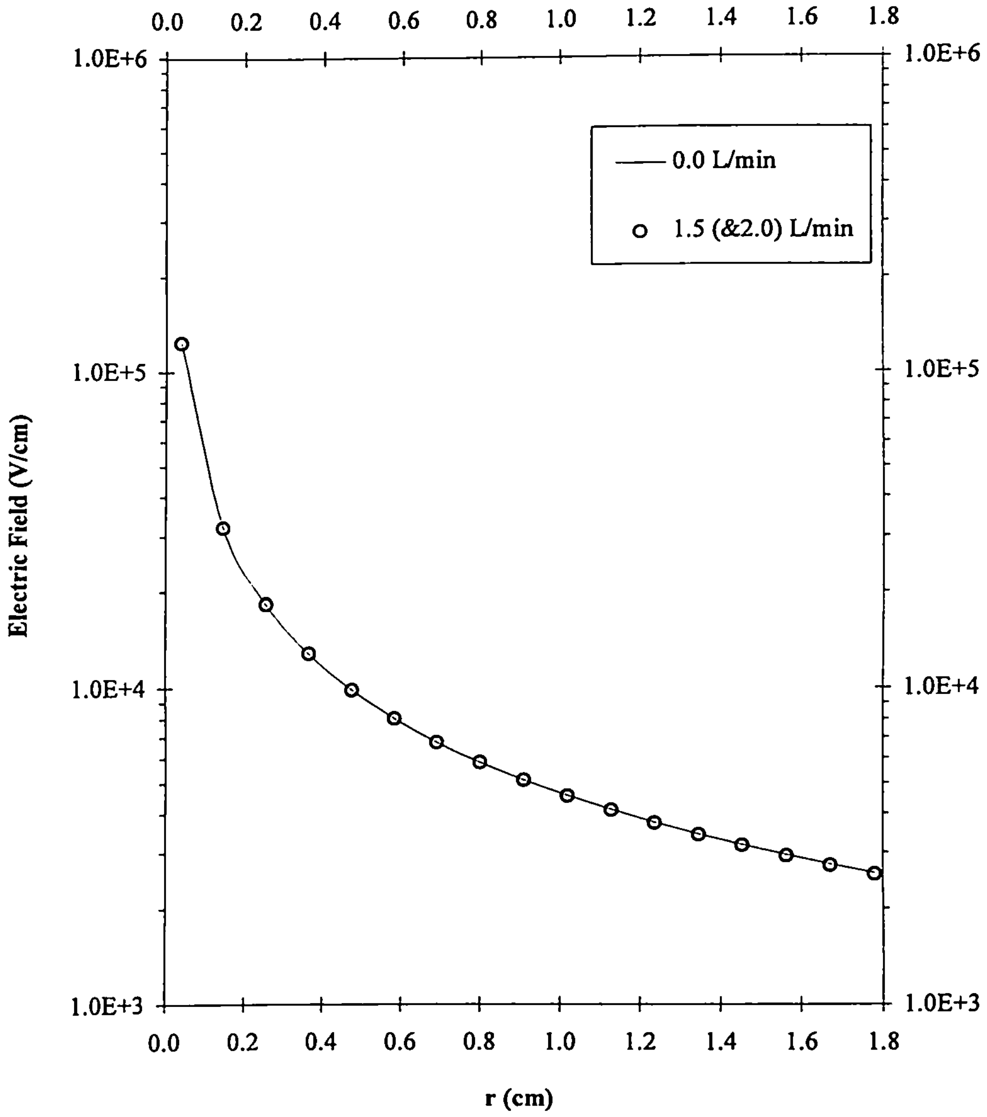

Figure 5.2.1: The effect of the gas flow rate on the radial electric field profiles at V = –18.0 kV for various gas flow rate

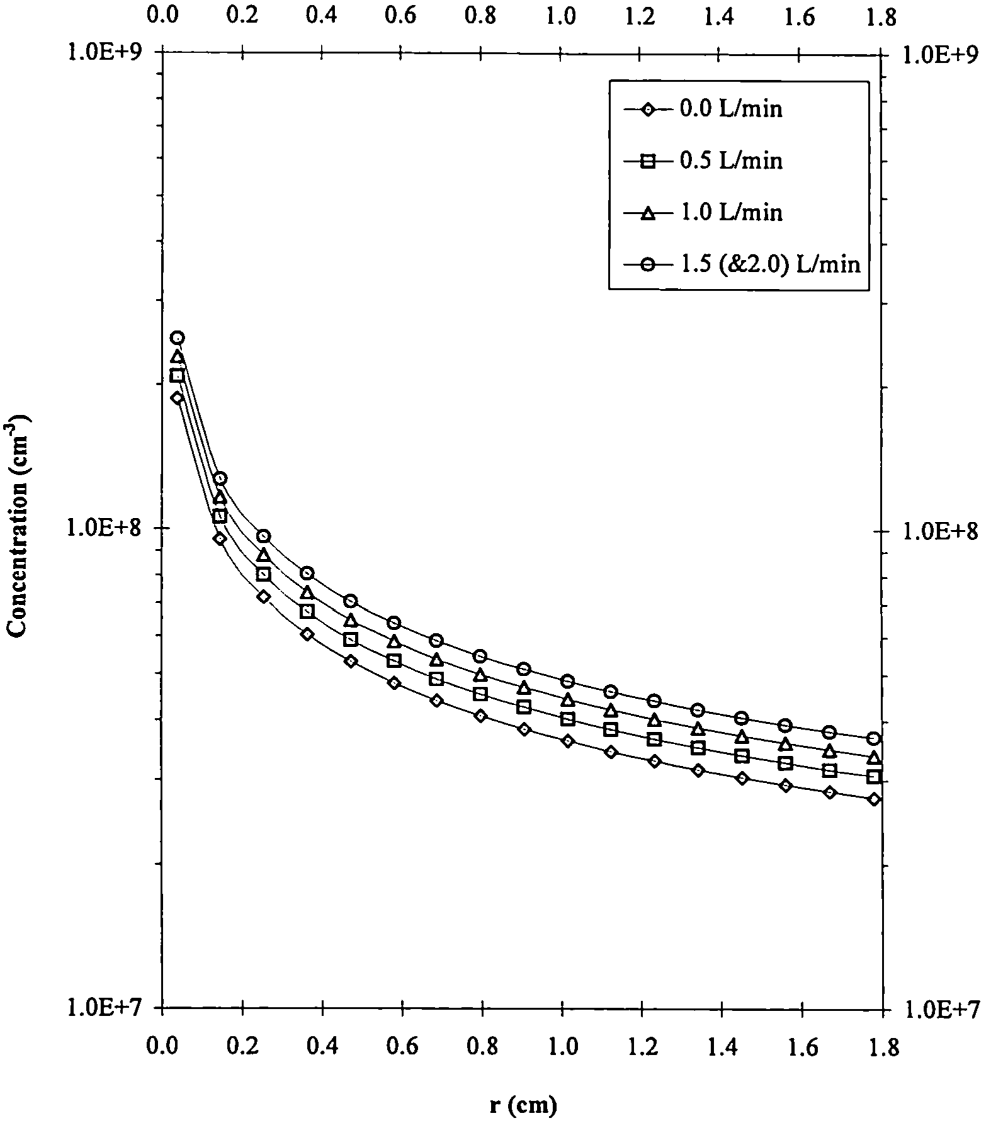

Figure 5.2.2: The effect of the gas flow rate on the radial electron density profiles for various gas flow rate at V = –18.0 kV

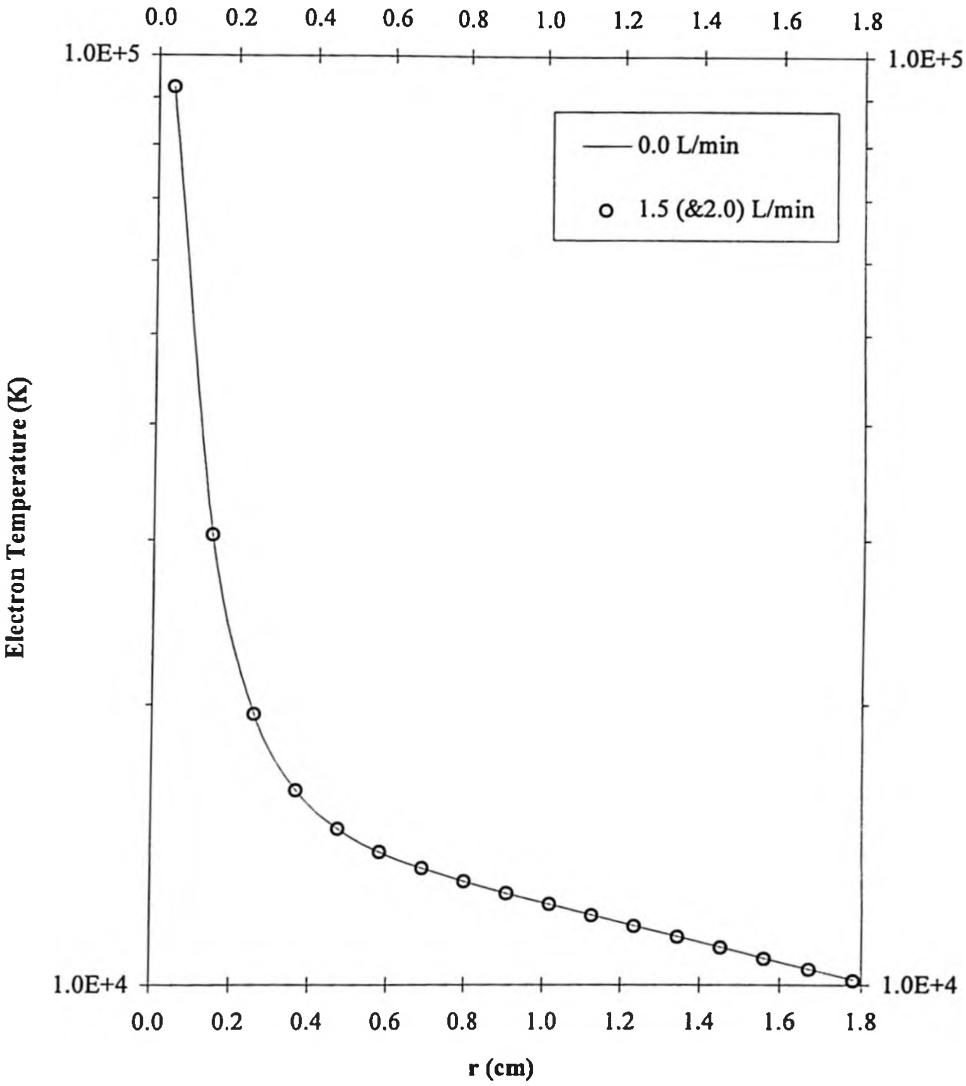

Figure 5.2.3: The effect of the gas flow rate on the radial electron temperature profiles for various gas flow rate at V = –18.0 kV

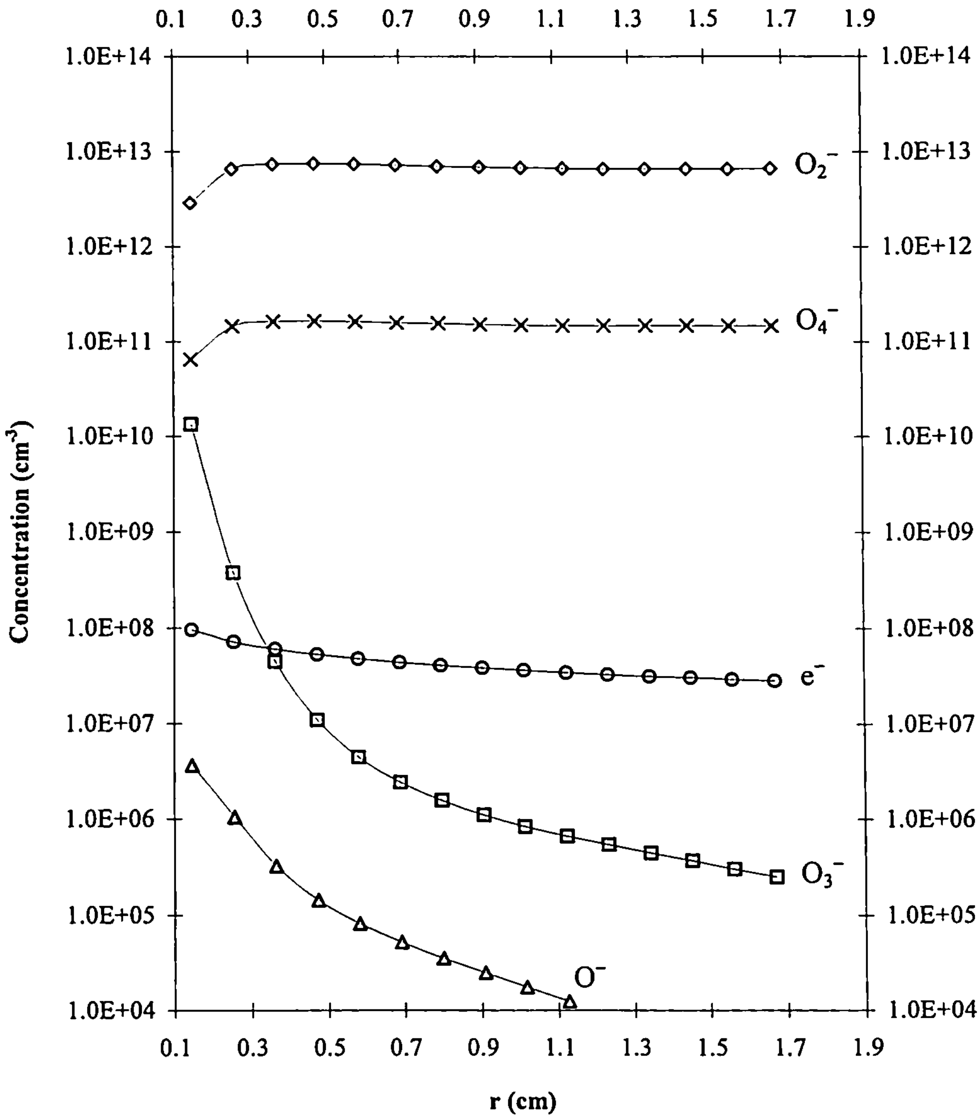

Figure 5.2.4: Radial electron and O_x^- negative ions concentration profiles for a corona discharge at V = –18.0 kV and Q_g = 0.0 L/min in a 21% O_2–79% N_2 atmosphere

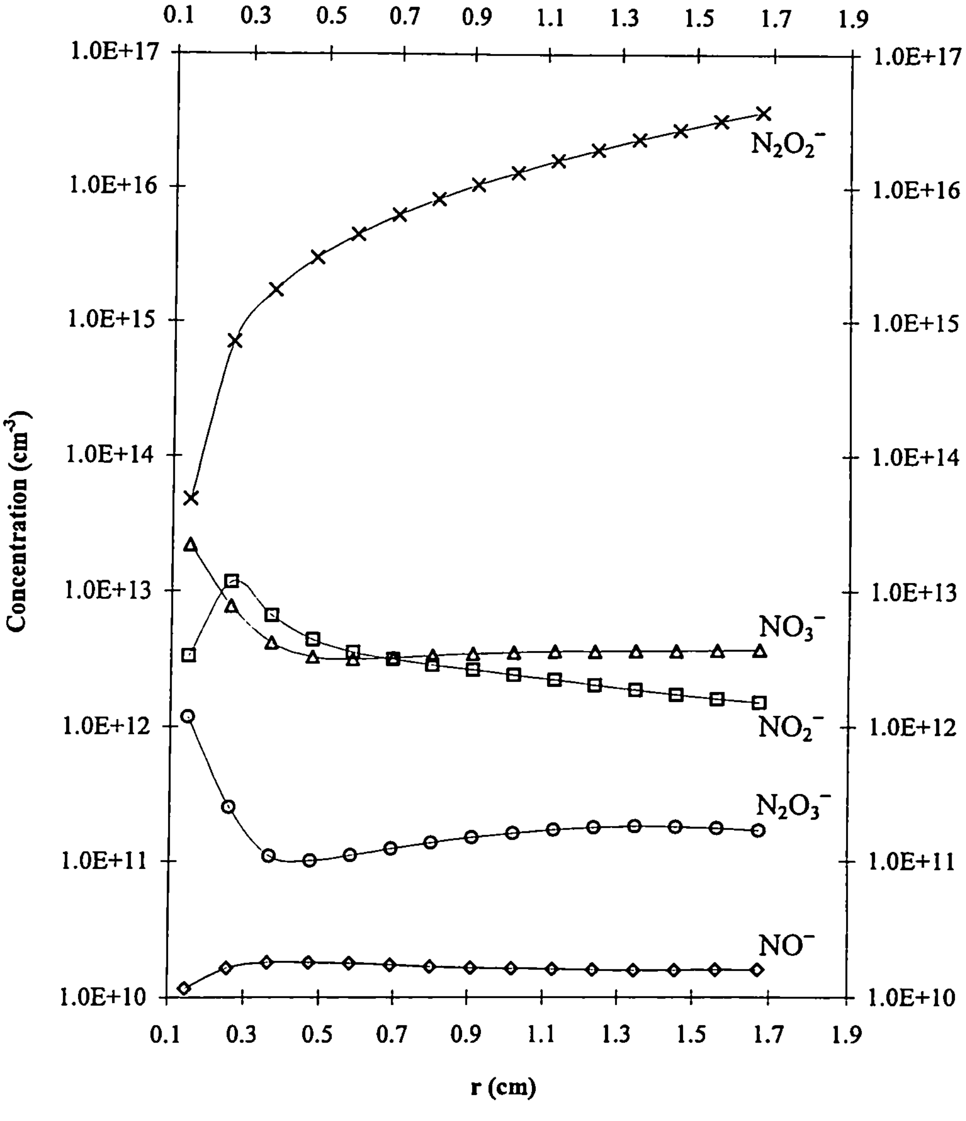

Figure 5.2.5: Radial $N_xO_y^-$ negative ions concentration profiles for a corona discharge at V = –18.0 kV and Q_g = 0.0 L/min in a 21% O_2–79% N_2 atmosphere

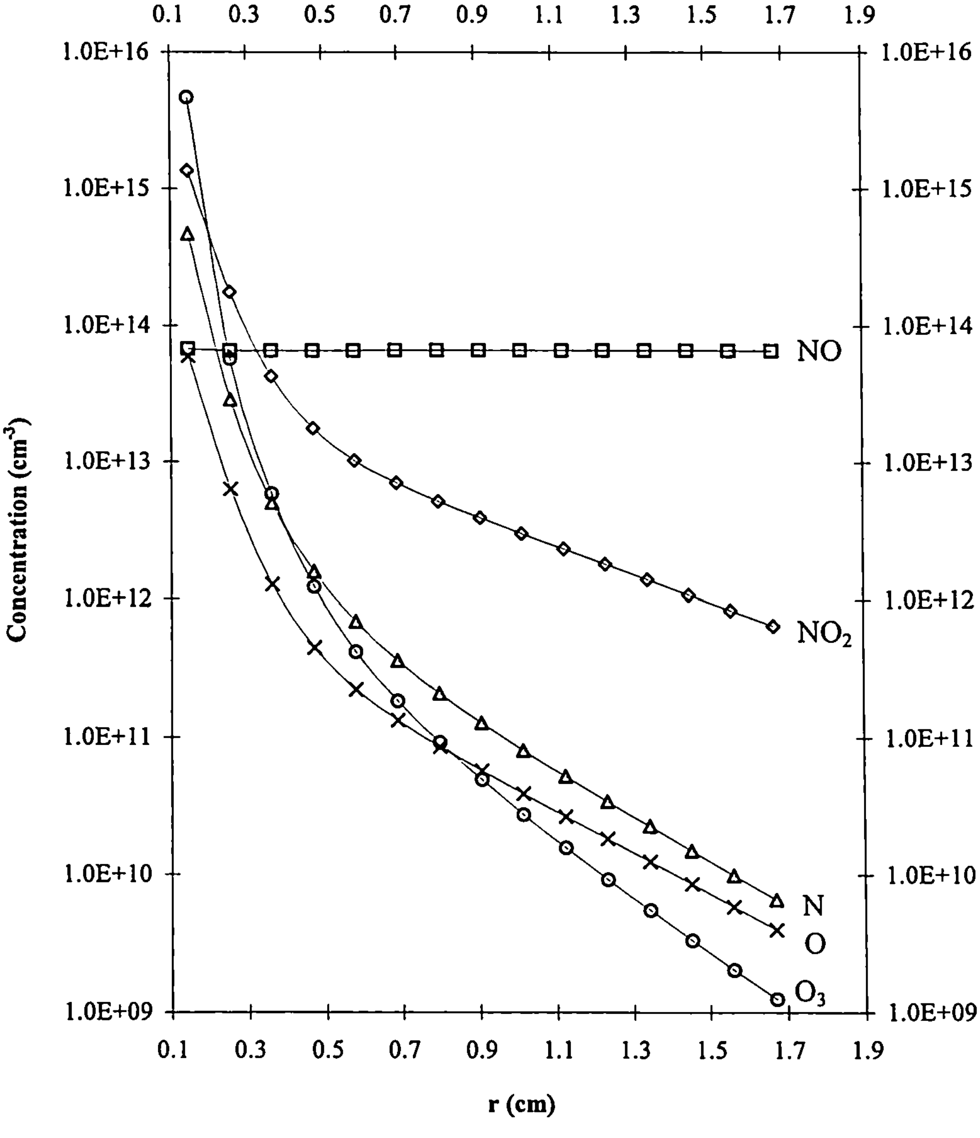

Figure 5.2.6: Radial lighter molecule radicals concentration profiles for a corona discharge at V = –18.0 kV and Q_g = 0.0 L/min in a 21% O_2–79% N_2 atmosphere

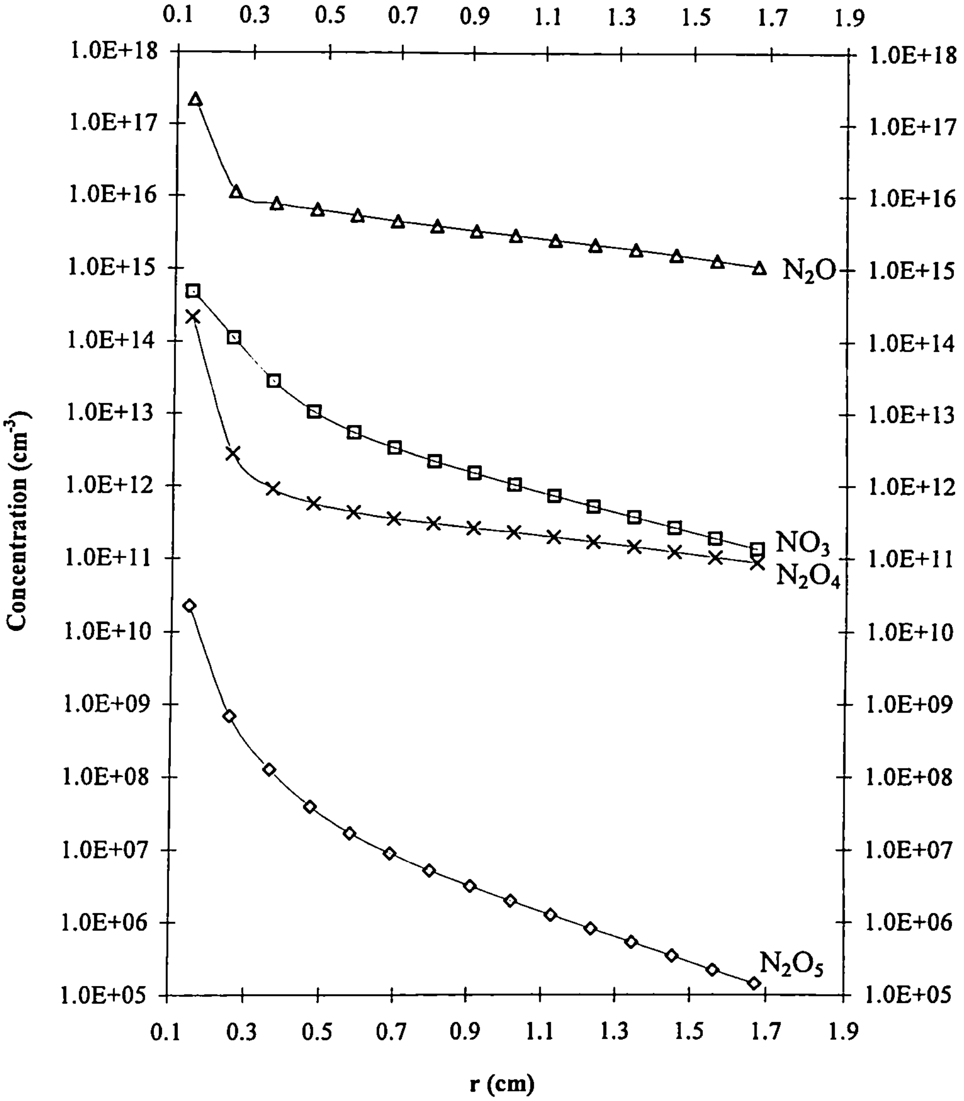

Figure 5.2.7: Radial heavier molecule radicals concentration profiles for a corona discharge at V = –18.0 kV and Q_g = 0.0 L/min in a 21% O_2–79% N_2 atmosphere

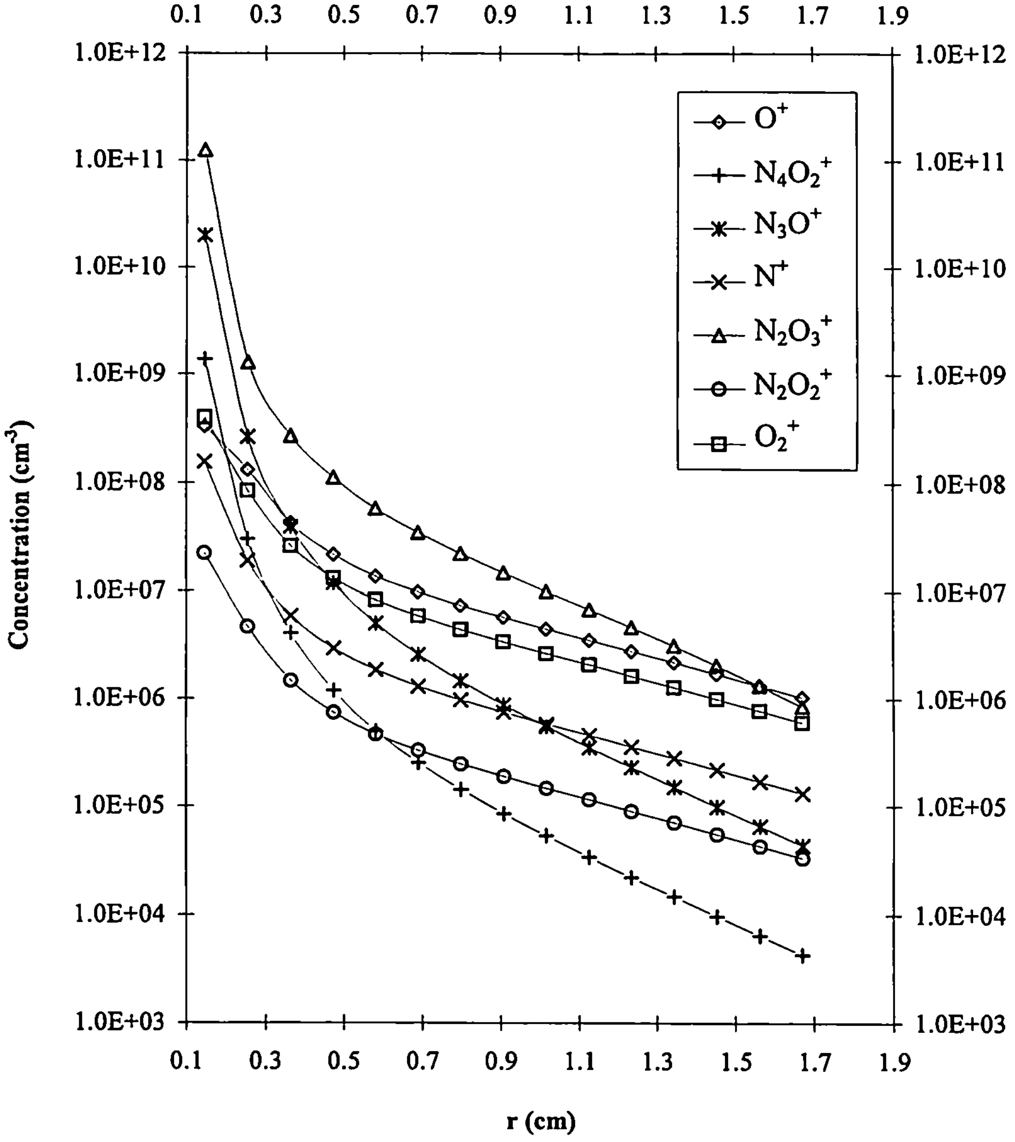

Figure 5.2.8: Radial positive ions concentration profiles for a corona discharge at V = –18.0 kV and Q_g = 0.0 L/min in a 21% O_2–79% N_2 atmosphere

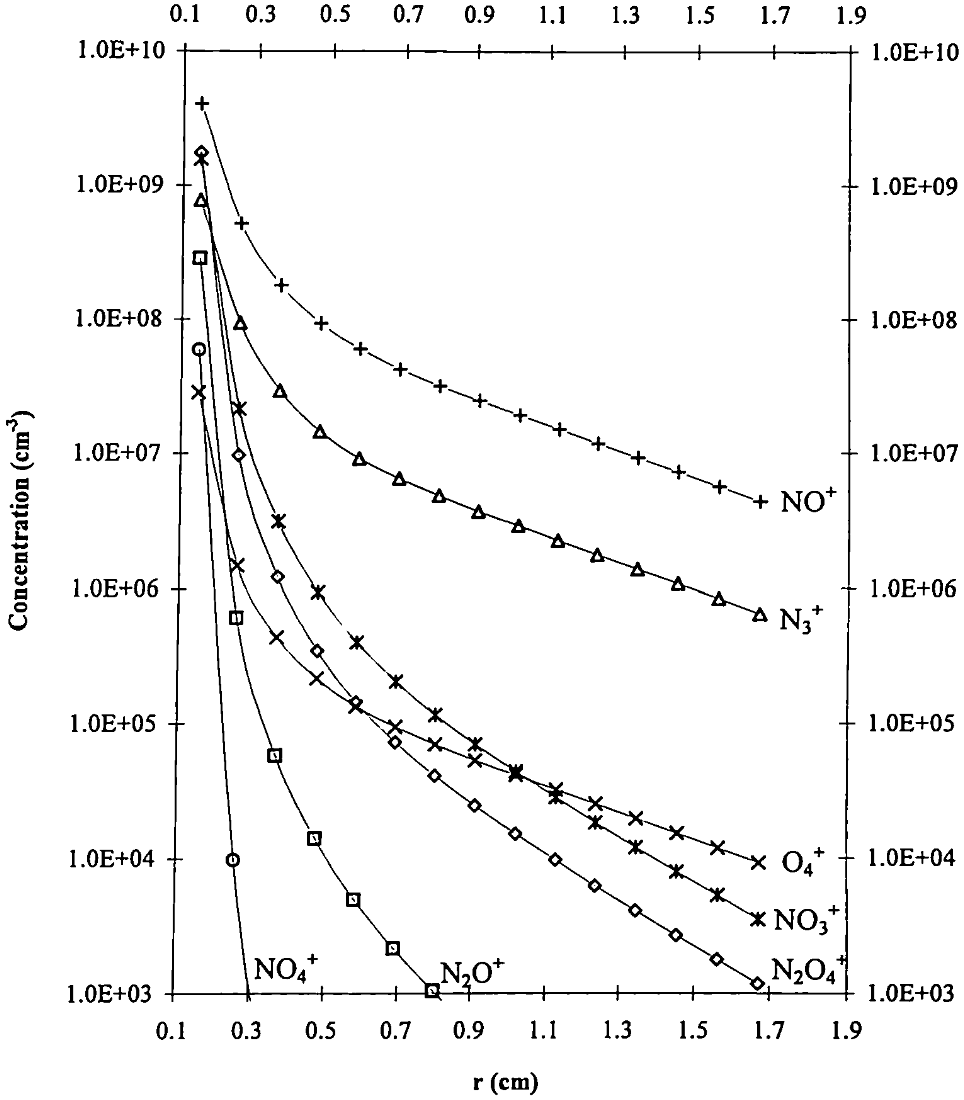

Figure 5.2.9: Radial positive ions concentration profiles for a corona discharge at V = –18.0 kV and Q_g = 0.0 L/min in a 21% O_2–79% N_2 atmosphere

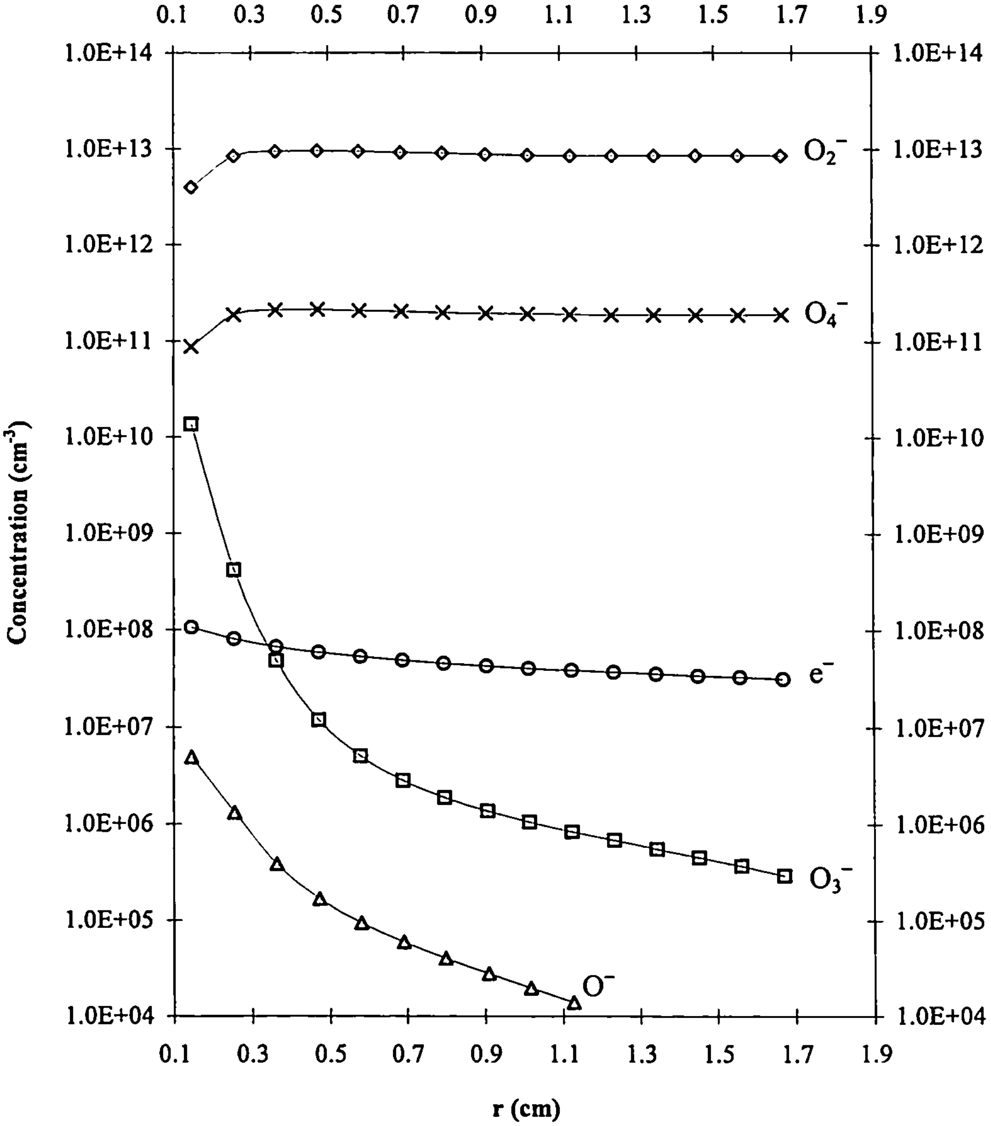

Figure 5.2.10: Radial electron and O_x^- negative ions concentration profiles for a corona discharge at V = –18.0 kV and Q_g = 0.5 L/min in a 21% O_2–79% N_2 atmosphere

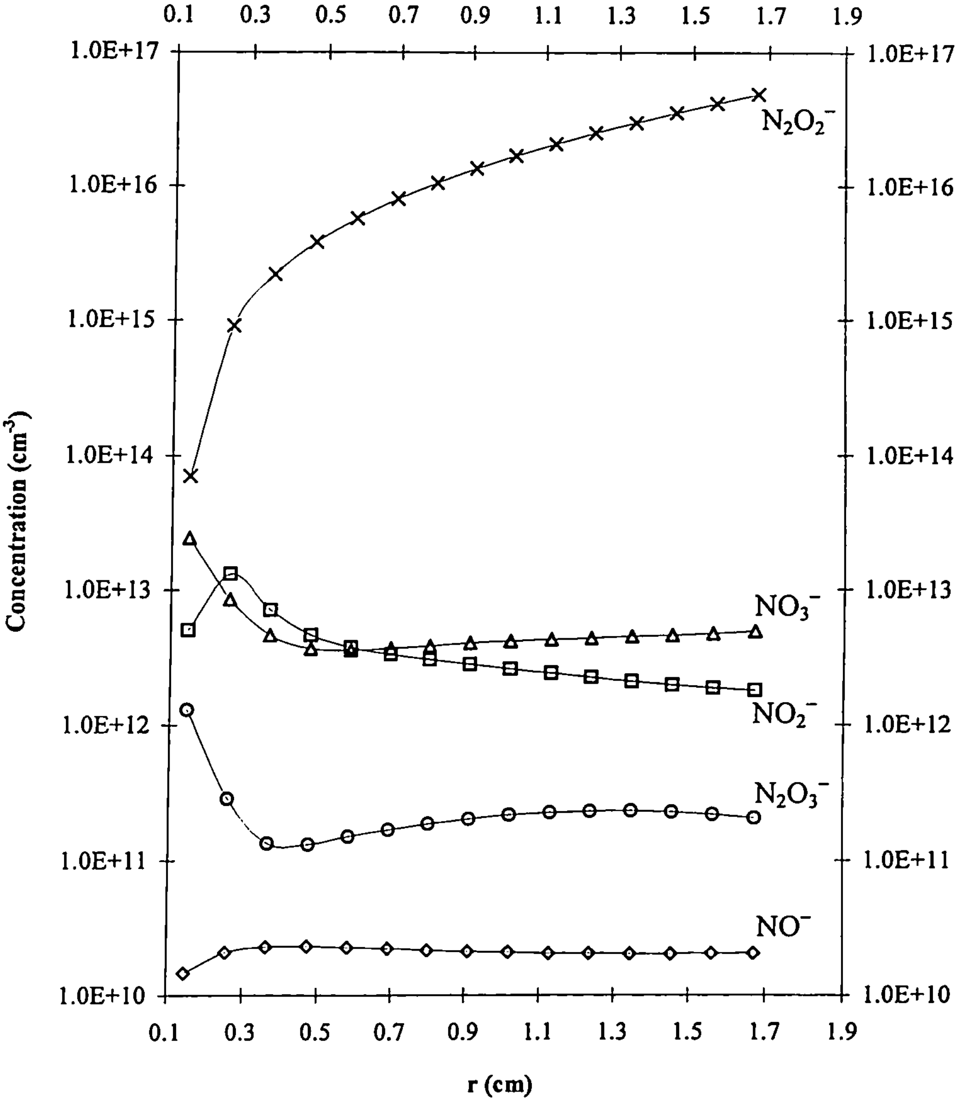

Figure 5.2.11: Radial $N_xO_y^-$ negative ions concentration profiles for a corona discharge at V = –18.0 kV and Q_g = 0.5 L/min in a 21% O_2–79% N_2 atmosphere

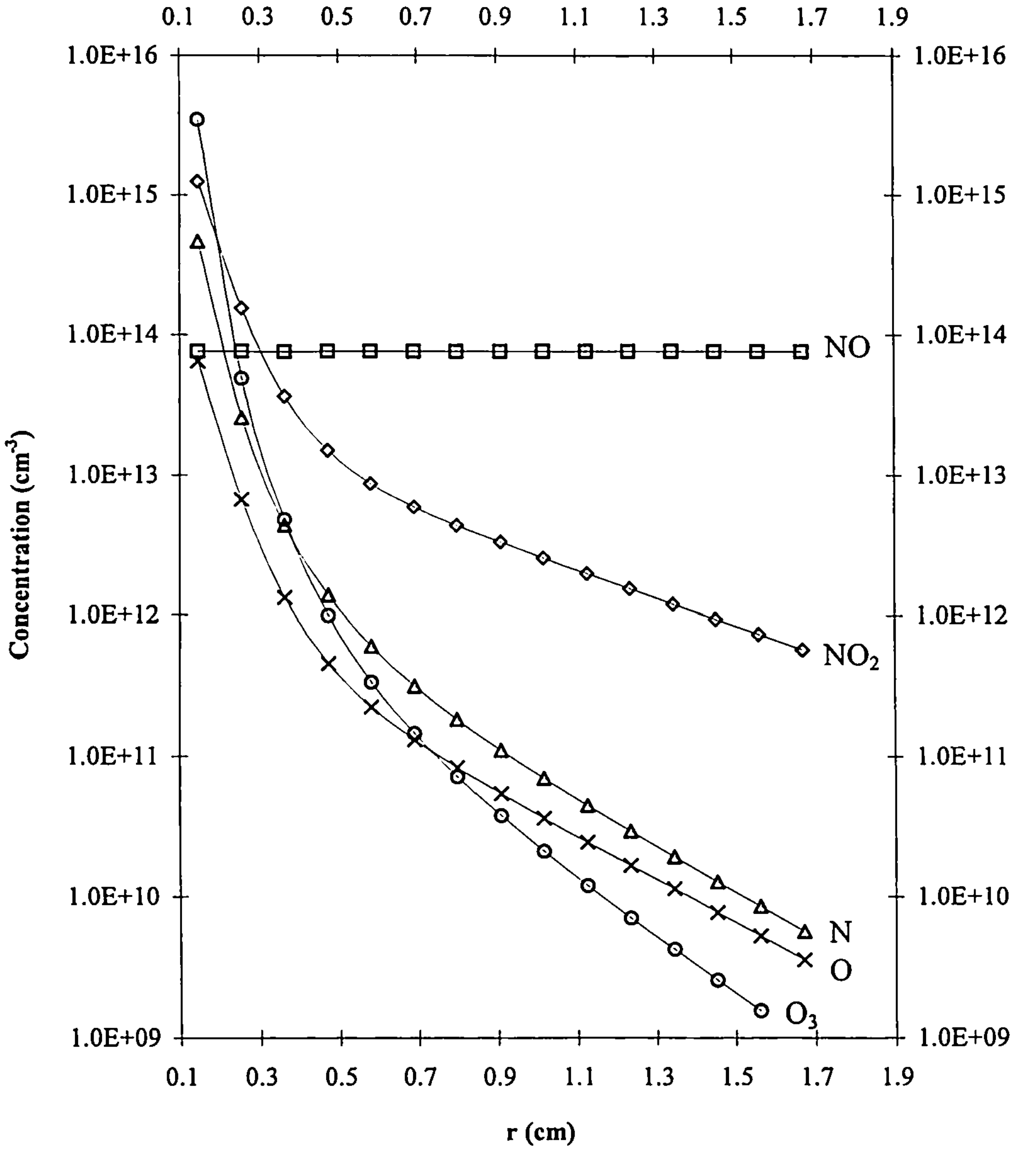

Figure 5.2.12: Radial lighter molecule radicals concentration profiles for a corona discharge at V = –18.0 kV and Q_g = 0.5 L/min in a 21% O_2–79% N_2 atmosphere

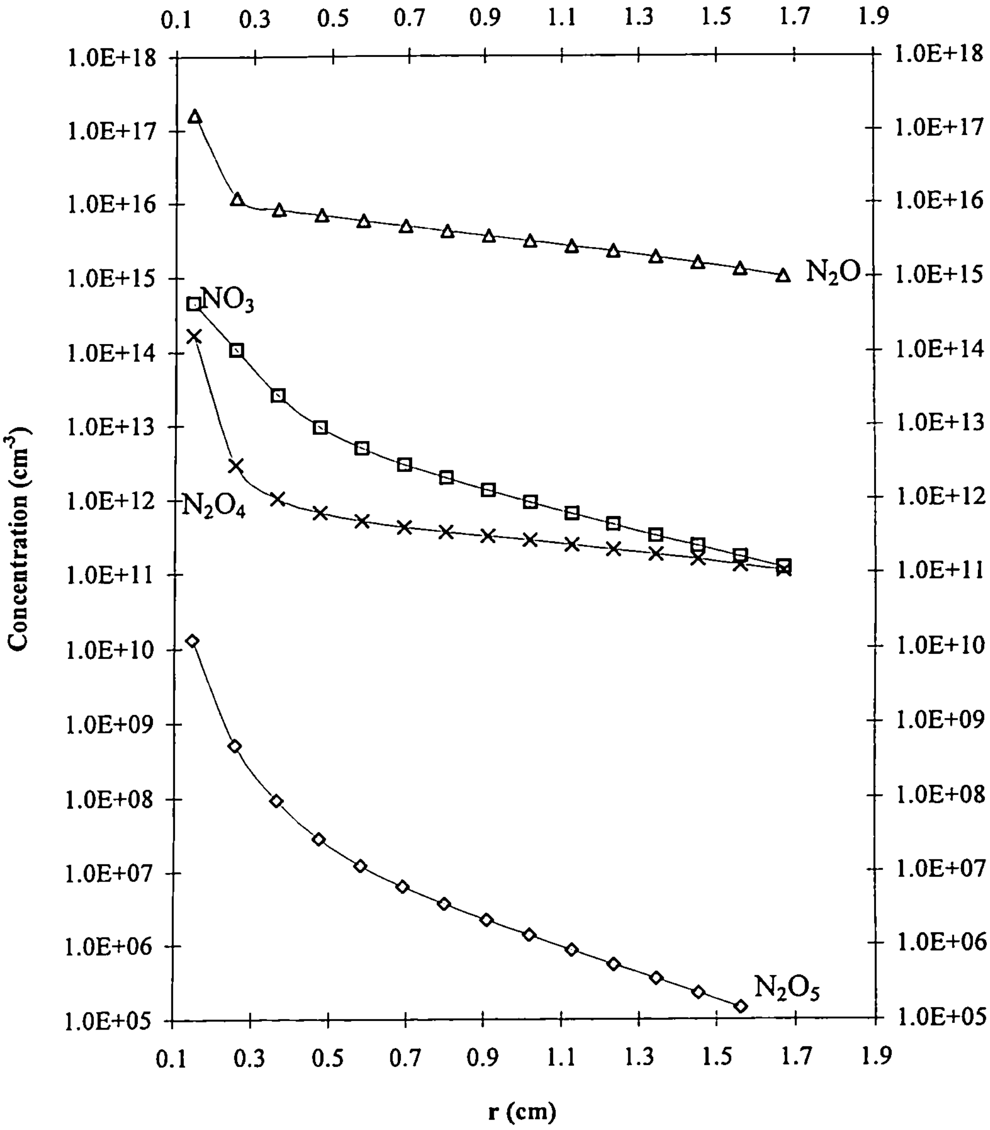

Figure 5.2.13: Radial heavier molecule radicals concentration profiles for a corona discharge at V = –18.0 kV and Q_g = 0.5 L/min in a 21% O_2–79% N_2 atmosphere

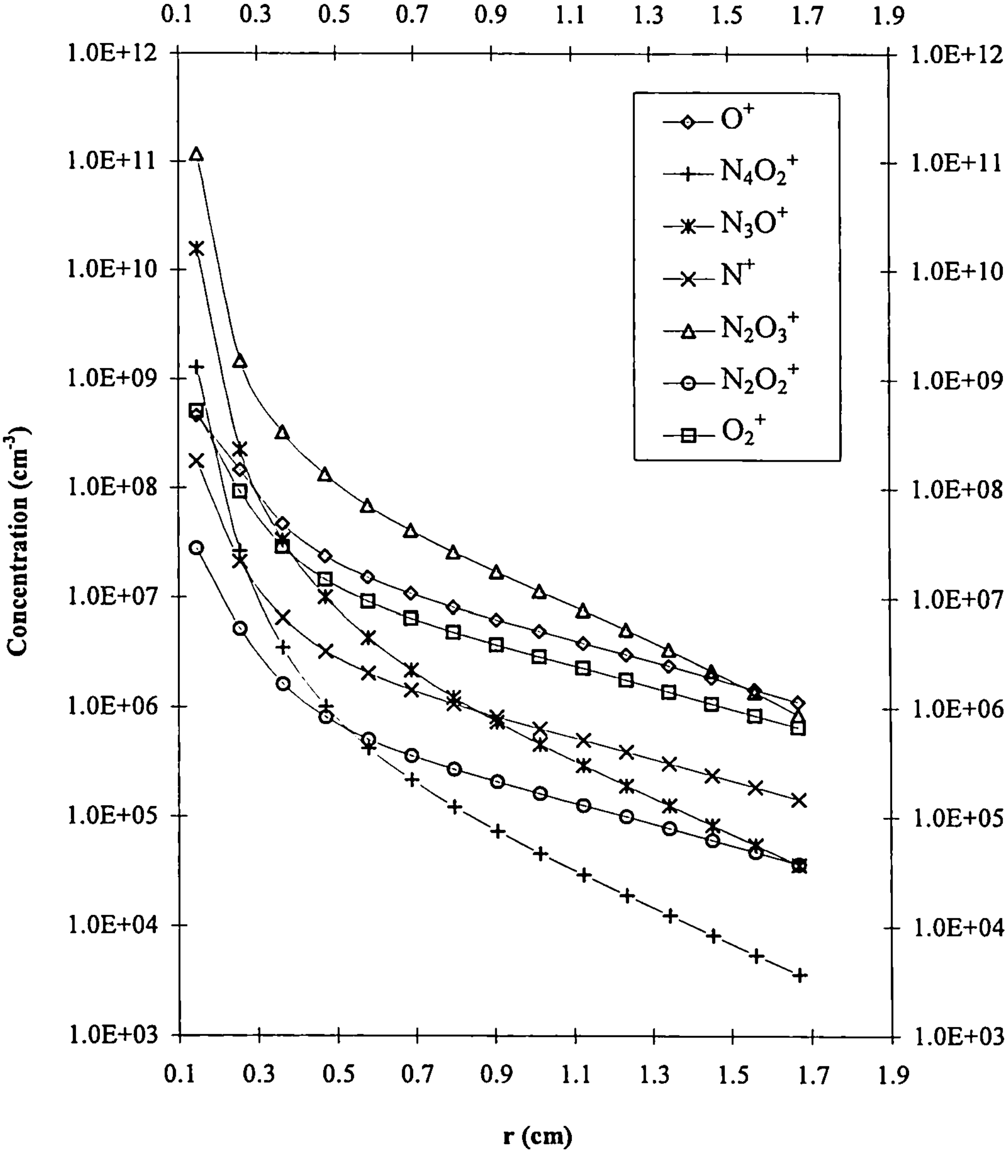

Figure 5.2.14: Radial positive ions concentration profiles for a corona discharge at V = –18.0 kV and Q_g = 0.5 L/min in a 21% O_2–79% N_2 atmosphere

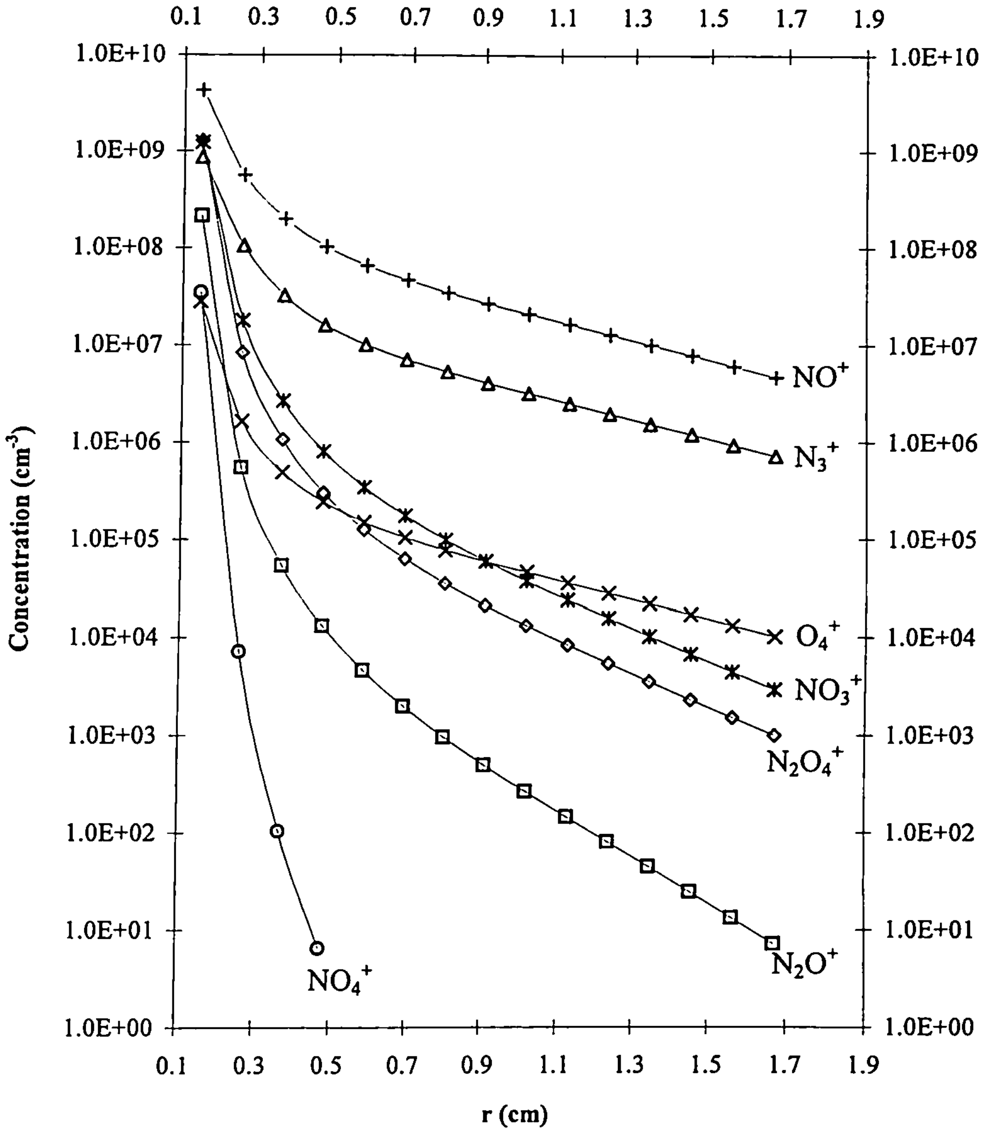

Figure 5.2.15: Radial positive ions concentration profiles for a corona discharge at V = –18.0 kV and Q_g = 0.5 L/min in a 21% O_2–79% N_2 atmosphere

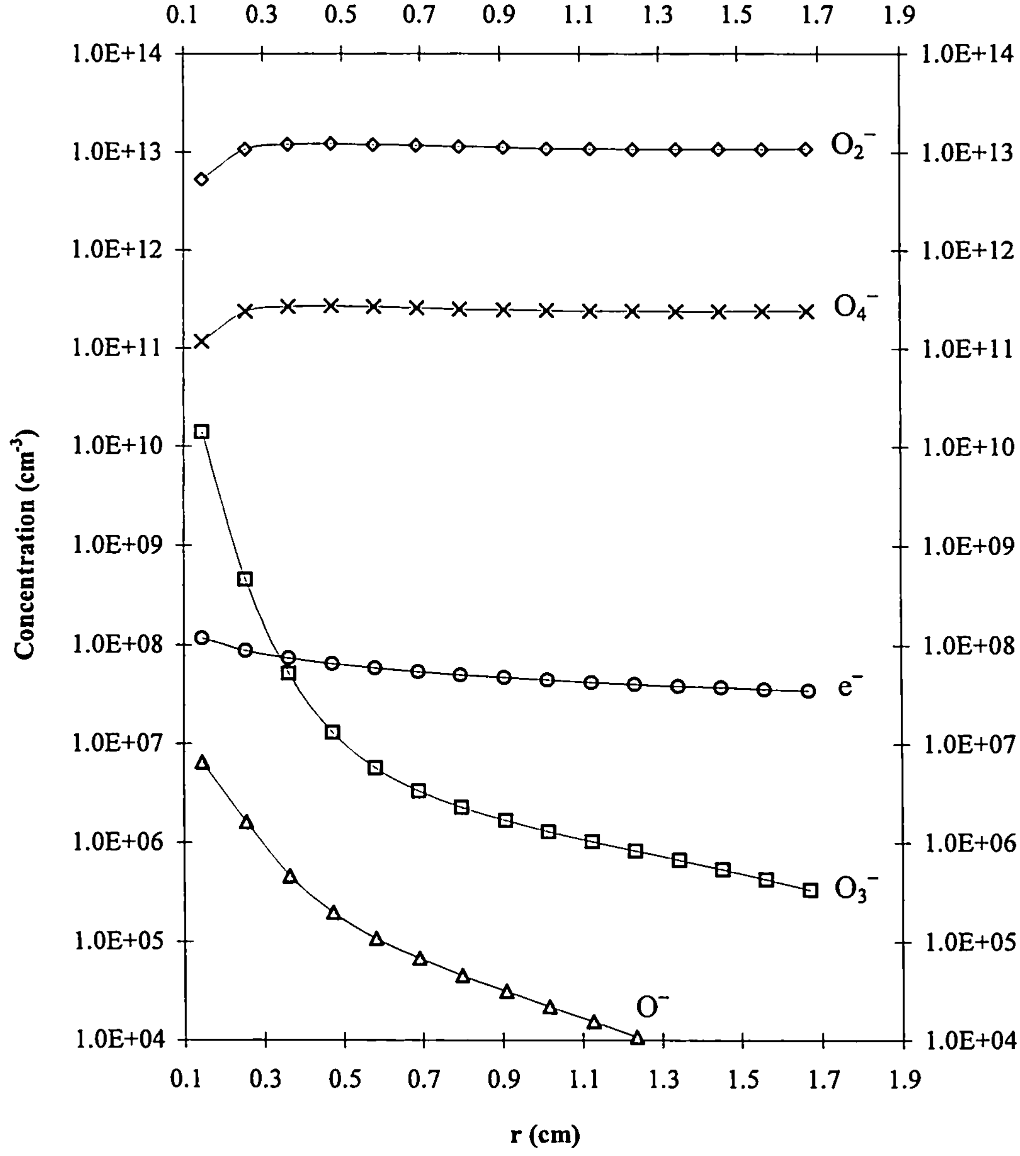

Figure 5.2.16: Radial electron and O_x^- negative ions concentration profiles for a corona discharge at $V = -18.0$ kV and $Q_g = 1.0$ L/min in a 21% O_2–79% N_2 atmosphere

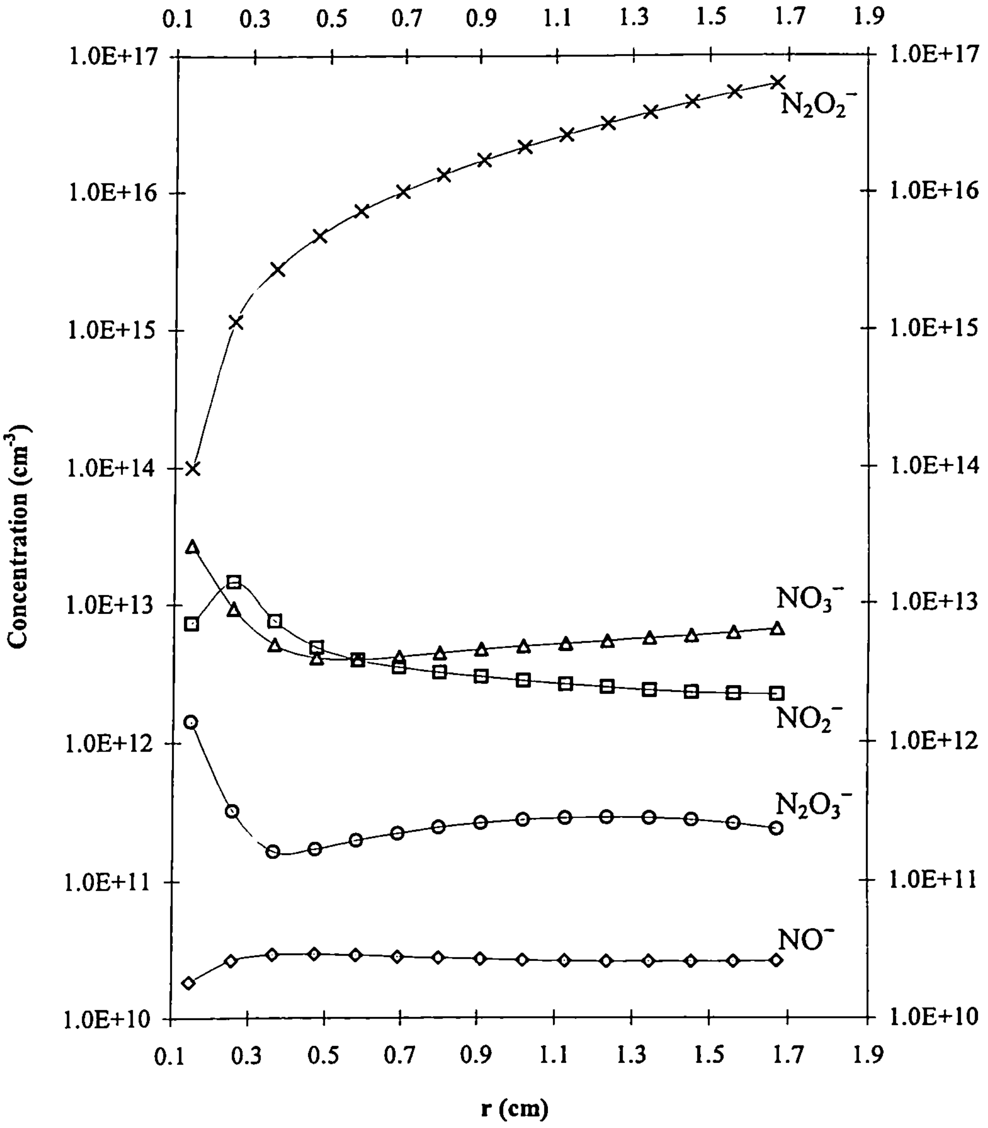

Figure 5.2.17: Radial $N_xO_y^-$ negative ions concentration profiles for a corona discharge at V = –18.0 kV and Q_g = 1.0 L/min in a 21% O_2–79% N_2 atmosphere

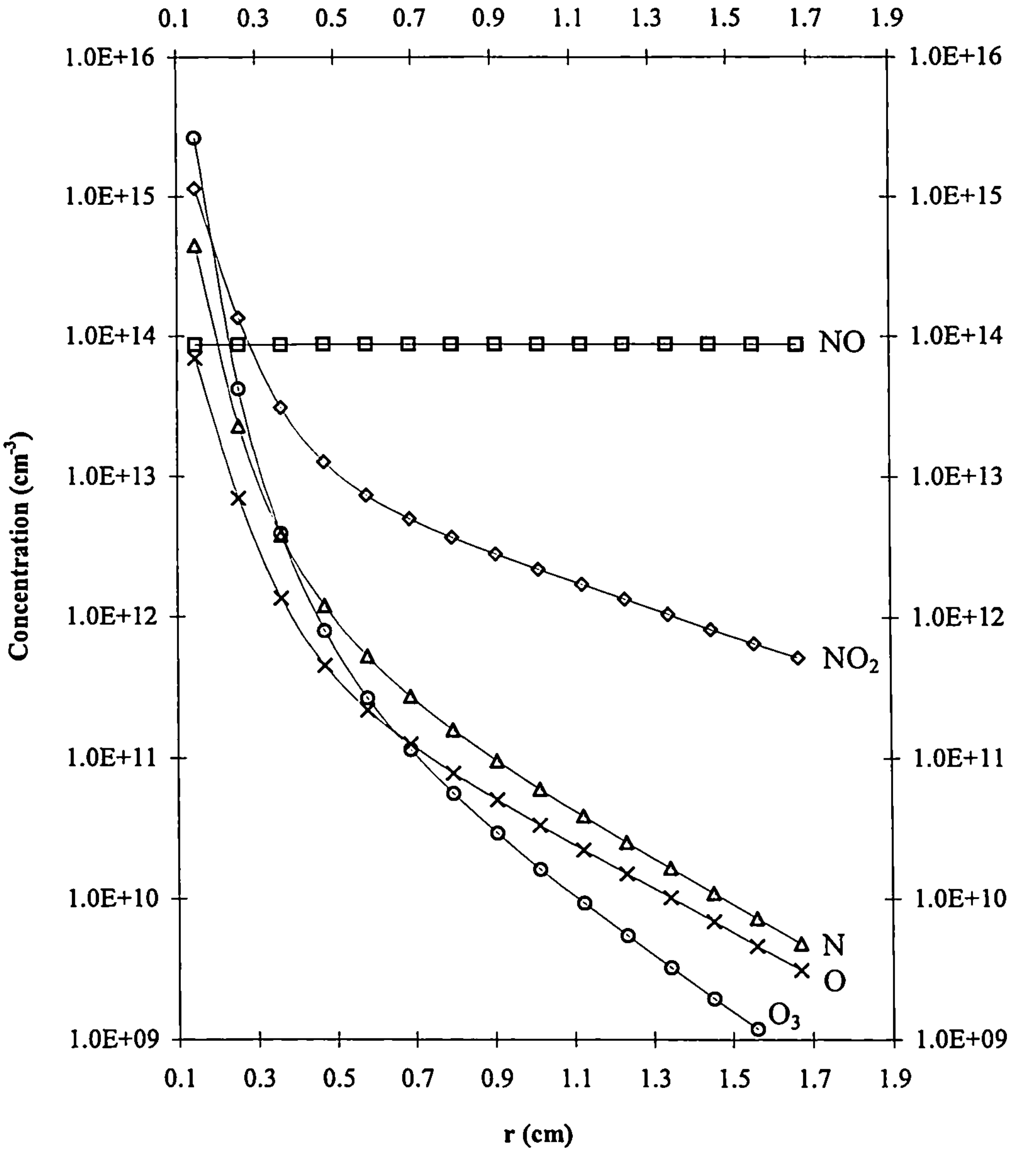

Figure 5.2.18: Radial lighter molecule radicals concentration profiles for a corona discharge at V = –18.0 kV and Q_g = 1.0 L/min in a 21% O_2–79% N_2 atmosphere

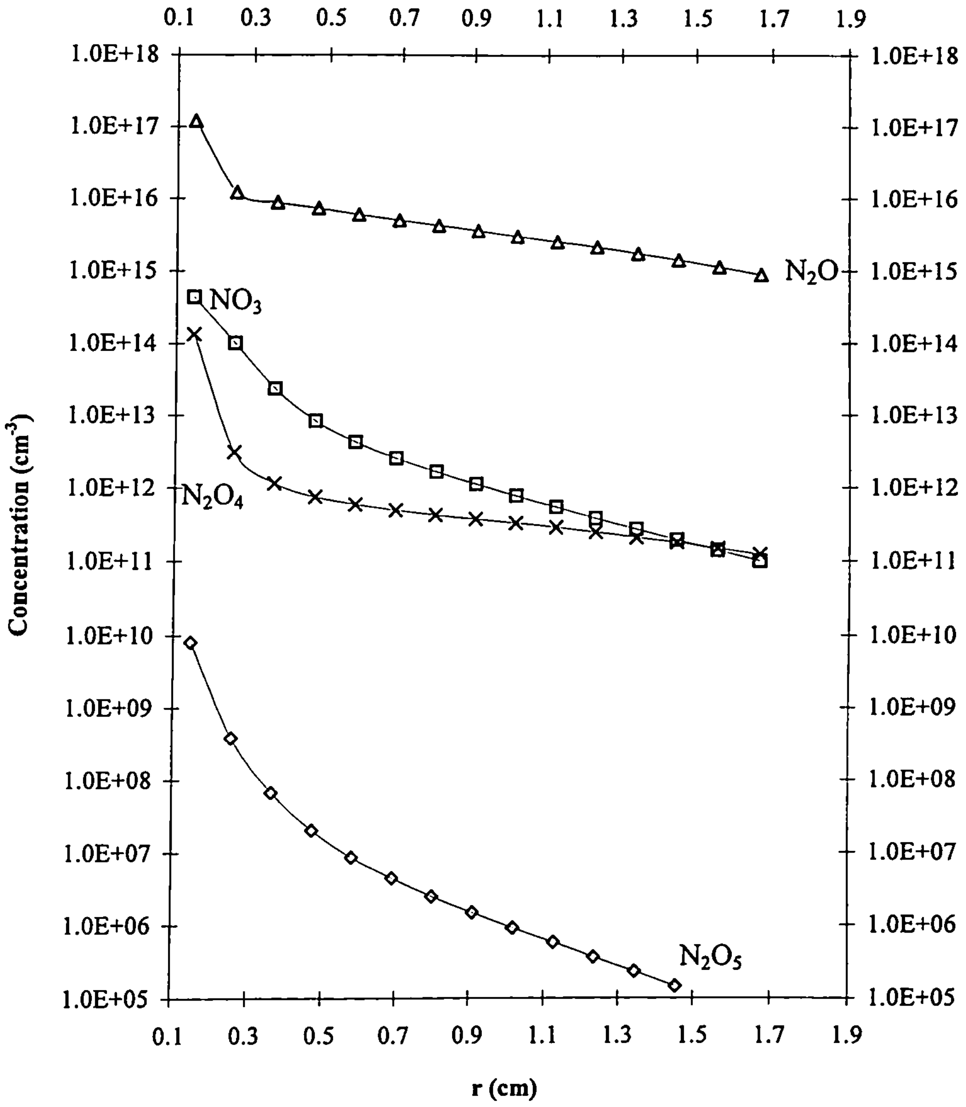

Figure 5.2.19: Radial heavier molecule radicals concentration profiles for a corona discharge at V = –18.0 kV and Q_g = 1.0 L/min in a 21% O_2–79% N_2 atmosphere

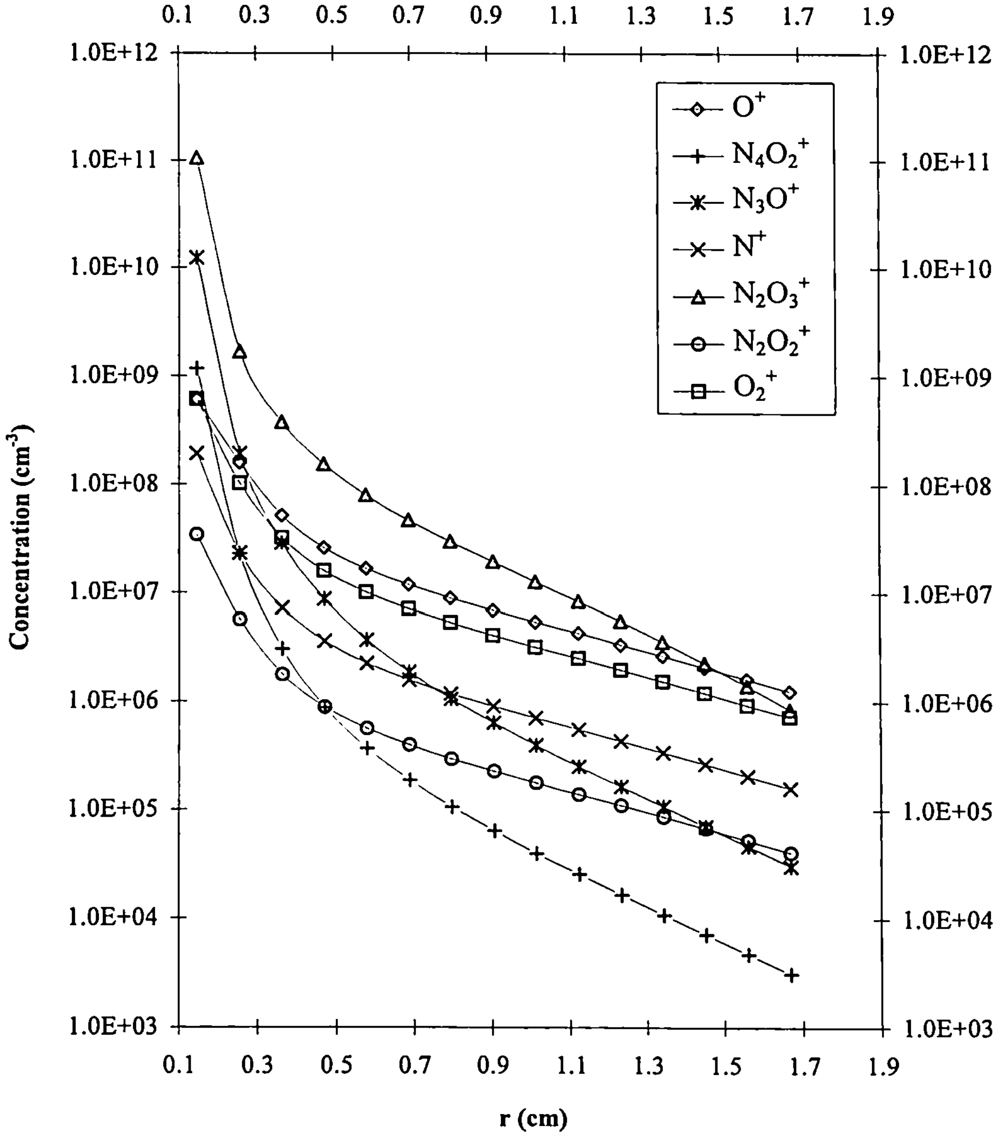

Figure 5.2.20: Radial positive ions concentration profiles for a corona discharge at V = –18.0 kV and Q_g = 1.0 L/min in a 21% O_2–79% N_2 atmosphere

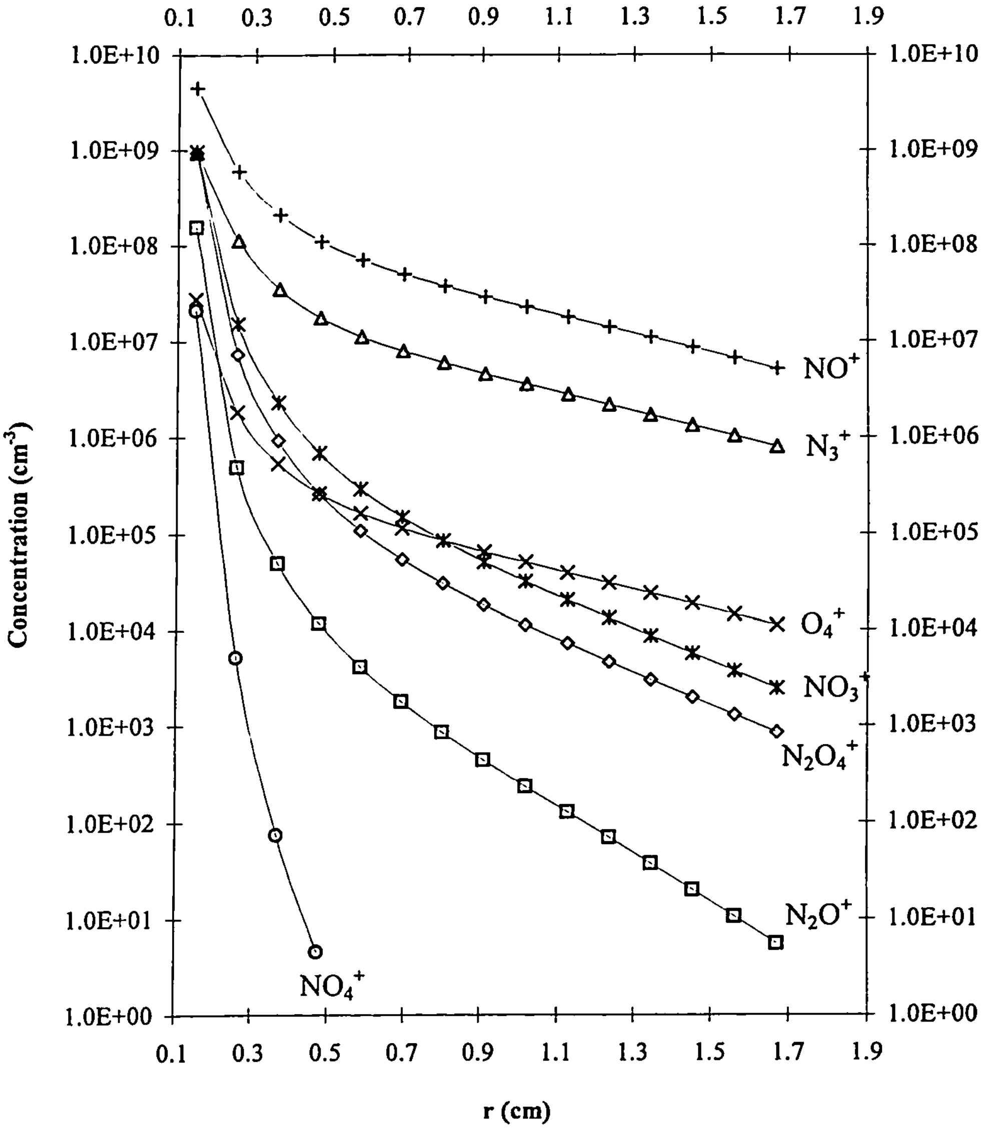

Figure 5.2.21: Radial positive ions concentration profiles for a corona discharge at V = –18.0 kV and Q_g = 1.0 L/min in a 21% O_2–79% N_2 atmosphere

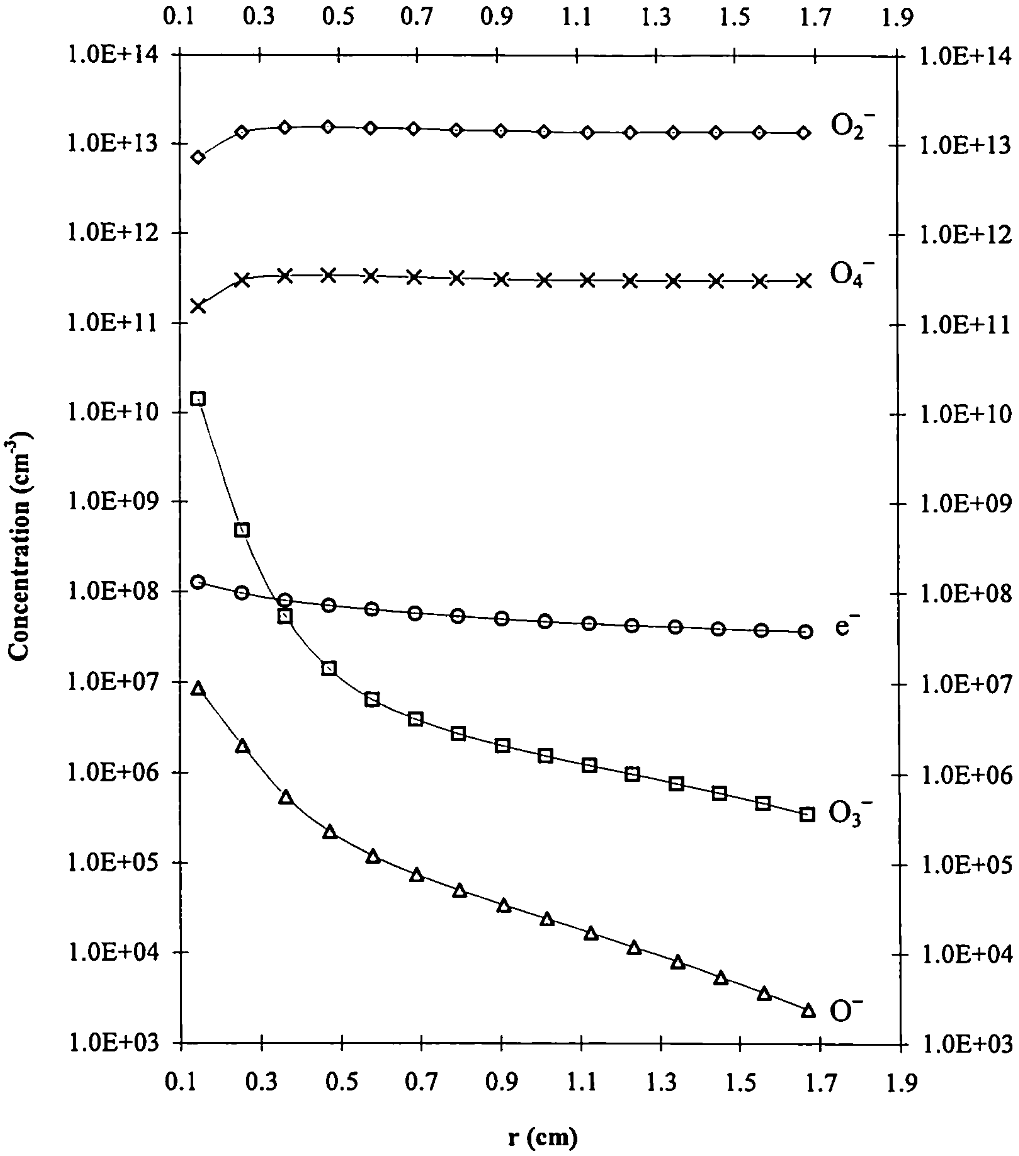

Figure 5.2.22: Radial electron and O_x^- negative ions concentration profiles for a corona discharge at V = –18.0 kV and Q_g = 1.5 L/min in a 21% O_2–79% N_2 atmosphere

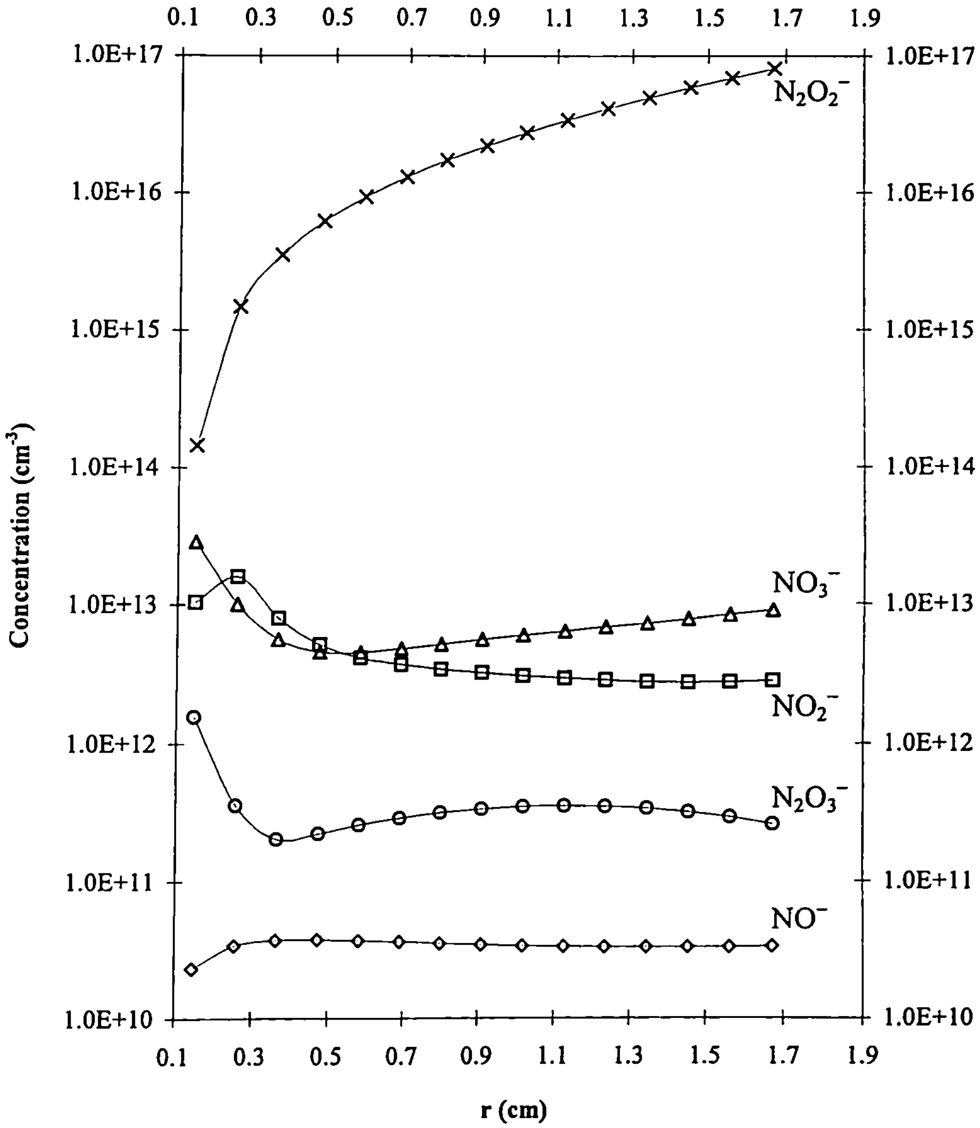

Figure 5.2.23: Radial $N_xO_y^-$ negative ions concentration profiles for a corona discharge at V = –18.0 kV and Q_g = 1.5 L/min in a 21% O_2–79% N_2 atmosphere

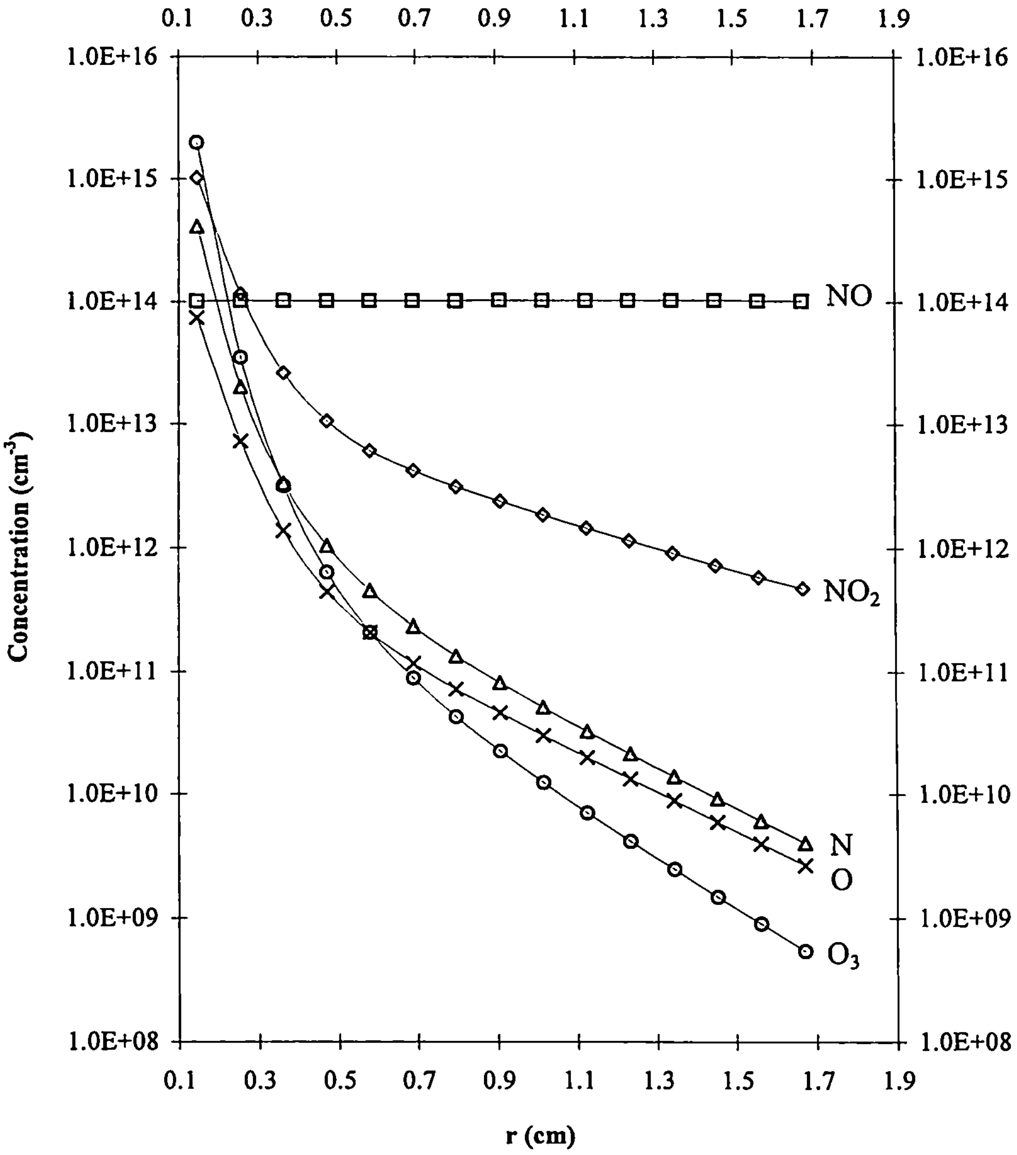

Figure 5.2.24: Radial lighter molecule radicals concentration profiles for a corona discharge at V = –18.0 kV and Q_g = 1.5 L/min in a 21% O_2–79% N_2 atmosphere

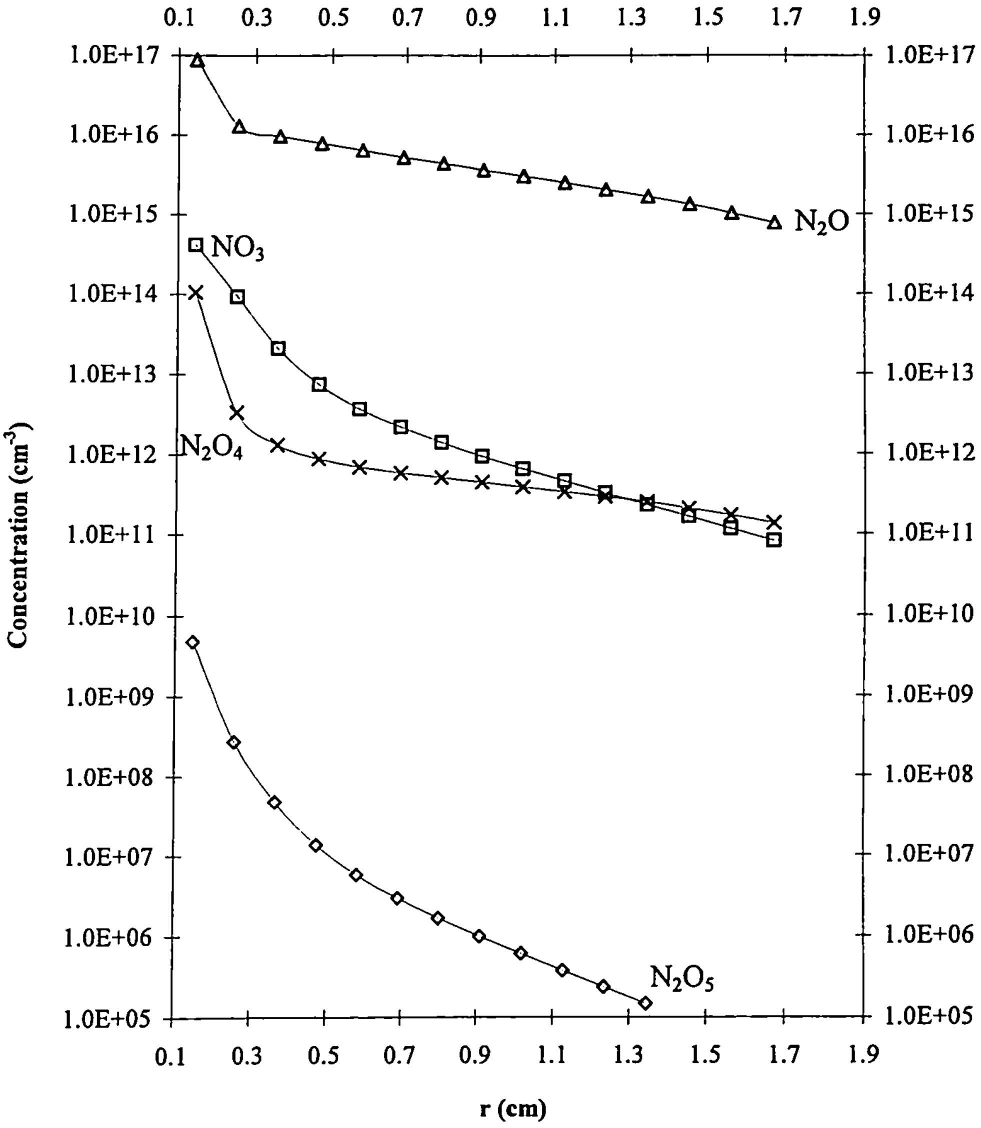

Figure 5.2.25: Radial heavier molecule radicals concentration profiles for a corona discharge at V = –18.0 kV and Q_g = 1.5 L/min in a 21% O_2–79% N_2 atmosphere

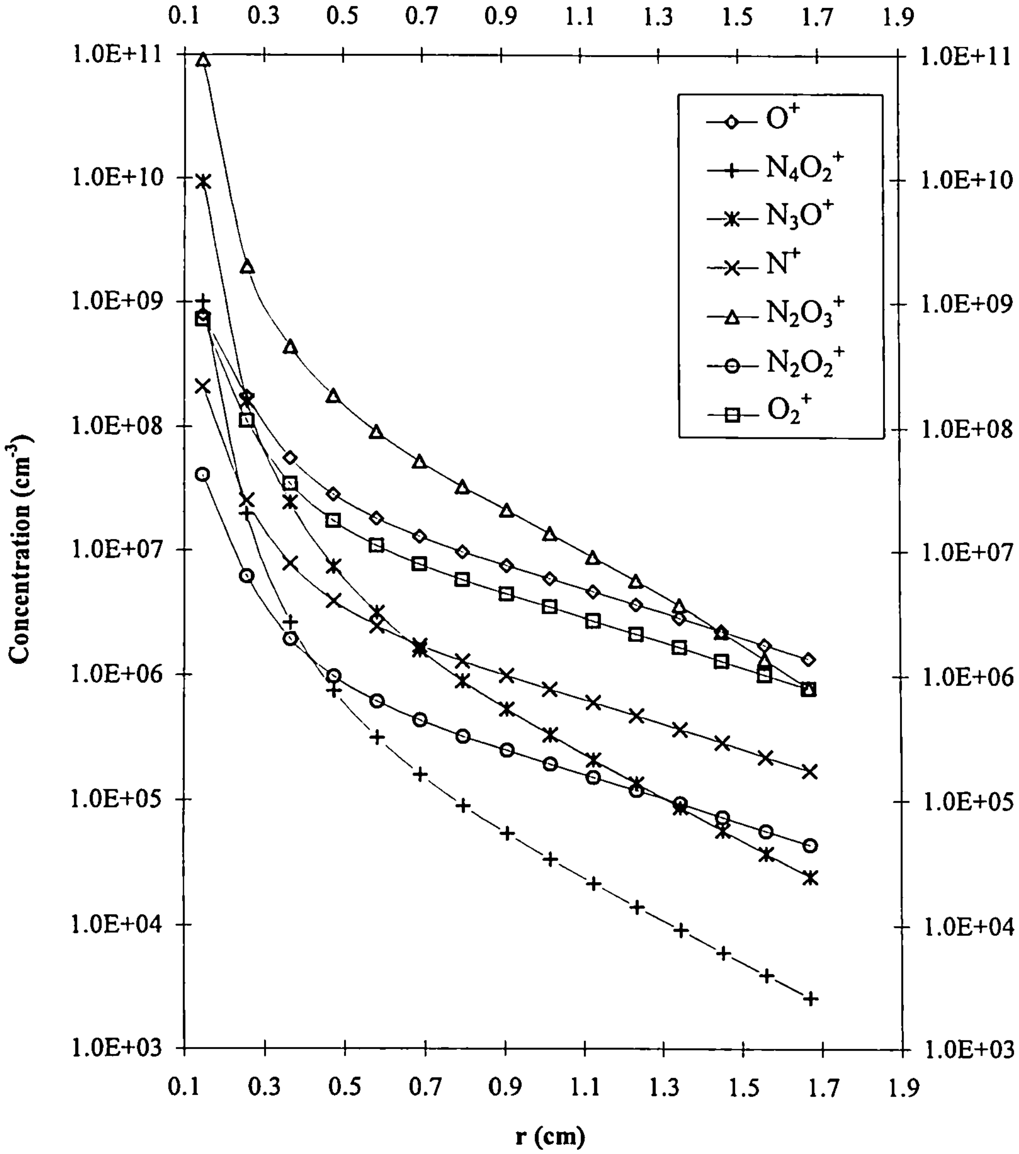

Figure 5.2.26: Radial positive ions concentration profiles for a corona discharge at V = –18.0 kV and Q_g = 1.5 L/min in a 21% O_2–79% N_2 atmosphere

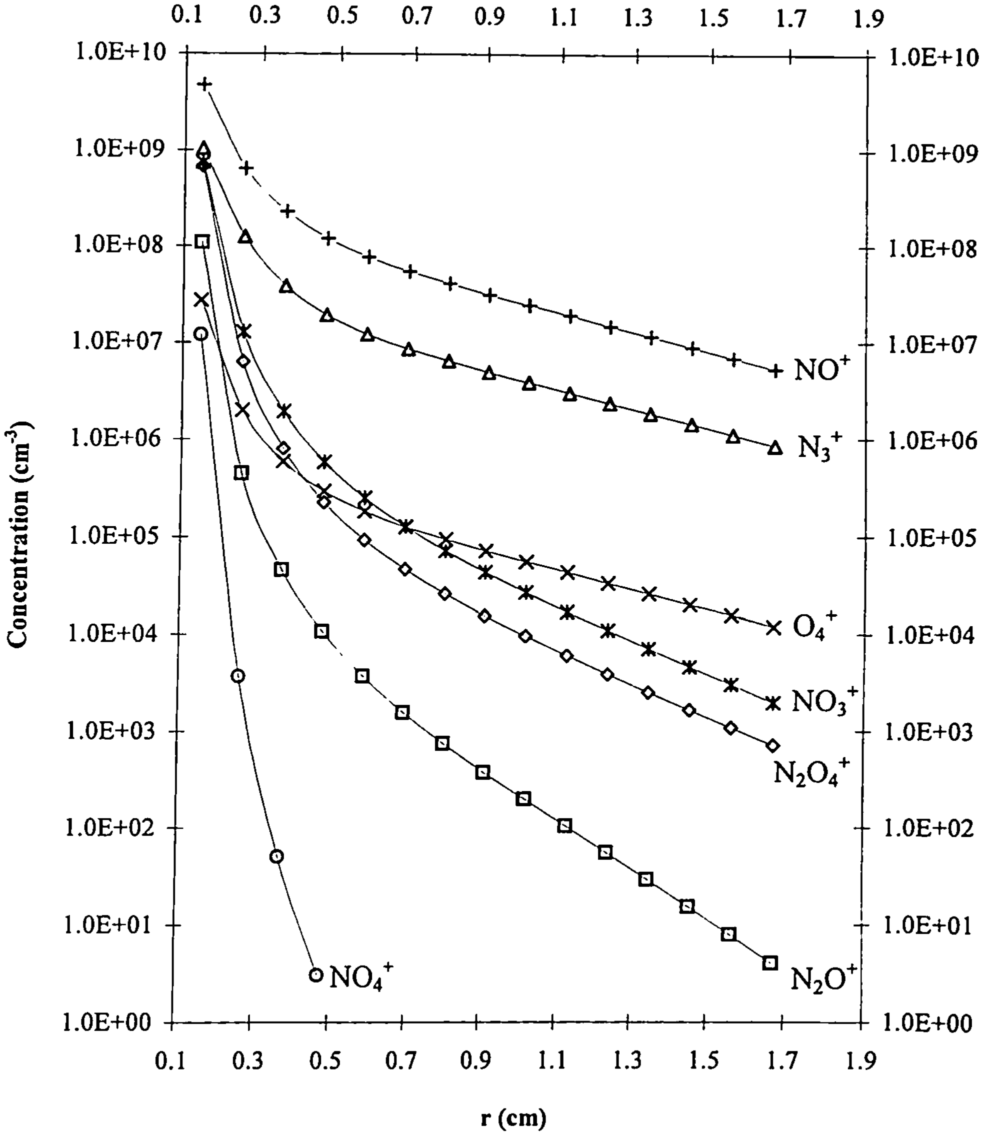

Figure 5.2.27: Radial positive ions concentration profiles for a corona discharge at V = –18.0 kV and Q_g = 1.5 L/min in a 21% O_2–79% N_2 atmosphere

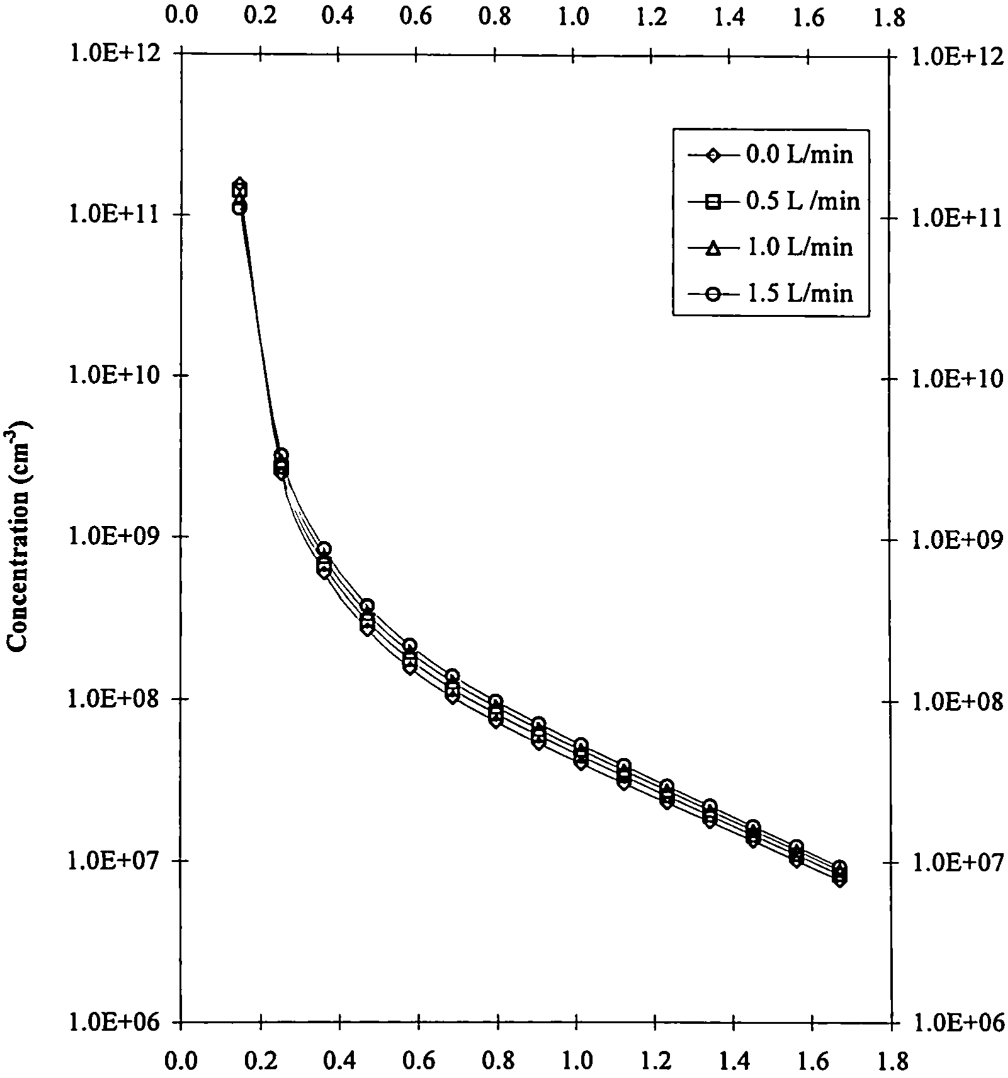

Figure 5.2.28: The effect of the gas flow rate on the total positive ion density radial profiles

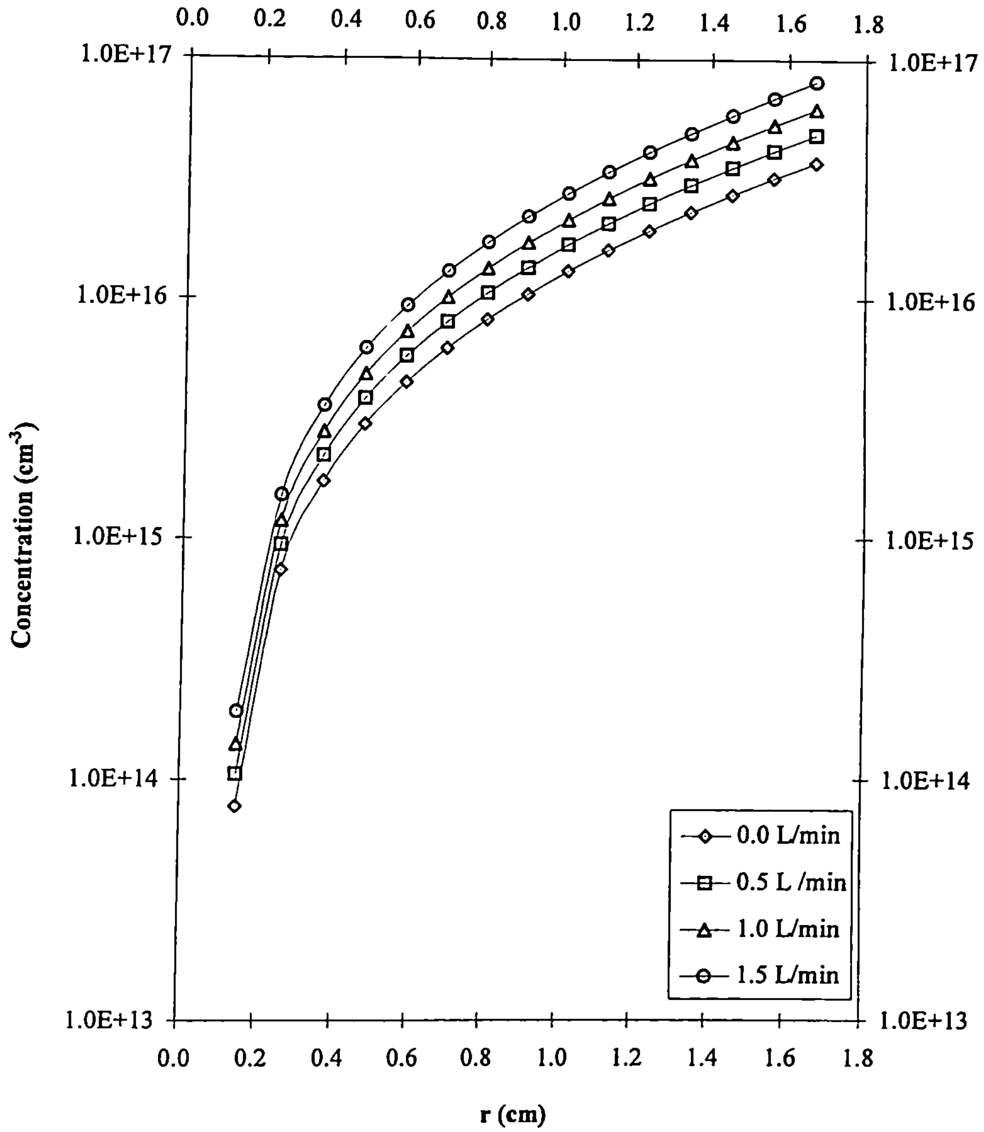

Figure 5.2.29: The effect of the gas flow rate on the total negative ion density radial profiles

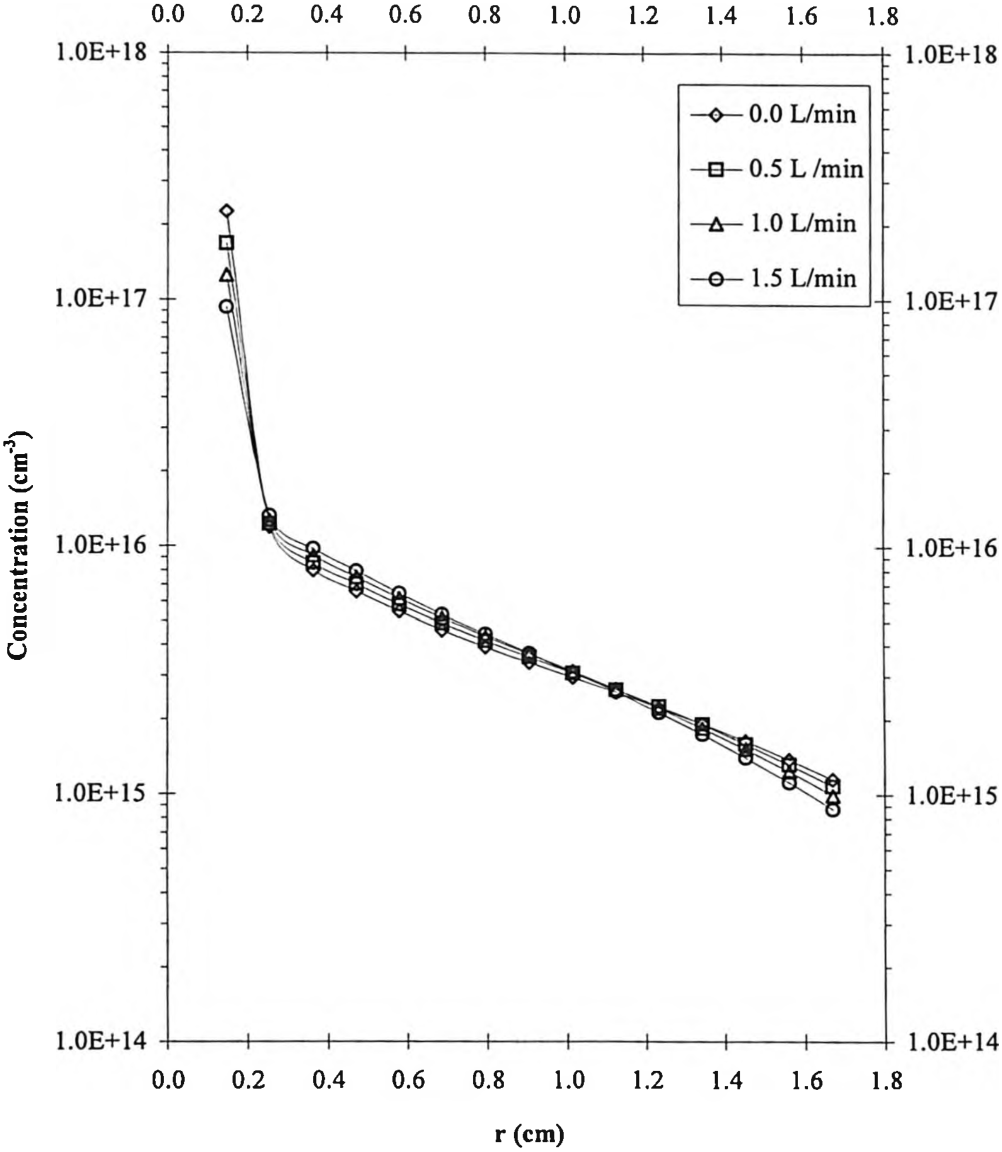

Figure 5.2.30: The effect of the gas flow rate on the total neutral radical density radial profiles

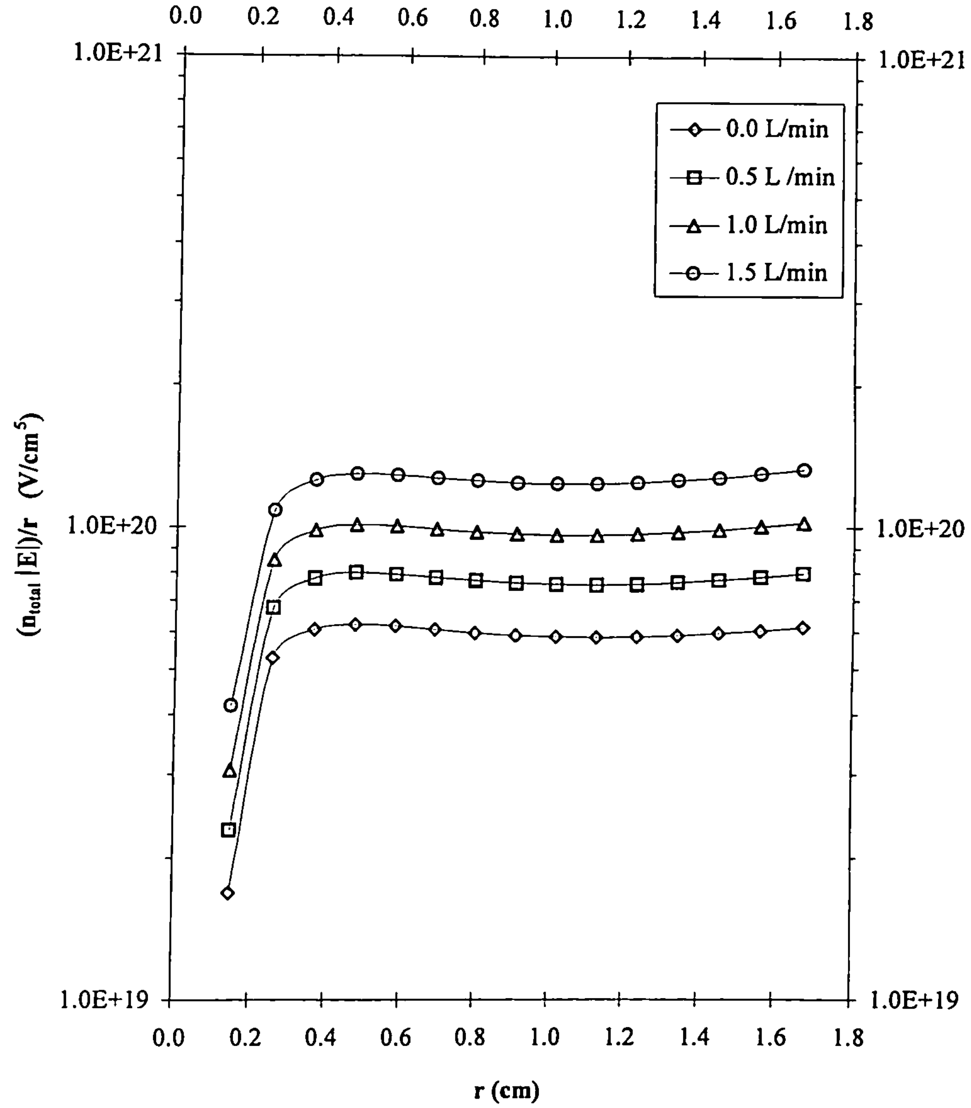

Figure 5.2.31: The effect of the gas flow rate

on the current density radial profiles

5.3. Sensitivity Analysis

Since the radial step size (Δr) is utilized in the computations of the divergence of the ion density and the Laplacian of the particle density as shown in Equations 4.2.24 and 4.2.25, the value of the step size used may affect the simulation results. Therefore, four different step sizes are simulated in order to study the effect of the radial step size on the computational results. These four step sizes are: 0.011 cm, 0.028 cm, 0.055 cm and 0.083 cm. The averaged difference between the computed concentrations of 36 trace chemical species for these step sizes are shown in Figure 5.3.1.

Figure 5.3.1 shows that the numerical errors due to the insubstantial small step size can be minimized (to less than few percentage) when one uses a step size below 0.011 cm. Another observation is that the error seems to be the largest for the first radial position (near the corona wire), and becoming almost constant afterward. One possible explanation for this larger error is that the initial concentration guesses for the first radial position are inputted by the user (arbitrary guesses), while the initial guess for all other radial positions utilize the results from the previous radial position. Therefore, the initial guess for the first radial position may not be as accurate as the other initial guesses and may resulted in a larger error in the computed concentrations. Since the average difference between the step size of 0.011 cm and 0.028 cm is less than 5.0% for most of the radial positions, the value of 0.011 cm is used in the present simulations as mentioned in Section 4.2.

The effect of the conversion criterion on the numerical results is examined in Figure 5.3.2. Three different conversion criteria are investigated. They are: 0.1, 0.01 and 0.005. From Figure 5.3.2, one may observed that the results are similar to the result for the radial step size in that the largest error occur at the first radial position and drop to almost a constant level afterward. This larger numerical error may also be caused by the arbitrary initial concentration guesses for the first radial position as mentioned before. Since the averaged numerical error for 36 trace chemical species between the conversion criteria of 0.01 and 0.005 is about 2% for most radial positions. The value of 0.005 (or 0.5%) is used as the conversion criterion for all the simulations as mentioned in Section 4.5. Another reason for using this value instead of a smaller error is because tighter conversion criterion tends to create oscillations in the resulting concentrations. This may be explained by the fact that the concentrations for various species can easily be a factor of 10,000 difference. Therefore, a tighter conversion criterion in a larger concentration species may cause the density of the smaller concentration species to change dramatically. Consequently, convergence can not be easily achieve with a tighter conversion criterion.

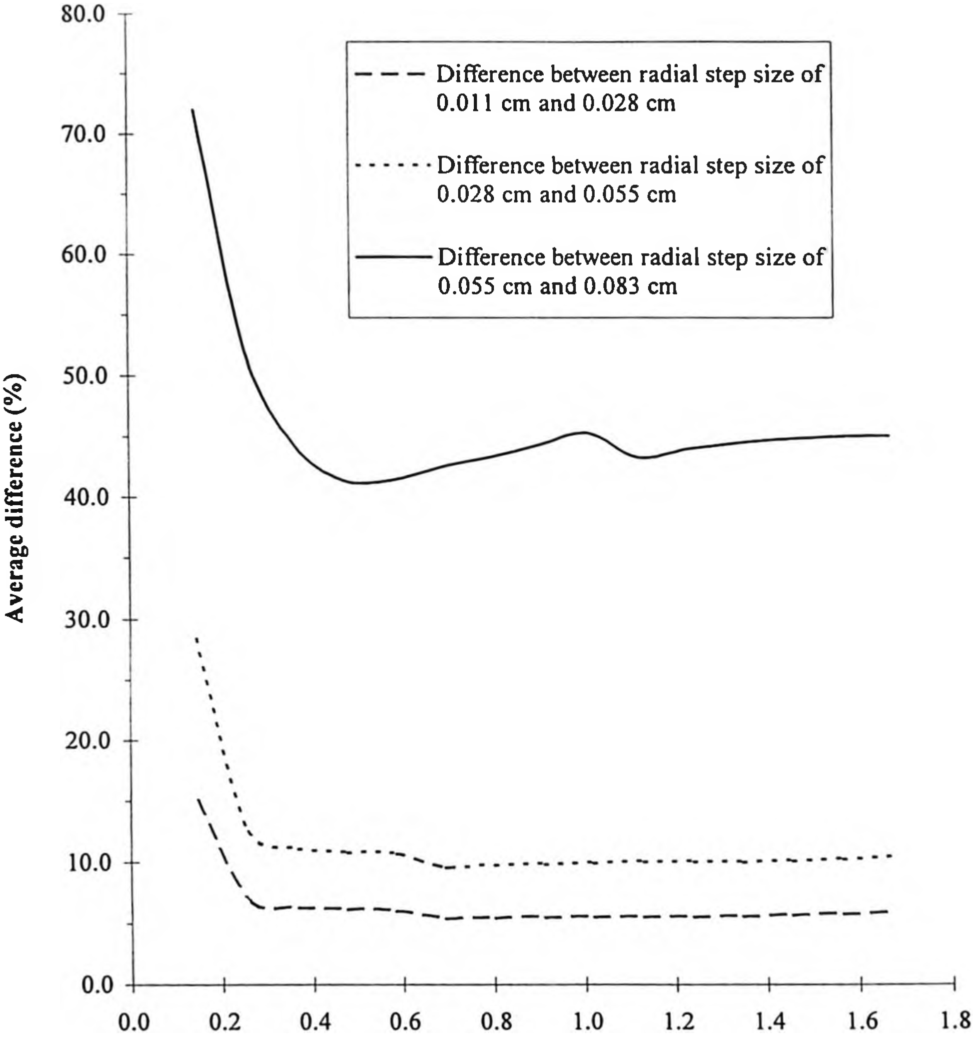

r (cm)

Figure 5.3.1: The effect of the radial step size on the 36 species radial concentration profiles computations

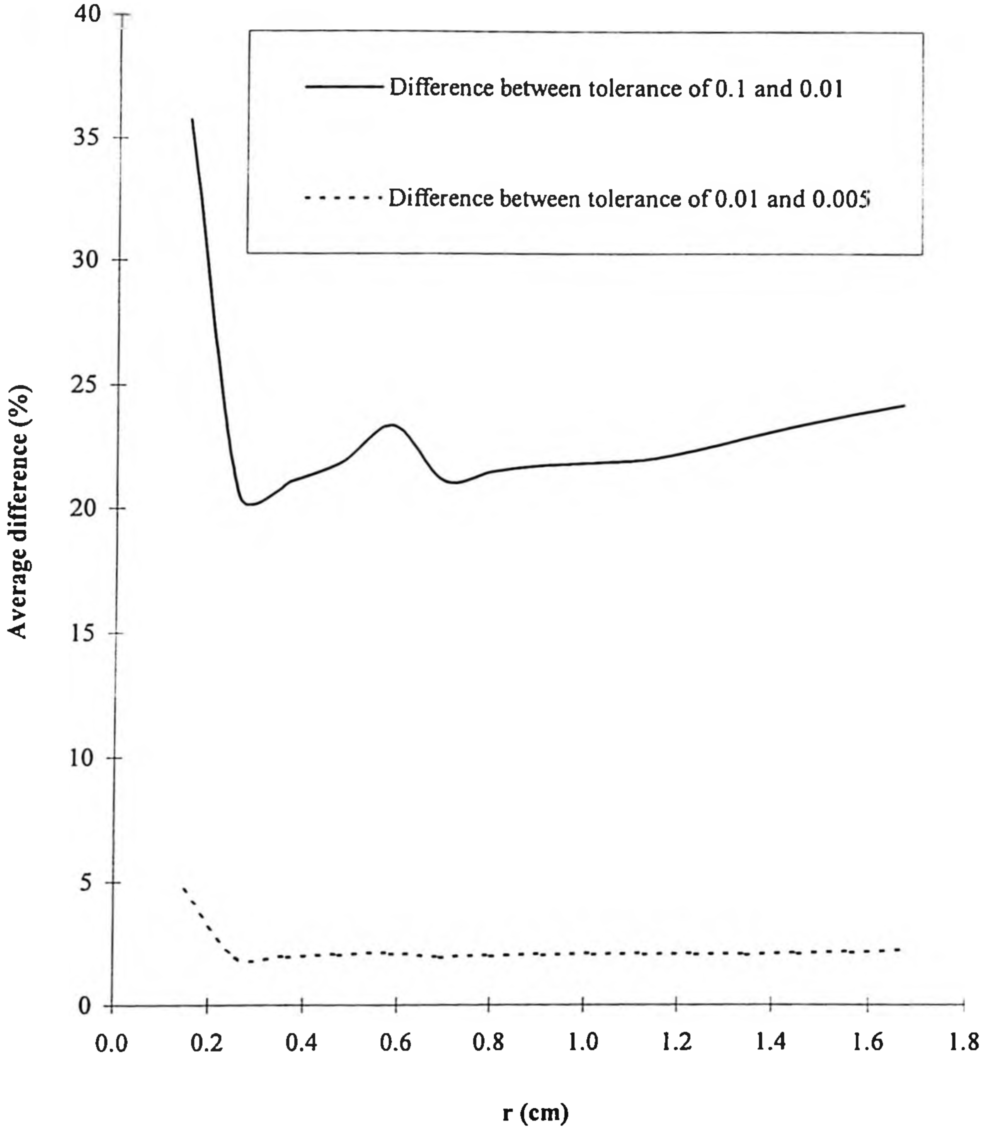

Figure 5.3.2: The effect of the convergence criterion on the 36 species radial concentration profiles computations

6. Conclusions

A numerical model is constructed for a negative dc corona discharge in a coaxial wire-tube electrode system in dry air. In this model, the continuity equations and the charged (or neutral) particle transport equations are solved simultaneous with the Poisson's equation. The electric field and the electron density are calculated based on the modified Loeb's model [16], while the total charge flux, the divergence of the electric field, the divergence of the particles density and the Laplacian of the particles density is approximated using the electron density.

One hundred and ninety-five chemical reactions for 38 different chemical species are included in the present model. These species can be divided into three groups. The first group is the negative ions which includes O^-, O_2^-, O_3^-, O_4^-, NO^-, NO_2^-, NO_3^-, $N_2O_2^-$ and $N_2O_3^-$. The second group is the neutral radicals which includes O, O_2, O_3, N, N_2, NO, NO_2, N_2O, NO_3, N_2O_4 and N_2O_5. The third group is the positive ions which includes O^+, O_2^+, O_4^+, O_6^+, N^+, N_2^+, N_3^+, N_4^+, NO^+, NO_2^+, NO_3^+, NO_4^+, N_2O^+, $N_2O_2^+$, $N_2O_3^+$, $N_2O_4^+$, N_3O^+ and $N_4O_2^+$. Due to the fact that the numerical model is intended for a negative dc corona discharge in dry air (which is assumed to be composed of 79% N_2 and 21% O_2), the concentrations of N_2 and O_2 are assumed to be at a constant value of 1.94577×10^{19} cm^{-3} and 5.1723×10^{18} cm^{-3} respectively.

Only the radial direction is considered in the present model. Fifteen equally spaced grid points is utilized in the simulations. The conversion criterion for the present model is set to be 0.5%. From this numerical model, the following conclusions are obtained:

1. The total concentrations of the trace neutral radical species are generally higher than the concentrations of the negative ions, which in term are generally larger than the concentrations of the positive ions;
2. The total concentrations of the negative ions tends to increase as the radial distance increases towards the grounded electrode;
3. The total concentrations of the positive ions and trace neutral radicals tends to decrease as the radial distance increases towards the grounded electrode;
4. The total concentrations of the positive ions, negative ions and trace neutral radicals, as well as the current density, increase with increasing applied voltage;
5. Due to the small enhancement of the time averaged discharge current by gas flow rate, only an small increase (compared to the applied voltage effect) in the total concentrations of the negative ions is observed as the gas flow rate is increased. The gas flow rate have no significant effect on the

concentration of the positive ions and neutral radicals when compared to the applied voltage effect;

6. The current density for the corona discharge increases as the applied voltage or the gas flow rate increases. However, the increase in gas flow rate is small when compared to the applied voltage effect;
7. For the present model, the radical with the highest concentration near the corona wire and the grounded electrode is N_2O. Ozone have the second highest concentration near the corona wire but its concentration decreases dramatically as the radial distance increases towards the grounded electrode;
8. For the present model, the radicals with the second highest concentration near the grounded electrode are both NO and NO_2. However, the concentration of the NO_2 tends to decrease as the radial distance increases towards the grounded electrode, while the concentration of NO tends to remain constant as the radial distance increases;
9. For the present model, the negative ion with the highest concentration near the corona wire and the grounded electrode is $N_2O_2^-$. The concentrations of NO_3^-, NO_2^- and O_2^- near the corona wire is also very close to the concentration of $N_2O_2^-$. However, the concentration of these negative ions tends to decrease (NO_3^-) or remain constant (O_2^-) as the radial distance

increases towards the grounded electrode, while the concentration of $N_2O_2^-$ tends to increase as the radial distance increases;

10. For the present model, the positive ion with the highest concentration for the lower applied voltages is NO_3^+. However, the concentrations of $N_2O_4^+$ and $N_4O_2^+$ is also very close to the concentration of NO_3^+ for the lower applied voltage cases;
11. For the present model, the positive ion with the highest concentration for higher applied voltages is NO^+. However, the concentrations of N_3^+ and $N_2O_3^+$ is also very close to the concentration of NO^+ in these cases;
12. Finally, several toxic byproducts like O_3, NO, NO_2, N_2O_4 and N_2O_5 are observed in the simulation results. However, their maximum computed concentrations (at $V = -20$ kV) are less than the acceptable limit of 25 ppm and therefore should not be a safety concern;
13. Present model agree qualitatively well with the experimental observations of Donohoe et al. [2], Ito et al. [3], Masuda et al. [4], Hill et al. [5] and Brahdvold and Martinez [6], where N_2O, O_3, and NO_x are observed to be the major corona discharge byproducts. Traces of N_2O_3, N_2O_4 and N_2O_5 are also observed in these experiments.
14. The results obtained from the present model agree qualitatively well with the results of Penetrante's model [1], where a high concentrations of N_2O, NO_2 and NO_3 is predicted. However, a high concentrations of O_3 and

N_2O_5 is also observed in Penetrante's model. This is different from what the present model is predicting. One possible reason may be due to the smaller number of ions and radical species, as well as chemical reactions, considered in Penetrante's work.

15. The results obtained from the present model disagree with the model presented by Mukkavilli et al. [28] and Tochikubo et al. [41], since both models oversimplified the chemical reactions and the number of species need to be considered.
16. By comparing with the other chemical models, the present model demonstrated that the contributions of ions are significant in predicting radical species concentrations, and most of the chemical species show significant radial distributions. Hence, an oversimplified chemical model and volume averaged model should be reconsidered for predicting the concentrations of the chemical species generated during a corona discharge.

7. Recommendations for Future Work

For future development, the following suggestions may be incorporated into the next generation model to enhanced its accuracy and/or performance:

1. The gas convection term in the transport equation (both charged and neutral) should be included in the next generation model since future applications of the corona plasma reactor should be extended to the larger gas flow rate conditions.
2. The present model assume the charge flux is dominated by the electrons. This is reasonable for a rough estimate. However, for better estimation of concentrations, a more accurate method of determining the total charged flux (like including the concentrations of all other charged particles) is needed.
3. The divergence and Laplacian of the particle densities utilized in the transport equations is approximated using the radial electron density profiles. Although this should provide a reasonable first order estimate, a better way of computing these values should produce more accurate results.
4. The current method of estimating the diffusion coefficient and ion mobility (for charged particles only) are very crude. Although this is adequate in

providing first order estimates, a better method of determine these variables should be apply to the next generation model if possible.

5. Finally if one desire a more accurate determination of the concentrations, a better convergence method will be needed since the current method cannot utilized a very tight convergence criterion.

8. References

1. B.M. Penetrante, "Plasma Chemistry and Power Consumption in Non-thermal DeNO$_x$" in Non-Thermal Plasma Techniques for Pollution Control, edited by B.M. Penetrante and S.E. Schultheis, Springer-Verlag, Berlin, pp. 65-89, 1993.
2. K. Donohoe, F.H. Shair and O.R. Wulf, "Production of O_3, NO and N_2O in a Pulsed Discharge at 1 atm.", *Ind. Eng. Chem. Fundam*, **16** : 208, 1977.
3. T. Ito, M. Kaneko, M. Shiomi and T. Sakai, "The Generation and Stability of Gaseous Products Generated by Discharge in Air", *Ooyo Butsuri*, **49** : 446, 1980.
4. S. Masuda, Y. Wu, T. Urabe and Y. Ono, "Pulse Corona Induced Plasma Chemical Process for De-NO$_x$, De-SO$_x$ and Mercury Vapour Control of Combustion Gas", *Third International Conference on Electrostatic Precipitation*, edited by M. Rea, pp. 667-676, 1987.
5. R.D. Hill, I. Rahmin and R.G. Rinker, "Experimental Study of Production of NO, N_2O, and O_3 in a Simulated Atmospheric Corona", *Ind. Eng. Chem. Res.*, **27** : 1264, 1988.
6. D.K. Brahdvold and P. Martinez, "Polarity Dependence of N_2O Formation from Corona Discharge", *Atmosph. Environ.*, **22** : 2477, 1989.

7. F.A.L. Dullien, "Introduction to Industrial Gas Cleaning", Academic Press, Inc., San Diego, 1989.

8. A.J. Buonicore and L. Theodore, "CRC Industrial Control Equipment for Gaseous Pollutants, Volume I", CRC Press, Inc., Cleveland, 1975.

9. D.O. Reimann, "Limitations of Flue-gas Cleaning", *Chemistry & Industry*, 659, September 1993.

10. R.H. Shannon, "Handbook of Coal-Based Electric Power Generation", Noyes Publications, New Jersey, 1982.

11. J.S. Chang, P.C. Looy, K. Nagai, T. Yoshioka, S. Aoki and A. Maezawa, "Preliminary Pilot Plant Tests of a Corona Discharge-Electron Beam Hybrid Combustion Flue Gas Cleaning System", *IEEE Transactions on Industry Applications*, **32** : 131, 1996.

12. K. Onda, K. Kato, and Y. Kasuga, "SO_2 and NO_x Removal from Combustion Flue Gas by Corona Discharge in Laboratory-Scale Experiment", *JSME International Journal*, **39** : 202, 1996.

13. J.S. Chang, "Energetic Electron Induced Plasma Processes for a Reduction of Acid and Greenhouse Gases in a Combustion Flue Gas" in Non-Thermal Plasma Techniques for Pollution Control, edited by B. Penetrante, Plenum Press, New York, pp. 1-32, 1994.

14. J.S. Chang, P.A. Lawless and T. Yamamoto, "Corona Discharge Processes", *IEEE Transactions on Plasma Science*, **19** : 1152, 1991.

15. M. Goldman, A. Goldman and R.S. Sigmond, "The Corona Discharge, its properties and specific uses", *Pure & Appl. Chem.*, **57** : 1353, 1985.

16. L.B. Loeb, "Electrical Coronas", University of California Press, Berkeley and Los Angeles, 1965.

17. J.S. Chang and S. Masuda, "Mechanism of Pulse Corona Induced Plasma Chemical Process for Removal of NO_x and SO_2 from Combustion Gases", *Conference Record of the 1988 IEEE Industry Applications Society Annual Meeting*, Pittsburgh, Pennsylvania, pp. 1628-1636, October 1988.

18. T. Ohkubo, S. Kanazawa, Y. Nomoto, J.S. Chang and T. Adachi, "NO_x Removal by a Pipe with Nozzle-Plate Electrode Corona Discharge System", *IEEE Transactions on Industry Applications*, **30** : 856, 1994.

19. I. Gallimberti, "Impulse Corona Simulation for Flue Gas Treatment", *Pure & Appl. Chem.*, **60** : 663, 1988.

20. G. Dinelli, L. Civitanto and M. Rea, "Industrial Experiments on Pulse Corona Simultaneous Removal of NO_x and SO_2 from Flue Gas", *IEEE Transactions on Industry applications*, **26** : 535, 1990.

21. T. Yamamoto, J.S. Chang, A.A. Berezin, J. Kohno, S. Honda and A. Shibuya, "Decomposition of Toluene, o-Xylene, Trichloroethylene and Their Mixture Using a $BaTiO_3$ Packed-Bed Plasma Reactor", *J. Adv. Oxid. Technol.*, **1** : 67, 1996.

22. H. Kohno, M. Tamura, A. Shibuya, S. Honda, A.A. Berezin, J.S. Chang and T. Yamamoto, "Destruction of Volatile Organic Compounds Used in a Semiconductor Industry by a Capillary Tube Discharge Reactor", *Conference Record of the 1995 IEEE Industry Applications Society, 30th IAS Annual Meeting*, Orlando, Florida, pp. 1445-1453, October 1995.

23. S. A. Hoenig, G.T. Sill, L.M. Kelley and K.J. Garvey, "Destruction of Bacteria and Toxic Organic Chemicals by a Corona Discharge", *Journal of the Air Pollution Control Association*, **30** : 277, 1980.

24. E.W. McDaniel, "Collision Phenomena in Ionized Gases", John Wiley, New York, 1969.

25. J.S. Chang, R.M. Hobson, Y. Ichikawa and T. Kaneda, "Atomic and Molecular Processes in an Ionized Gas", Tokyo Denki University Press, Tokyo, 1984.

26. T.G. Bethe and J.S. Chang, "Gas Discharge Phenomena" in Ch. 9, Handbook of Electrostatic Processes, edited by J.S. Chang, A.J. Kelly and J.M. Crowley, Marcel Dekker, Inc., New York, 1995.

27. A.A. Belevtsev and L.M. Biberman, "On the Theory of Corona Discharge", *Beitr. Plasmaphys.*, **23** : 313, 1983.

28. S. Mukkavilli, C.K. Lee, K. Varghese and L.L. Tavlarides, "Modeling of the Electrostatic Corona Discharge", *IEEE Transactions on Plasma Science*, **16** : 652, 1988.

29. B. Eliasson and U. Kogelschatz, "Modeling and Applications of Silent Discharge Plasmas", *IEEE Transactions on Plasma Science*, **19** : 309, 1991.

30. A.A. Kulikovsky, "Production of Chemically Active Species in the Air by a Single Positive Streamer in a Nonuniform Field", *IEEE Transactions on Plasma Science*, **25** : 439, 1997.

31. E.W. McDaniel and H.R. Crane, "Measurements of the Mobilities of the Negative Ions in Oxygen and in Mixtures of Oxygen with the Noble Gases, Hydrogen, Nitrogen and Carbon Dioxide", *Review of Scientific Instruments*, **28** : 684, 1957.

32. M. Lecuiller, R. Julien and J. Pucheault, "Chemical Study on Ions Produced by Corona Discharge", *J. Chim. Phys.*, **69** : 1353, 1972.

33. A. Goldman, R. Hang and R.V. Latham, "A Repulsive-Field Technique for Obtaining the Mobility-Spectra of the Ion Species Created in a Corona Discharge", *Journal of Applied Physics*, **47** : 2418, 1976.

34. J.S. Chang, "Chemical Reactions Leading to an Aerosol Particle Formation and Growth by an Irradiation of High Energy Electron Beam", *2nd International Aerosol Conference*, Berlin, Germany, pp. 867-871, 1986.

35. J.S. Chang, "Mechanism of NH_4NO_3 Aerosol Particle Formation by Streamer Corona Discharges", *Third International Conference on Electrostatic Precipitation*, Abano-Padova, Italy, pp. 653-661, October 1987.

36. J.S. Chang, "The Role of H_2O and NH_3 on the Formation of NH_4NO_3 Aerosol Particles and De-NOx Under the Corona Discharge Treatment of Combustion Flue Gases", *J. Aerosol Sci.*, **20** : 1087, 1989.

37. F. Pontiga, J.S. Chang, A. Kwan and A. Castellanos, "Chemical and Physical Modelling of Dry Air with Trace Toluene in a Coaxial Wire-Pipe Negative Corona Discharge", *The Third International Conference on Advanced Oxidation Technologies for Water and Air Remediation*, Cincinnati, Ohio, page 23, October 1996.

38. D. Braun, U. Kuchler and G. Pietsch, "Microdischarges in air-fed ozonizers", *Journal of Physics D-Applied Physics*, **24** : 564, 1991.

39. P.A. Vitello, B.M. Penetrante and J.N. Bardsley, "Simulation of Negative-Streamer Dynamics in Nitrogen", *Physical Review E*, **49** : 5574, 1994.

40. A.A. Kulikovsky, "Two-Dimensional Simulation of the Positive Streamer in N_2 between Parallel-Plate Electrodes", *Journal of Physics D-Applied Physics*, **28** : 2483, 1995.

41. F. Tochikubo, A. Miyamoto and T. Watanabe, "Simulation of Streamer Propagation and Chemical Reaction in Pulsed Corona Discharge", *The Eleventh International Conference on Gas Discharge and Their Applications*, Tokyo, Japan, pp. I-168 to 172, September 1995.

42. R. Morrow and J.J. Lowke, "Streamer Propagation in Air", *Journal of Physics D-Applied Physics*, **30** : 614, 1997.

43. A.A. Kulikovsky, "Positive Streamer between Parallel Plate Electrodes in Atmospheric Pressure Air", *Journal of Physics D-Applied Physics*, **30** : 441, 1997.

44. A.A. Kulikovsky, "The Mechanism of Positive Streamer Acceleration and Expansion in Air in a Strong External Field", *Journal of Physics D-Applied Physics*, **30** : 1515, 1997.

45. F. Pontiga, C. Soria, and A. Castellanos, "Electrical and Chemical Model of Negative Corona in Oxygen at Atmospheric Pressure", *Journal of Electrostatics*, **40&41** : 115, 1997.

46. J.S. Chang, Y.Q. Sheng, F. Pontiga, A. Castellanos, G. Sheng and G.F. Round, "Chemical and Physical Modelling of Coaxial Wire-Pipe Negative Corona Discharges", *First International Workshop on Atmospheric Pressure Gas Discharge Modelling*, Seville, Spain, page 7, February 1995.

47. J.S. Chang, F. Pontiga, P. Atten and A. Castellanos, "Hysteresis Effect of Corona Discharge in a Narrow Coaxial Wire-Pipe Discharge Tube with Gas Flow", *IEEE Transactions on Industry Applications*, **32** : 6, 1996.

48. L. Waldman and K.H. Schmitt, "Themophoresis and Diffusophoresis of Aerosols" in Aerosol Science, edited by C.N. Davies, Academic Press, New York, 1966.

49. J.R. Hook and H.E. Hall, "Solid State Physics", John Wiley & Sons, New York, 1994.

50. D.J. Griffiths, "Introduction to Electrodynamics", Prentice Hall, New Jersey, 1989.

51. L.G.H. Huxley and R.W. Crompton, "The Diffusion and Drift of Electrons in Gases", John Wiley & Sons, New York, 1974.

52. D.C. Giancoli, "Physics for Scientists and Engineers", Prentice Hall, New Jersey, 1988.

53. S.S. Zumdahl, "Chemistry, 2nd Edition", D.C. Heath and Company, Lexington, 1989.

54. G.E. Caledonia, "A survey of gas-phase negative ion kinetics of inorganic molecules. Electron attachment reaction", *Chemical Reviews*, **75** : 333, 1975.

55. D.L. Albritton, "Ion-neutral reaction-rate constants measured in flow reactors though 1977", *Atomic Data and Nuclear Data Tables*, **22** : 1, 1978.

56. R. Atkinson, D.L. Baulch, R.A. Cox, R.F. Hampson, J.A. Kerr and J. Troe, "Evaluated kinetic and photochemical data for atmospheric chemistry. Supplement IV", *Journal of Physical and Chemical Reference Data*, **21** : 1125, 1992.

57. R. Atkinson, D.L. Baulch, R.A. Cox, R.F. Hampson, J.A. Kerr and J. Troe, "Evaluated kinetic and photochemical data for atmospheric chemistry. Supplement III", *Journal of Physical and Chemical Reference Data*, **18** : 881, 1989.

58. B. Eliasson and U. Kogelschatz, “Basic data for modelling of electrical discharges in gases: Oxygen”, Technical Report KLR 86-11 C, Brown Boveri, June 1986.

59. L.M. Chanin, A.V. Phelps, and M.A. Biondi, “Measurements of the attachment of slow electrons in oxygen”, *Physical Review Letters*, **2** : 334, 1959.

60. P.C. Cosby, “Electron-impact dissociation of nitrogen”, *Journal of Chemical Physics*, **98** : 9544, 1993.

61. L.J. Kieffer, “Low-energy electron-collision cross-section data. Part I: Ionization, Dissociation, Vibrational Excitation”, *Atomic Data*, **1** : 19, 1969.

62. R.F. Hampson, “Chemical kinetic and photochemical data sheets for atmospheric reactions”, Technical Report FAA-EE-80-17, U.S. Department of Transportation, April 1980.

63. G.Y. Alekseev, A.V. Levchenko and V.A. Bityurin, “Flue Gas Cleaning by Pulse Corona, Part II”, Research Report IVTAN-ANRA #93/2, IVTAN Analytical & Numerical Research Association, June 1993.

64. L.G. Christophorn, “The Lifetimes of Metastable Negative Ions”, *Advances in Electronics and Electron Physics*, **46** : 55, 1978.

65. E. Nasser, “Fundamentals of Gaseous Ionization and Plasma Electronics”, Wiley-Interscience, New York, 1971.

66. F. Reif, " Fundamentals of Statistical and Thermal Physics", McGraw-Hill, Inc., New York, 1965.

Appendix I: Reaction Rates Correlation for Electron Impact Oxygen Ionization

Since four of the reaction rates listed in Table 4.3.2 (k_{172} to k_{175}) is approximated using the corrected version of Equation 41 from Reference 26, they will need to be validated to ensure the correlation are correct. To accomplish this task, one of the reaction rates (k_{174}) is computed using the formula shown in Table 4.3.2 and then compared with the experimental data listed in Reference 58. The results are shown in Figure 9.1.1. From Figure 9.1.1, one can observed that the calculated reaction rate are similar to the experimental data, implying that the approximations is acceptable as a good estimation.

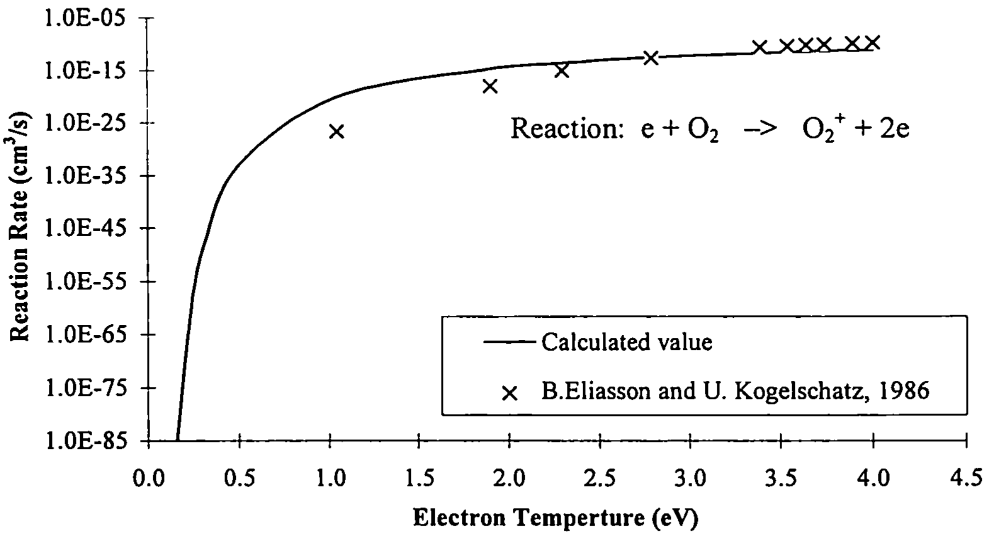

Figure 9.1.1: A comparison of the approximated reaction rate with experimental results for the reaction $e^- + O_2 \rightarrow O_2^+ + 2e^-$

Appendix II: List of Mobility and Diffusion Coefficients Used in the Present Model

Table 9.2.1: A table of the values for the ion mobility and diffusion coefficients

Name	Ion Mobility (cm^2/Vs)	Diffusion Coefficient (cm^2/s)
NO^-	2.605	0.0465
NO_2^-	1.668	0.0375
NO_3^-	1.437	0.0323
O_2^-	2.000	0.0450
O_3^-	1.633	0.0367
O^-	2.828	0.0636
$N_2O_2^-$	1.460	0.0329
O_4^-	1.414	0.0318
$N_2O_3^-$	1.298	0.0292
N_2O_5	N/A	0.0969
NO_3	N/A	0.1279
NO_2	N/A	0.1485
NO	N/A	0.1838
N	N/A	0.2690
O	N/A	0.2517
N_2O	N/A	0.1518
O_3	N/A	0.1453
N_2O_4	N/A	0.1050
O^+	1.414	0.0976
$N_4O_2^+$	0.603	0.0416
N_3O^+	0.743	0.0512
$N_2O_4^+$	0.590	0.0407
N_2O^+	0.853	0.0588
NO_4^+	0.640	0.0422
NO_3^+	0.718	0.0496
N_2^+	1.069	0.0737

Table 9.2.1: Continue

Name	Ion Mobility (cm^2/Vs)	Diffusion Coefficient (cm^2/s)
N^+	1.511	0.1043
NO^+	1.033	0.0713
N_3^+	0.873	0.0602
O_6^+	0.577	0.0398
O_4^+	0.707	0.0488
N_4^+	0.756	0.0521
$N_2O_3^+$	0.649	0.0488
$N_2O_2^+$	0.730	0.0504
NO_2^+	0.834	0.0575
O_2^+	1.000	0.0690

Appendix III: Finite Difference Model

In order to improve the accuracy of the divergence of the ion density ($\nabla \cdot n_k$) and the Laplacian of the particle density ($\nabla^2 n_k$), an attempt to compute these terms using the actual particle densities with the finite difference iterative method (instead of the electron density as shown in Equations 4.2.1 and 4.2.2) is experimented. But to the fact that the particle densities were what one try to obtain in this simulation, this causes the computation to become radial dependent as well. Consequently, this lead to an instability in the iterations, which resulted in oscillation in the computed concentrations as shown in Table 9.3.1. The concentrations shown in Table 9.3.1 are the results after 10,000 iterations, but have not reached convergence.

Table 9.3.1: A table of the computed concentrations using the finite difference method

Radius	NO^-	NO_2^-	NO_3^-	O_2^-	O_3^-	O^-	$N_2O_2^-$	O_4^-	$N_2O_3^-$	N_2O_5	NO_3	NO_2
0.15	3.09E+05	5.13E+12	1.00E-06	1.00E-06	1.00E-06	9.36E+05	1.00E-06	1.00E-06	1.00E-06	5.73E+06	1.65E+15	1.00E-06
0.26	1.35E+08	3.64E+12	5.38E+14	6.73E+07	1.00E-06	2.88E+05	2.37E+04	5.01E+04	1.00E-06	1.08E+11	8.08E+14	1.00E-06
0.36	6.21E+09	2.27E+10	1.00E-06	6.82E+09	1.00E-06	1.26E+05	3.67E+09	1.13E+09	1.00E-06	1.04E+16	1.00E-06	4.63E+18
0.47	2.55E+10	1.32E+14	1.26E+17	5.32E+10	1.29E+08	8.54E+04	1.75E+17	1.18E+10	2.51E+13	8.62E+09	4.32E+17	1.08E+19
0.58	9.14E+11	8.05E+16	1.00E-06	2.80E+11	6.91E+05	2.32E+04	1.00E-06	6.18E+10	7.25E+15	7.03E+10	2.61E+12	7.26E+17
0.69	5.26E+08	1.30E+14	3.15E+17	5.47E+08	1.00E-06	2.37E+04	4.86E+06	1.00E-06	1.00E-06	2.45E+11	4.35E+10	1.00E-06
0.80	1.85E+09	5.77E+09	1.00E-06	2.93E+09	4.73E+07	3.65E+05	5.30E+07	3.23E+07	7.21E+06	1.00E-06	2.34E+15	1.05E+19
0.91	6.28E+10	1.00E-06	1.00E-06	1.32E+11	1.00E-06	1.43E+04	7.95E+11	2.51E+10	6.44E+08	1.98E+18	1.64E+13	1.27E+18
1.02	7.39E+09	2.47E+15	1.00E-06	1.74E+10	1.62E+05	1.03E+04	6.16E+12	3.88E+09	1.75E+08	8.17E+08	1.00E-06	3.78E+15
1.13	2.02E+09	1.00E-06	3.03E+13	4.76E+09	8.24E+04	1.00E-06	1.00E-06	6.41E+08	1.00E-06	1.00E-06	1.06E+14	2.24E+19
1.24	1.93E+08	3.02E+11	9.46E+15	4.59E+08	4.74E+06	1.00E+04	1.35E+12	1.02E+08	1.46E+10	1.00E-06	3.53E+14	5.17E+17
1.35	6.46E+10	2.97E+14	3.92E+17	2.11E+10	1.35E+04	1.00E-06	2.56E+13	4.69E+09	1.00E-06	7.25E+11	1.81E+10	1.64E+18
1.45	1.12E+10	5.42E+08	1.00E-06	1.93E+10	8.05E+06	1.00E-06	1.09E+13	3.97E+09	1.92E+12	2.22E+19	4.33E+14	5.84E+18
1.56	4.76E+08	1.04E+08	2.96E+15	1.12E+09	7.02E+05	1.00E-06	7.40E+11	2.42E+08	1.78E+10	1.54E+18	4.17E+15	5.86E+17
1.67	6.11E+08	1.41E+11	1.78E+14	7.76E+08	4.01E+07	2.20E+05	7.20E+07	8.17E+07	1.21E+07	1.00E-06	1.74E+15	1.00E-06

Table 9.3.1: Continue

Radius	NO	N	O	N_2O	O_3	O^+	N_2O_4	$N_4O_2^+$	N_3O^+	$N_2O_4^+$	N_2O^+	NO_4^+
0.15	4.49E+09	9.92E+10	1.05E+11	1.00E-06	2.21E+17	9.36E+08	2.80E+11	2.56E+10	1.10E+11	3.66E+11	1.00E-06	1.58E+10
0.26	8.43E+10	6.38E+11	6.73E+11	7.12E+18	5.65E+16	1.18E+06	1.46E+16	3.15E+07	6.91E+09	8.55E+06	4.65E+06	2.49E+08
0.36	9.25E+13	8.15E+08	2.46E+09	1.00E-06	7.36E+14	1.11E+05	1.00E-06	7.38E+10	1.97E+09	2.04E+10	1.00E-06	1.28E+06
0.47	4.67E+13	1.78E+08	5.99E+08	2.24E+17	1.73E+13	2.44E+04	1.35E+14	1.00E-06	1.00E-06	1.00E-06	1.00E-06	1.00E-06
0.58	4.44E+16	1.50E+09	4.27E+09	3.79E+12	3.20E+09	2.27E+05	2.82E+11	2.08E+04	1.00E-06	1.00E-06	1.00E-06	1.00E-06
0.69	1.22E+12	6.12E+09	4.44E+09	1.00E-06	2.88E+16	8.15E+06	5.32E+14	1.00E-06	3.08E+04	1.00E-06	1.00E-06	1.00E-06
0.80	2.82E+13	6.44E+07	2.01E+08	1.00E-06	1.00E-06	1.00E-06	1.00E-06	6.97E+10	1.85E+14	2.89E+11	4.11E+09	5.72E+09
0.91	3.92E+14	3.92E+08	1.04E+09	1.00E-06	1.12E+16	5.27E+04	1.00E-06	7.05E+08	4.72E+07	1.90E+08	8.32E+04	3.51E+05
1.02	3.88E+13	7.58E+10	8.44E+10	1.25E+12	2.19E+10	2.85E+06	4.36E+09	1.24E+05	8.08E+05	1.05E+05	1.00E-06	1.00E-06
1.13	2.88E+14	1.35E+07	7.80E+07	1.00E-06	1.05E+13	1.00E-06	1.00E-06	1.40E+07	1.23E+08	3.64E+06	1.00E-06	1.00E-06
1.24	1.51E+14	4.10E+08	1.34E+09	1.00E-06	1.00E-06	5.91E+04	1.96E+15	3.36E+04	1.74E+05	1.00E-06	1.00E-06	1.00E-06
1.35	3.65E+14	1.07E+08	2.25E+08	7.99E+12	8.44E+13	1.47E+04	6.05E+14	1.00E-06	5.44E+04	1.00E-06	1.00E-06	1.00E-06
1.45	1.50E+14	2.43E+07	6.01E+07	1.00E-06	1.19E+16	1.00E-06	1.00E-06	1.00E-06	1.00E-06	1.00E-06	1.00E-06	1.00E-06
1.56	6.16E+12	1.78E+08	4.43E+08	1.00E-06	6.78E+12	2.37E+04	1.00E-06	5.82E+04	4.78E+05	2.52E+04	1.00E-06	4.47E+04
1.67	2.40E+12	4.64E+11	1.49E+10	1.00E-06	1.00E-06	7.44E+05	3.62E+15	1.00E-06	7.34E+08	1.00E-06	1.00E-06	3.13E+05

Table 9.3.1: Continue

Radius	NO_3^+	N_2^+	N^+	NO^+	N_3^+	O_6^+	O_4^+	N_4^+	$N_2O_3^+$	$N_2O_2^+$	NO_2^+	O_2^+
0.15	8.89E+09	1.00E-06	1.14E+08	6.71E+10	5.63E+08	1.00E-06	3.58E+08	1.00E-06	3.37E+11	3.51E+06	1.00E-06	4.97E+08
0.26	6.66E+08	1.00E-06	1.37E+07	5.96E+08	6.76E+07	1.95E+18	8.67E+05	1.00E-06	5.54E+11	3.31E+06	1.00E-06	2.44E+06
0.36	1.72E+14	1.00E-06	4.41E+06	4.46E+09	2.18E+07	1.00E-06	2.34E+06	1.00E-06	6.89E+08	2.27E+05	4.68E+13	1.89E+07
0.47	1.00E-06	1.00E-06	2.27E+06	4.44E+04	1.12E+07	1.00E-06	1.64E+05	1.00E-06	2.99E+09	5.67E+05	1.00E-06	5.87E+06
0.58	1.00E-06	1.00E-06	1.44E+06	1.00E-06	7.03E+06	1.00E-06	9.89E+04	1.00E-06	1.00E-06	3.65E+05	1.50E+08	6.30E+06
0.69	1.00E-06	1.00E-06	1.03E+06	1.00E-06	5.07E+06	1.00E-06	3.56E+06	1.00E-06	6.97E+08	1.00E-06	1.00E-06	4.44E+06
0.80	1.17E+14	1.00E-06	7.64E+05	1.83E+10	3.78E+06	1.00E-06	7.83E+06	1.00E-06	1.35E+09	5.13E+04	4.43E+15	3.37E+06
0.91	2.03E+12	1.00E-06	5.83E+05	1.28E+07	2.88E+06	3.57E+17	4.02E+04	1.00E-06	1.00E-06	1.50E+05	1.43E+09	4.71E+05
1.02	6.44E+04	1.00E-06	4.50E+05	4.48E+04	2.23E+06	2.02E+14	2.88E+04	1.00E-06	1.18E+05	1.12E+05	1.91E+11	2.07E+06
1.13	9.79E+06	1.00E-06	3.49E+05	1.14E+07	1.72E+06	1.00E-06	2.38E+05	1.00E-06	2.77E+07	2.91E+04	1.00E-06	1.54E+06
1.24	1.64E+04	1.00E-06	2.70E+05	7.08E+04	1.33E+06	6.65E+14	1.80E+04	1.00E-06	1.00E-06	6.70E+04	1.00E-06	1.24E+06
1.35	1.00E-06	1.00E-06	2.08E+05	1.00E-06	1.03E+06	1.54E+13	1.47E+04	1.00E-06	1.12E+04	5.36E+04	1.15E+10	9.57E+05
1.45	3.15E+11	1.00E-06	1.60E+05	2.28E+05	7.91E+05	1.00E-06	2.81E+06	1.00E-06	2.64E+08	1.00E-06	1.61E+07	1.29E+04
1.56	2.73E+04	1.00E-06	1.22E+05	9.47E+04	6.05E+05	1.00E-06	6.25E+05	1.00E-06	5.45E+07	1.00E-06	1.00E-06	1.14E+05
1.67	7.79E+07	1.00E-06	9.33E+04	1.05E+08	4.61E+05	1.00E-06	2.29E+04	1.00E-06	1.85E+06	1.00E-06	5.95E+15	4.03E+05

Appendix IV: Ownership of Copyright

With regard to the intellectual property rights and copyright of the work presented in this project, it is understood that Dr. J.S. Chang and myself are co-owners of these rights.